
Doctoral Dissertations

Student Theses and Dissertations

Fall 2018

Design and characterization of multi-spectral underwater beam-port for pool-type research reactors

Meshari Mesfer Alqahtani

Follow this and additional works at: https://scholarsmine.mst.edu/doctoral_dissertations



Part of the [Nuclear Commons](#), and the [Nuclear Engineering Commons](#)

Department: Nuclear Engineering and Radiation Science

Recommended Citation

Alqahtani, Meshari Mesfer, "Design and characterization of multi-spectral underwater beam-port for pool-type research reactors" (2018). *Doctoral Dissertations*. 3088.

https://scholarsmine.mst.edu/doctoral_dissertations/3088

This thesis is brought to you by Scholars' Mine, a service of the Missouri S&T Library and Learning Resources. This work is protected by U. S. Copyright Law. Unauthorized use including reproduction for redistribution requires the permission of the copyright holder. For more information, please contact scholarsmine@mst.edu.

DESIGN AND CHARACTERIZATION OF MULTI-SPECTRAL
UNDERWATER BEAM-PORT FOR POOL-TYPE RESEARCH REACTORS

by

MESHARI MESFER ALQAHTANI

A DISSERTATION

Presented to the Faculty of the Graduate School of the
MISSOURI UNIVERSITY OF SCIENCE AND TECHNOLOGY

In Partial Fulfillment of the Requirements for the Degree

DOCTOR OF PHILOSOPHY

in

NUCLEAR ENGINEERING

2018

Approved by:

Ayodeji B. Alajo, Advisor
Hyoung K. Lee
Carlo Castano
Xin Liu
Cassie Elrod

© 2018

MESHARI MESFER ALQAHTANI

All Rights Reserved

ABSTRACT

The beam-port is a cardinal facility at research reactors necessary for dry irradiation, testing and measurement experiments. The Missouri University of Science and Technology Reactor (MSTR) is one such reactor with a beam-port. Installation of additional beam-port in such reactor facilities can be prohibitive. A novel remedy to this is an underwater beam-port for pool-type reactors. The design and characterization of a conceptual underwater multi-spectral beam-port for neutron and gamma fluxes were completed for the MSTR. The neutron spectra from the MSTR were simulated using the Monte Carlo N-particle (MCNP). The determined neutron spectra were experimentally validated using SAND-II. The underwater beam-port system was designed to be portable so that it could be moved in and out of the reactor pool. Filters and collimators were used to modify the neutron beams for thermal and fast neutron densities as well as gamma energy spectra at the target location. In its most thermal neutron configuration, the beam-port delivered $1.43 \times 10^9 \text{ n cm}^{-2} \text{ s}^{-1}$ to the target with 91.7% of the flux having energies no greater than 0.55 eV. The hardest spectrum achievable in its fast neutron configuration was $4.95 \times 10^9 \text{ n cm}^{-2} \text{ s}^{-1}$ with 51.8% of the flux having energies greater than 0.1 MeV. The beam-port was able to deliver gamma flux of $3.19 \times 10^{10} \text{ photons/cm}^2 \cdot \text{s}$ to the target. A predictive algorithm was developed in MATLAB so that: 1.) beam flux quality could be determined given collimator and filter dimensions and 2.) Collimator and filter dimension could be determined given desired flux qualities. For both scenarios, the maximum prediction errors were 19% and 8.5%, respectively. The algorithm reduced time required for one simulation to 0.007 seconds from 179 minutes when using MCNP.

ACKNOWLEDGEMENTS

I am grateful to God for his blessings in my life, then my advisor, Dr. Ayodeji B. Alajo, for his infinite patience and for his tremendous efforts, support, guidance that he provided and continues to provide during my research. I am highly thankful to him for helping me on different matters on several occasions. I am grateful for having the privilege to learn from his expertise. I would also like to acknowledge the members of my committee, Dr. Carlo Castano, Dr. Cassie Elrod, Dr. Xin Liu, and Dr. Hyoung Lee, for their interest, support, feedback and suggestions. Also, I'm thankful to Dr. Joseph Graham for his interest in, and support of, the work. I am thankful to MSTR staff, Bill Bonzer, Craig Reisner and Anthony Alchin, for assistance with the experiments at Missouri University of Science and Technology Reactor. I would like to thank the King Abdulaziz City for Science and Technology for sponsoring my PhD studies. I would like to express my appreciation to all those people in the Nuclear Engineering Department at Missouri S&T.

A special thanks to my best friend and brother, Thaqal Alhuzaymi, for his friendship, encouragement, support, assistance, and opinions; without him, this success would not have been achieved. I would like to thank Thaar Aljuwaya and all my friends for their continuous support that has been shown to me during my study.

Last but not least, I would like to thank my family for their support and encouragement during my studies. I am especially grateful to my mom for her support, encouragement, prayers, and love. Words cannot express how grateful I am to her, and to my brothers, and sisters for all the sacrifices they have made on my behalf.

TABLE OF CONTENTS

	Page
ABSTRACT.....	iii
ACKNOWLEDGEMENTS.....	iv
LIST OF ILLUSTRATIONS.....	ix
LIST OF TABLES.....	xi
NOMENCLATURE	xiii
 SECTION	
1. INTRODUCTION.....	1
1.1. TRADITIONAL BEAM-PORTS.....	1
1.2. NUCLEAR RESEARCH REACTOR.....	2
1.3. A BRIEF HISTORY OF NUCLEAR RESEARCH REACTORS.....	3
1.4. TYPES OF RESEARCH REACTORS	5
1.5. OPEN-POOL RESEARCH REACTORS	7
1.6. NEUTRON BEAM-PORT FACILITY	9
1.7. NEUTRON BEAM APPLICATIONS	9
1.7.1. Materials Testing.....	9
1.7.2. Neutron-Activation Analysis.....	10
1.7.3. Radioisotope Production	10
1.7.4. Neutron Imaging.....	10
1.7.5. Small-Angle Neutron Scattering	11
1.8. MISSOURI UNIVERSITY OF SCIENCE AND TECHNOLOGY REACTOR	11

1.9. LITERATURE REVIEW	16
1.9.1. Beam-Ports	16
1.9.2. Development of Beam-Port Design	18
1.9.2.1. Redesigning existing beam-ports.....	18
1.9.2.2. Design of neutron beam system in unconventional research reactors.....	19
1.10. OBJECTIVE AND MOTIVATION.....	20
1.11. APPROACH AND TASKS.....	21
2. CHARACTERIZATION OF MSTR PROMPT-NEUTRON SPECTRUM.....	24
2.1. NEUTRON FLUX SPECTRA DETERMINATION	24
2.2. METHODOLOGY	25
2.3. IRRADIATION FACILITIES	26
2.3.1. Source-Holder Position	26
2.3.1.1. Foil selection.....	26
2.3.1.2. Experimental procedure	27
2.3.1.3. Monte Carlo N-particle code	29
2.3.1.4. SAND-II.....	30
2.3.1.5. Results.....	32
2.3.2. Impact of Resonance Self-Shielding on Neutron Spectrum Determination	38
2.3.2.1. Experiment.....	38
2.3.2.2. Result	39
2.3.3. Bare Rabbit Tube Position	42
2.3.3.1. Foil selection.....	44

2.3.3.2. Monte Carlo N-particle code	45
2.3.3.3. Results.....	47
3. CONCEPTUAL DESIGN OF THE BEAM-PORT SYSTEM	52
3.1. MULTI-SPECTRA UNDERWATER BEAM-PORT	52
3.2. DESIGN OF THE BEAM-PORT SYSTEM	53
3.2.1. General Components	53
3.2.2. Beam-Port Tube	55
3.2.3. Movable Base	56
3.2.4. Target Delivery System.....	57
3.3. MODIFICATION TO MSTR CORE LAYOUT	58
3.3.1. Criticality.....	58
3.3.2. Conceptual Fast Neutron Island	59
3.3.2.1. Fuel element redesign	60
3.3.2.2. Core access element.....	61
3.3.2.3. Simulations	62
3.3.2.4. Results.....	63
3.3.2.5. Concluding thoughts	66
3.4. OPTIMIZATION OF THE BEAM-PORT.....	66
3.4.1. Selection of the Beam-Port Position	67
3.4.2. Selection of the Beam-Port Tube	69
3.4.3. Optimization of the Beam-Port for a Thermal-Flux.....	71
3.4.3.1. Moderator material in the beam-port	71
3.4.3.2. Moderator thickness.....	72
3.4.3.3. Fast neutron filter for the thermal beam-port.....	73

3.4.3.4. Gamma-ray filter for the thermal beam-port	74
3.4.3.5. Final design for the thermal neutron beam-port	75
3.4.4. Optimization of the Beam-Port for a Fast-Flux.....	77
3.4.5. Optimization of the Beam-Port for a Gamma-Ray Flux	79
4. CHARACTERIZATION OF NEUTRON BEAM SPECTRA	81
4.1. BEAM-PORT CONFIGURATION DETERMINATION	81
4.2. DETERMINATION OF MATERIAL CROSS-SECTIONS IN BEAM-PORT.....	83
4.3. FLUX PREDICTION GIVEN MATERIAL THICKNESSES	85
4.4. MATERIAL THICKNESSES FOR DESIRED FLUX.....	86
4.4.1. Problem Statement	86
4.4.2. Solution by Newton's Method	88
4.4.3. Solution Steps.....	89
5. CONCLUSIONS	92
5.1. CONCLUSION ON MSTR PROMPT-NEUTRON SPECTRUM	92
5.2. CONCLUSION ON SENSITIVITY OF MSTR SPECTRUM TO INITIAL SPECTRUM GUESSES.....	93
5.3. CONCLUSION ON MULTI-SPECTRUM BEAM-PORT DESIGN	95
BIBLIOGRAPHY.....	98
VITA.....	102

LIST OF ILLUSTRATIONS

Figure	Page
1.1. Cutaway View of the MSTR.....	12
1.2. Standard Fuel Element.....	13
1.3. MSTR Core Configurations: (a) 120W, Current and (b) 101W, Retired.	14
2.1. Foil Cross-Sections as a Function of Incident Neutron Energy.....	28
2.2. Coarse and Fine Spectra (120W) at the Source-Holder from MCNP Calculations...	31
2.3. MSTR Neutron Flux Spectra at the Source-Holder.	33
2.4. Foil Detector Regions in the Unfolded Spectrum.....	35
2.5. MSTR and MCNP Integrated Flux as a Function of Neutron Energy for the 120W Configuration.....	37
2.6. MSTR Neutron Flux Spectra	39
2.7. Non-Thermal Region of the Spectra: (a) Resonance Energy Region; (b) Fast Energy Region.....	41
2.8. MCNP Initial Estimates of Spectra Obtained from the Bare Rabbit Tube (120W).	46
2.9. MSTR Neutron Flux Spectra at the BRT.....	47
2.10. Cumulative Distribution of the Relative Error in the Fluxes for Energy Groups....	50
3.1. Side View of the MSTR and the Beam-Port System.....	53
3.2. Beam-Port System, Showing the Beam-Port (A), the Movable Base (B), and the Target Delivery System (C)	54
3.3. Beam-Port Tube.....	55
3.4. Beam-Port in the Core	56
3.5. Movable Base.....	58

3.6. Target Delivery System	59
3.7. MSTR Core Configuration (Modified).....	60
3.8. Fuel Element with Zircaloy	61
3.9. Core Access Element	61
3.10. Flowchart for CAE Simulations.....	62
3.11. Core Access Element Simulations.....	63
3.12. Neutron Flux Spectra in the Core Access Element (CAE): (a) CAE Moderated by H ₂ O or Zr. (b) CAE with Full-Length Fuel Plates. (c) CAE with Half-Length Fuel Plates	64
3.13. Optimization of the Beam-Port Position.....	67
3.14. Effect of Beam-Port Diameter on the Neutron Flux.....	69
3.15. Moderating Ratio for Moderator Material	72
3.16. Ratio of Thermal Neutron Flux to Fast Neutron Flux at the End of the Beam-Port vs. Beryllium Thickness	73
3.17. Final Design for the Thermal Neutron Beam-Port	76
3.18. Target Delivery Tube.....	77
3.19. Fast Neutron Flux Spectrum in the Target Delivery System.....	78
3.20. Gamma-Ray Flux Beam-Port	79
3.21. Gamma Spectrum in the Target Delivery	79
4.1. Beam-Port Configuration.....	81
4.2. Cross-Section Algorithm Flowchart	84
4.3. Filters Thickness Algorithm Flowchart	90

LIST OF TABLES

Table	Page
2.1. Specification and Reaction Information for Available Foils Used for Source-Holder Spectrum	27
2.2. Reactions Used in SAND-II and the Corresponding Energies and Cross-Sections ..	34
2.3. MSTR Neutron Flux Distribution as Determined by SAND-II.....	35
2.4. MSTR Integrated Flux	36
2.5. MSTR Neutron Flux Distribution as Determined by SAND-II in Source-Holder Tube.....	42
2.6. Specifications and Reaction Information of the Available Foils Used for Bare Rabbit Tube Spectrum.....	43
2.7. Foil Cross-Sections and Energy Ranges Used in SAND-II.....	44
2.8. MSTR Neutron Flux Distribution as Determined by SAND-II in BRT	48
3.1. Technical Specifications	57
3.2. Neutron Flux Distribution in CAE as Determined by MCNP	65
3.3. Fast Neutron Flux Improvement in CAE with Moderators	66
3.4. Neutron Flux for the Beam-Port Positions.....	68
3.5. K_{eff} Values for Beam-Port with Different Diameters.....	70
3.6. Thermal Neutron Flux as Determined by MCNP	74
3.7. Neutron Flux Distribution as Determined by Using Aluminum Filter	75
3.8. Thermal Neutron Beam-Port Flux Distribution.....	76
3.9. Fast Neutron Beam-Port Flux Distribution.....	78
4.1. Material Cross-Sections in Beam-Port.....	85

4.2. Prediction Algorithm Time vs. MCNP Simulation Time	86
4.3. Predictive Neutron Flux Using MATLAB	87
4.4. Predictive Material Thickness Using MATLAB	91

NOMENCLATURE

Symbol	Description
a	Thickness of the material matrix
A_i	Atomic weight of the isotope
A_m	Atomic mass number
b	Alpha value matrix at the i^{th} energy
i	Index of the medium in the beam tube
I_γ	Gamma-ray intensity
j	Energy group
K_{eff}	Effective multiplication factor
m_i	Mass of the isotope to be activated
m_0	Initial number of target atoms
N	Number of atoms
n	Number of foils
N_A	Avogadro's number
N_0	Number of atoms initially present in the sample
S_i	Thickness of the medium
t_c	Live counting time
x	Cross-section for the filter matrix
ϵ	Detector efficiency
Σ_s	Scattering cross-section
Σ_a	Absorption cross-section

$\Sigma_{r,i}^j$	Removal cross-section for element i at energy range j (k is either fast or thermal)
α	Activity of the standard sample
α_i	Measured activity of foil i
α_s	Saturation activity
α_{tr}	Activity of the sample after irradiation for time t_r
γ_i	Natural abundance
λ	Decay constant of the product isotope
ξ	Average logarithmic energy decrement
σ	Microscopic cross-section of the sample
$\sigma_i(E)$	Energy-dependent neutron cross-section of foil i
φ	Neutron flux
φ_{Tgt}	Neutron flux in the target delivery system
φ_{rx}	Reactor flux
φ_k^j	Flux at position k with energy range j (k is either fast or thermal)

1. INTRODUCTION

1.1. TRADITIONAL BEAM-PORTS

Beam-ports are essential to the robustness of research reactors, especially for radiography, radiolysis, and other experiments involving neutron transmission. The beam-port of most pool-type research reactors has multiple horizontal ports. The number of beam-ports and their arrangement differ from reactor to reactor. The prevailing design of beam-ports for pool-type research reactors are tubes protruding through the biological shield and then through the pool wall. They are directed at the reactor core center. A beam-port allows a beam of neutrons for experimental purposes to pass from the reactor through the tube. However, the design of the beam-ports differs in each experimental facility. The neutron beam from a beam-port depends on many factors, including the size and shape of the port as well as the location and orientation of the beam-port with respect to the reactor core, core-moderator configuration, reflectors, filters, and collimators. Each of these factors needs to be well defined to characterize the neutron beam, which will then have a fixed spectrum. To produce neutron beams with different spectra for various applications, multiple beams must then be designed as part of the reactor facility.

There are inherent limitations to fixed (traditional) beam-ports built into research reactor facilities. First, there is the obvious limitation of the fixed spectrum. Moreover, a traditional beam-port does not readily lend itself to core redesign. For example, a change in the reactor fuel that involves a change in the active fuel height may result in the beam-port not being directed at the axial center of the core (where the flux is usually highest). For reactors with multiple beam-ports, a change in the core configuration may lead to the

loss of a useful neutron beam from one or more ports. In such cases, the reactor facility must compromise between an optimal core configuration with regard to the in-core characteristics and an optimal beam flux at the beam-port. Another limitation of a traditional beam-port is the challenge of installing additional ports after completion of the reactor facility. For example, cutting through the pool wall to install another beam-port may compromise the structural integrity of the reactor pool. Even when technical challenges like these are surmounted, the costs may be unreasonable.

Thus, an alternative that provides the benefits of traditional beam-ports while avoiding their limitations is a novel approach to research reactor design. An additional innovation of this project is to use filters and a collimator configured to provide the option for a neutron-only beam-port or a gamma-only beam-port. Moreover, the neutron-only mode would be capable of providing spectra from a soft (thermal) spectrum to a hard spectrum. The design is envisioned to be relatively portable, which would allow it to be moved in and out of the pool. This would also allow for beam realignment where and when necessary. For example, core configuration changes may necessitate the realignment of a beam-port.

1.2. NUCLEAR RESEARCH REACTOR

Nuclear research reactors are not used to generate energy but to provide neutrons. These reactors are used for research, development, and education. The neutron beams generated from such reactors are used for material testing, agriculture, medicine, etc. Compared with their power-generating counterparts, research reactors function at lower

temperatures and utilize higher uranium enrichment. Many research reactors are built near or on a campus for university research (IAEA, 2016).

Research reactors like other nuclear reactors rely on fission chain reactions to produce neutrons. A fission reaction is the division of a heavy metal nucleus into smaller nuclei, a few neutrons, and a large amount of energy. When the mass of uranium fuel is above a critical mass, a chain reaction occurs as the neutrons produced in one reaction cause fission in other uranium atoms. This cascade is controlled in a reactor by a control system so that the reaction is sustained and to ensure that the reactor rating is not exceeded.

The key components of a reactor are (Martens & Jacobson, 1968):

- the fuel used in the fission reaction
- a moderator to slow down the neutrons so that fission occurs more readily
- a coolant to remove excess heat to prevent overheating
- a reflector to mitigate the escape of neutrons
- a shield to protect the surroundings from radiation
- a control system used to regulate the reaction rate.

1.3. A BRIEF HISTORY OF NUCLEAR RESEARCH REACTORS

The history of nuclear reactors started with the discovery of nuclear fission, which was announced in 1939 along with the possibility of its use as a power source. However, with the advent of World War II, it was realized that a fission chain reaction could be used to make a weapon: the atomic bomb. Thus began the Manhattan Project, which had the goal of producing a chain reaction for a nuclear weapon and subsequently, the creation of a new element, plutonium.

The development of the first reactor was supervised by the leading nuclear physicist Enrico Fermi at Columbia University. This research was first demonstrated at the University of Chicago in the form of Chicago Pile No. 1 (CP1). This experimental reactor was built using pure graphite. It did not have a cooling mechanism as it was expected to produce low power (10 kW thermal energy). It was later reconstructed at a new site in the suburbs of Chicago and was used as a research reactor until 1953. The success of CP1 was followed by the first production reactors at Hanford, Washington. The first fuel-enriched research reactor was constructed at Los Alamos, New Mexico, in 1944 as the use of enriched uranium-235 for research purposes became possible. These efforts resulted in the first test of an atomic bomb on 16 July 1945 at Alamogordo, New Mexico.

During the Manhattan Project, the possibility of using heavy water as the neutron moderator in a reactor had been assigned to a Canadian research team (as Canada had heavy-water production facilities). This Canadian project bore fruit in late 1945 with the success of a heavy-water-moderated uranium-fueled research reactor, the Zero-Energy Experimental Pile, at Chalk River, Ontario. This was followed by Soviet bombs and other nuclear programs all over the world and to the commercial use of reactors for power generation. The history of nuclear reactors can be divided into four generations:

- Generation I: These early prototype reactors were the first to produce civilian nuclear power.
- Generation II: Commercial power reactors emerged in the mid-1960s. These are still the most widely used reactors today. Second-generation power reactors have active safety systems. They reduce the risk by

employing human operators to activate the reactor. Furthermore, the reactor is designed to stop functioning if there is an electrical shutdown.

- Generation III: Advanced light water reactors were installed during the 1990s. They have passive safety systems that operate without human intervention to increase reactor safety. Control rods drop into the reactor core if there is an electrical shutdown. This halts the fission reactions. Decay heat is transported out through gravity-fed cooling tanks.
- Generation IV: Next generation nuclear plants are being planned for implementation in the second quarter of the 21st century. The goals for these nuclear plants are for them to be economical and safe, to produce minimal waste and to be resistant to proliferation (Behar, 2014; Spinrad & Marcum, 2018).

1.4. TYPES OF RESEARCH REACTORS

The design of a research reactor depends on its planned uses. The neutron spectrum and intensity are tailored accordingly. The most specialized research reactors have very specific flux characteristics, whereas multipurpose research reactors intended for several types of activities are designed to generate fast, thermal, or intermediate neutron spectra with less specific features.

There are many types of nuclear research reactor in use, each named after a distinctive feature:

- Graphite reactors: These reactors use graphite as the moderating material. The graphite slows down neutrons but absorbs very few of them. The core

of a graphite reactor may be very large, so it is possible to use natural uranium rather than enriched uranium. The first reactor built in the Manhattan project was a graphite reactor. For example, the X-10 graphite reactor at Oak Ridge Tennessee (Cagle, 1953).

- Water-boiler reactors: This type of reactor does not utilize boiling water but is so named for its distinctive appearance, since the aqueous uranium salt solution gives off bubbles during use. They are generally low-power reactors, limited to 50 kW (thermal). This is the simplest reactor type. The main component in the reactor core is a sphere with a coil of tubing inside. This sphere has various openings for fuel, waste gases, and control rods (Bunker, 1983).
- Heavy-water reactors: These reactors use heavy water, which is water enriched in deuterium-bearing molecules rather than the common hydrogen isotope. Heavy water has the same chemical properties as water but since deuterium has an extra neutron, it absorbs fewer neutrons. Generally, they are top-shielded reactors, which are more compact and consequently, the volume of heavy water required is reduced (Kirk & Greenwood, 1979).
- Pulsed reactors: The power in this type of reactor rises and falls very quickly in short bursts or pulses. These bursts last for only a fraction of a second. The maximum output is about 5000 MW (thermal), which is equivalent to 250 kW to 5 MW from a non-pulsing reactor (Martens & Jacobson, 1968).
- High-flux reactor: These are built to produce heavy elements like plutonium, curium, and for isotope production. They use a flux trap. A

region of fuel surrounding an island of moderating region makes up the core. The fast neutrons are moderated in the island, which results in a high thermal neutron flux at the center of the core. These thermal neutrons reside or are trapped in the center of the core, from where they are channeled out through beam tubes to produce isotopes ("History of the High Flux Isotope Reactor," ; Kouts, 1963).

- Tank reactors: There are two basic versions of tank reactors: the open-tank reactor and the top-shielded tank reactor. The open-tank reactor has a lower power level of about 5 MW while the top-shielded tank reactor is used for much higher power levels. Top-shielded tank reactors are like fixed pool reactors, but with an enclosed core (Martens & Jacobson, 1968). Open-tank reactors are water-cooled plate-fueled reactors like the pool reactor detailed below. They have solid concrete shielding and controlling the flow of pumped water is simple.

1.5. OPEN-POOL RESEARCH REACTORS

An open-pool research reactor is a common type of water-cooled reactor, which use enriched uranium bonded with aluminum alloy plates as fuel. They use water as a coolant, reflector, moderator, and shield. Since they are not used for power generation, their specifications include thermal power, neutron density, and nominal neutron energy.

The core in a pool-type research reactor is placed at the bottom of a pool that is at least 18 feet deep and has no shallow end. The depth of water is necessary to shield the surroundings from the radioactivity. The reactor core is suspended from a bridge that can

move the core to anywhere within the pool. The bridge has a mechanism to control the fission reaction with extension rods that reach the core (Martens & Jacobson, 1968).

In a pool reactor, it is simple to place the beam-port tubes that transport the neutrons for research. Besides using water as a reflector, some reactors use blocks of graphite as inner reflectors around the core. The reflectors down-scatter neutrons to produce regions with a higher concentration of thermal neutrons. These higher concentration regions are exploited for experimental use (Spinrad & Marcum, 2018).

The cooling mechanism used in this type of reactor is mainly convection. This is also why initially only low-power pool-type plate-fueled reactors were thought possible. The limitation to the power output of the reactors was due to the cooling mechanism and the radioactivity levels of the water. Neutrons in the core interact with the oxygen in water to produce nitrogen-16. The higher the power of the reactor, the more nitrogen-16 and heat are produced. Nitrogen-16 has a half-life of 7.13 s (Tuli, 1995). It rises to the top of the pool where it is hazardous to the reactor personnel. Further, the heat produced is not efficiently disseminated through convection. These limitations were addressed with pumps, water fans, and heat exchangers, which made it possible either to keep the nitrogen-16 blanketed deep in the pool or to pump it into hold-up tanks until it decayed. The heat exchangers are placed near the hot top of the pool to allow for greater heat loss. These innovations have made it possible to have a high-power pool reactor with an output of up to 10 MW (Martens & Jacobson, 1968).

1.6. NEUTRON BEAM-PORT FACILITY

A neutron beam-port is built into a nuclear research reactor for the efficient utilization of neutrons and other radiation generated. It is a tunnel that facilitates the movement or transport of neutrons from the point of origin or the core of the reactor to a point outside the protective shielding where they can be used. The opening of the neutron beam tube inside the shielding is usually shut by a beam shutter to channel only neutrons. The beam tube often has equipment such as a collimator, which focuses and adjusts the shape of the neutron beam (Martens & Jacobson, 1968).

1.7. NEUTRON BEAM APPLICATIONS

Research reactor used for efficient utilization of neutron and other radiations. The research reactor provides neutron source for various applications. The most neutron applications are detailed.

1.7.1. Materials Testing. Neutron beams can be used in the development and testing of new materials. They are frequently used to optimize material properties. They can be used to examine the atomic and magnetic structures of materials. Neutron beams are important in solving complex engineering problems in nanotechnology, polymer engineering, material science, and archaeology.

Because they have no electric charge, neutrons are indispensable in the study of bulk and metallic materials because of their depth of penetration. Further, neutron scattering is a unique probe in material analysis due to the short-range strong nuclear and electromagnetic interactions. Thermal neutrons are used to detect light elements, to study the arrangement of complex magnetic systems, and to assess residual stress.

1.7.2. Neutron-Activation Analysis. This technique can analyze both qualitatively and quantitatively the elements in a material due to the characteristic radiation produced after the irradiation of the material by neutrons. The analysis depends on the radiation levels and the nature and interference of other elements in the sample. This technique is used in various fields like biology, medicine, forensic science, chemistry, and mining.

1.7.3. Radioisotope Production. Radioisotopes are radioactive isotopes of an element. These isotopes release energy in the form of radiation. They occur naturally and are also produced artificially for use in medicine, industry, and agriculture. Radioisotopes can be produced by bombarding a target metal with neutrons.

In several medical imaging techniques, such as for the thyroid, radioactive tracers are crucial in identifying diseased tissue. In medical research, positron emission tomography is used to study blood flow, glucose metabolism, and cancerous tissues. Various cancer treatments also require radioisotopes. The radioisotopes are administered both locally and orally, depending on the need and the risk associated with the radioactivity.

1.7.4. Neutron Imaging. This technique is used to analyze the structure of a sample non-destructively. Like X-ray imaging, a beam of neutrons passes through the sample and its structure and geometry can be determined by the degree of attenuation. In contrast to X-ray imaging, the beam interacts with the nuclei rather than the electrons and is attenuated by lighter elements like helium and can penetrate heavier materials like lead. This is an advantage for 3D imaging and there is an attenuation contrast with X-rays. For example, neutron imaging is used to detect hydrogen and to determine the efficiency of batteries.

Other applications include the non-invasive study of artifacts and the non-destructive study of nuclear fuel (AGENCY, 2014).

1.7.5. Small-Angle Neutron Scattering. Neutron scattering is used to study the structure and dynamics of materials. Since neutrons lack electrical charge and interact with other nuclei only over very short ranges, they penetrate deeply. The neutron-scattering measurements obtained can be used to determine atomic coordinates in lattices and the molecular structure of polymers.

With the pioneering use of Wolter optics based on axisymmetric grazing-incidence focusing mirrors, it possible to turn pinhole-camera-like neutron instruments into powerful microscopes ("Neutron Beam Applications," 2018).

1.8. MISSOURI UNIVERSITY OF SCIENCE AND TECHNOLOGY REACTOR

The 200-kW open-pool research reactor at Missouri University of Science and Technology was built in 1961 for training nuclear engineering students and for research (Figure 1.1). The Missouri University of Science and Technology Reactor (MSTR) uses light water moderation and natural convection cooling. The MSTR has a single-beam-port. It consists of a 15-cm-diameter tube, which is sealed at the end closest to the reactor to prevent the loss of water from the reactor pool. The other end in the MSTR basement is open. The neutron beam is used for neutron-activation analysis (Bonzer & Carroll, 2008). The beam tube is surrounded by concrete shielding and there is a lead plug at the end of the beam tube to reduce the transmission of gamma-rays.

The reactor core consists of 19 fuel elements (Figure 1.2) positioned in a 9×6 grid on an aluminum plate (Figure 1.3). The cross-section of each fuel element is a square of

side 76 mm. The fuel elements are 87 cm tall and they have a cylindrical nose piece, which plugs into the grid plate. All except four of the fuel elements contain 18 aluminum-clad fuel plates, with inter-plate spacing to accommodate the flow of coolant. Each fuel element comprises of U_3Si_2 -Al fuel plate enriched to 19.75% ^{235}U . The four fuel elements without the full complement of plates have had 10 of the central fuel plates removed to accommodate a control rod.

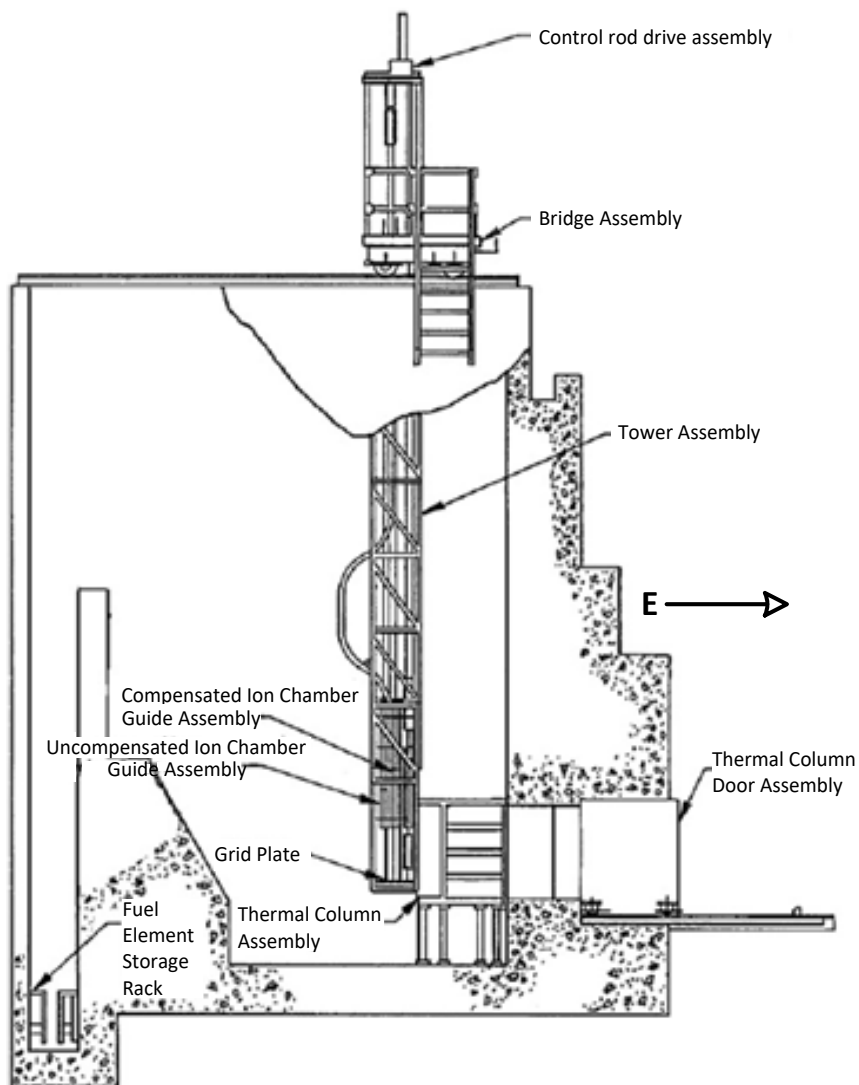


Figure 1.1. Cutaway View of the MSTR.

The four control rods (three shim-safety rods and one regulating rod) go into the middle of the reactor core. The three shim-safety rods are made of 1.5% natural-boron stainless steel. They are used to control nuclear fission in the core and to shut down the reactor. The regulating rod is made of stainless steel (SS304) and is used to keep the reactor power stable. The height of all four control rods can be detected remotely.

A plutonium–beryllium startup neutron source can be inserted into the grid plate at the source-holder position. It is used for low-power and subcritical operations.

The reactor core is submerged in approximately 113.6 m³ of demineralized water in an 8.2-m-deep part of the concrete pool. The fuel is stored in the 9.1-m-deep part of the reactor pool, separated from the main part of the pool by a concrete bulkhead (see Figure 1.1) (Bonzer & Carroll, 2008; MSTR, 2012-2013).

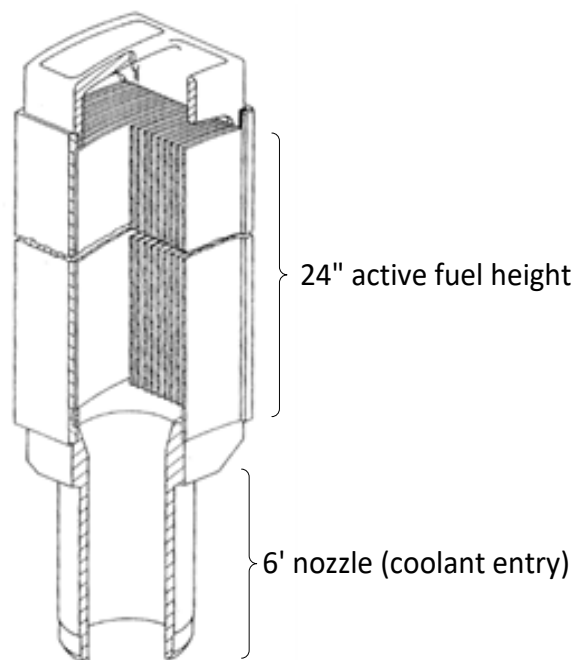


Figure 1.2. Standard Fuel Element.

The reactor core together with the in-core experimental facilities and control rods hang through aluminum scaffolding from a manually operated bridge tower.

	1	2	3	4	5	6	7	8	9
A									
B						S			
C					C-4	F-5	F-1	F-17	
D				F-4	F-8	F-14	C-1	F-10	F-2
E				F-9	C-3	F-12	C-2	F-7	F-3
F				CRT	F-15	HC	F-13	BRT	F-6

(a)

	1	2	3	4	5	6	7	8	9
A									
B						S			
C						F-8	F-4	C-4	
D				F-13	C-1	F-3	F-2	F-12	F-15
E				F-10	C-2	F-1	C-3	F-9	F-14
F				CRT	F-5	F-6	F-7	BRT	

(b)

S: Source-Holder, F-#: Fuel Element, C-#: Control Rod, HC: Hot Cell, BRT: Bare Rabbit Tube, CRT: Cadmium Rabbit Tube

Figure 1.3. MSTR Core Configurations: (a) 120W, Current and (b) 101W, Retired.

The bridge is about 3.4 m long and 1.4 m wide and can be displaced along the long axis of the reactor pool on rail tracks. The grid plate contains 54 61-mm-diameter holes that hold the elements and allow water to pass through to cool the core. The holes are labeled A–F by row and 1–9 by column. Moreover, there are 22.2-mm-diameter holes between these larger holes to allow water to flow inside the reactor core and to cool the outside surfaces of the fuel elements. The source-holder occupies position B6, and the four control rods are in positions C5, D7, E5, and E7. The grid plate is also designed to support experiments (Bonzer & Carroll, 2008; MSTR, 2012-2013).

The MSTR contains various irradiation facilities such as the hot cell, and the bare and cadmium rabbit tubes (Figure 1.3(a)). These facilities are positioned in the core. Samples can be remotely moved into and out of the core using compressed nitrogen. This system allows samples to be positioned in zones of high neutron flux. Other irradiation

facilities include a beam tube, a source-holder tube, and a thermal column. The thermal column 1.1 m (length) \times 1.1 m (width) \times 1.75 m is located behind the reactor core. The movable bridge allows the reactor core to be displaced toward the thermal column, where reflection by the graphite produces thermal neutrons for experiments. The MSTR supports both dry and wet samples for irradiation, albeit in different areas

These facilities support various experiments such as isotope production, neutron activation, materials science, and medical research. Some of the recent work at the MSTR includes neutron and X-ray combined computed tomography (Sinha, Avachat, & Lee, 2013), the development of a dual-chamber internet-accessible hot-cell facility (Grant, Mueller, Castaño, Usman, & Kumar, 2011), and a study of the criticality, temperature, and void coefficient of reactivity (Richardson, Castano, King, Alajo, & Usman, 2012).

In 2010, the reactor core configuration was changed from designation 101W to designation 120W (Grant et al., 2011). The previous configuration (101W) had 14 standard fuel elements and four control-rod-accessible fuel elements (Figure 1.3(b)). The group of elements was surrounded by water. The source-holder in position B5 was surrounded by water on three sides and there was a fuel element on the fourth side. The current reactor core has been reconfigured and two new fuel elements have been added. These new fuel elements are positioned to the right of the reactor core close to the beam-port. There is also a new irradiation facility (the hot cell) (Grant et al., 2011). As shown in Figures. 1.3(a) and 1.3(b), the source-holder is in the same relative position in both configurations.

The MSTR has two reflector modes: water-reflector mode (W mode) and thermal-column-reflector mode (T mode). In W mode, the reactor core is surrounded by water on all sides. In T mode, the rear of the reactor core touches the graphite thermal column, which

reflects neutrons toward the core (Grant et al., 2011). The reactor has seen various configurations starting with configuration 101W. The reactor has been primarily used in W mode, which is the focus of this work (Alqahtani & Alajo, 2017b).

1.9. LITERATURE REVIEW

This section is present a relevant literature review about the traditional beam-port designs issues.

1.9.1. Beam-Ports. Research reactors with beam tubes were being implemented as early as the late 1940s. The considerable progress in technology and theory since then has led to better designs. What was initially not possible to calculate then is now possible due to new techniques. The use of the beam tubes has unearthed practical limitations of the original model, which led to a subsequent redesign. There is a further need to cope with the ever-growing number of new applications and experimental techniques and to continue to remain relevant (through redesigns). There are various issues with beam-port designs:

- **Positioning:** Conventionally, beam tubes projected radially from the core, which decreased the quality of the neutron beam due to the background radiation from the core. Now, tangential beam tubes are used to lessen the background radiation. Some vertical beams are used to harvest cold neutrons, using gravity for deceleration. The point of origin of beam tubes was previously just near the core, owing to calculation limitations and because the core could move. Now, most research reactors operate with an axial flux distribution, and the peak flux is below the axial center of the core, which is the optimal position for beam tubes.

- Diameter: There were problems with the small diameter beam tubes originally used. This has led to the use of wider though more costly tubes, which is a significant concern for cold neutron sources. This problem has been addressed in the BER-II in Berlin by replacing the thermal column with a wide conical beam tube(Welzel, 2007).
- Reflector material: The optimal location of the centerline of the tube coincides with the peak thermal-flux. Originally, the reactors were surrounded by light water or beryllium reflectors were placed at the core and tube border. This was not optimal and solid beryllium is more often used to surround beam tubes. This moves the thermal peak due to the water gaps produced by the differences in neutron slowing capabilities of water and beryllium. This needs to be taken into account when positioning a beam tube.
- Number and diameter of beam tubes: The optimal arrangement of multiple beam tubes with wide diameters is not the same as for a single tube.
- Safety issues: The strength of the beam-tube walls and the corrosive effect of neutrons on the walls is a major safety concern for designers(Knop, Pfaffenbach, & Schreiner, 2007). It is important to minimize attenuation of the beam and neutron leakage. To maximize the intensity, an evacuated tube is ideal but a break may lead to a water hammer (the intrusion of water into an evacuated chamber), which could tear through the metal barrier of the tube and result in a significant leak.

- Neutron guides: These have progressed significantly since the discovery of neutron reflection by metal at FRM in Garching, Germany (Knop et al., 2007). Bent multilayer guides coupled with neutron focusing devices can improve the efficiency of the production of cold neutrons.
- Beam tube material: Selection of and the transition between the materials of the inner and outer beam tubes require design experience. The inner beam tube material is selected for its characteristics under long-term radiation exposure and low neutron absorption (Roegler, 2007).

1.9.2. Development of Beam-Port Design. The following conventional research reactors have been improved and redesigned to suit modern needs and improve efficiency.

1.9.2.1. Redesigning existing beam-ports. FRG-1 at Geesthacht in Germany is a swimming pool-type research reactor primarily used for neutron beam experiments. It has eight beam tubes, seven of which are radial, and one is tangential through. This reactor has had subsequent modifications to increase the neutron flux to remain useful in current experimentation. A high flux for neutron scattering has been achieved through two compactations, which reduced the size of the core and quadrupled the neutron flux. These compactations added beryllium reflectors (specifically designed with a helium-filled box to optimize the beam tube thermal neutron distribution coupling) and minimized the water gap between the grid plate and the beam to maximize the efficiency. A cold neutron source was installed in one of the tubes to increase the number of possible applications. Safety was enhanced with beam-port, lead port, and collimator status and leakage monitoring systems. Together, these changes have increased the service life by a decade (Knop et al., 2007).

Hoger Onderwijs Reactor (HOR) is a conventional research reactor used for neutron-activation analysis and positron beams, and it has undergone subsequent modifications to improve its efficiency. A beryllium block is embedded in the beam tubes for moderation and reflection purposes. Modifications of the beam tubes include the installation of a new neutron guidance system to harvest neutron beams with maximal thermal neutron intensity and low radiation contamination and the barriers to limit consequences from inner and outer beam tube breakage. The four neutron guides act as a filter against fast neutrons and gamma radiation and have been successful in improving the signal to background radiation by a factor of 20. Several methods have been implemented to ensure that the barrier flange interface can withstand water hammer pressure in case of severe tube breakage (Vries & Verkoijen, 2007).

1.9.2.2. Design of neutron beam system in unconventional research reactors.

The following research reactors have designs optimized through calculation. The neutron beam systems of these reactors do not use conventional beam-port models and are especially notable in their respective applications.

FRM-II in Munich, Germany, is a high-performance compact reactor. It has an extended system of neutron guides, so it can use a large amount of equipment. At only 20 MW, this reactor achieves a thermal neutron flux density of $8 \times 10^{14} \text{ n cm}^{-2} \text{ s}^{-1}$. It has 10 horizontal beam tubes, all of which are tangential to the core, minimizing background radiation. The beam tubes can be categorized into those supplying thermal, hot, or fast fission neutrons and there are beams for positrons. The neutron guides have been designed with a smooth surface coating to maximize reflection. Together these features make it a suitable supply for a variety of applications (Böning & Neuhaus, 2007).

The key features of the China Advance Research Reactor are its safety, versatility, and efficiency. It has a sophisticated structure with nine horizontal tangential tubes and 21 vertical holes. The main applications of this reactor are neutron scattering, neutron imaging, radioisotope production, material testing, neutron-activation analysis, and transmutation doping. All the horizontal tubes are tangential to the core to minimize background radiation. Its core is surrounded by heavy water, which prevents the escape of fast neutrons and moderates unmoderated neutrons from the core. There is confinement of the reactor building to control the release of fission products to the environment. Five of the horizontal tubes are placed at the thermal neutron peak while the other four are in the optimal positions to function as a cold neutron source, hot neutron source, fission-fragment source, or mono-energetic neutron source, respectively. The geometry and position of each of the beam tubes has been optimized for its experimental purpose with MCNP4A (Luo, 2007).

1.10. OBJECTIVE AND MOTIVATION

The objective of this project is the design and characterization of an underwater multi-spectral beam-port for neutron and gamma fluxes from pool-type research reactors. The motivation is the inherent limitation of fixed (traditional) beam-ports built into research reactor facilities.

1.11. APPROACH AND TASKS

A complete 3D design and high-fidelity model of the beam-port system was developed. This particular model is for the MSTR, which is an open-pool reactor. Key aspects of the design include:

- Characterization of MSTR neutron and gamma fluxes.
- Replaceable beam tubes for the beam-port system: This includes the design of a subsystem to secure the beam tube underwater.
- Design and characterization of beam tubes for a specific type of particle transport or energy spectrum: Filters and collimators are used to facilitate spectral morphing and particle discrimination.
- Design of a target delivery system to place the irradiation sample at the beam-port and its subsequent retrieval: This includes designs for both wet and dry target delivery systems.
- Shielding: This is necessary to mitigate the entry of extraneous nuclear particles into the beam-ports from the surrounding pool water.
- Mitigation of gamma contamination: This is specific to the neutron-only mode. Any interaction that leads to activation in the beam tube is most likely to generate gamma particles, which would contaminate the neutron-only beam. The design will seek to eliminate or minimize this effect.

The tasks for the characterization of the underwater beam-port system include the following:

1. Determine the neutron spectrum: This is needed to establish the relevant neutronic characteristics of the current MSTR core configuration.

2. MSTR core layout modification: This ensures there is adequate excess reactivity after the implementation of the beam-port and it enhances the neutron spectrum quality at the reactor side of the beam-port.
3. Conceptual design of beam-port and target delivery systems.
4. Optimization of beam-port for thermal-flux.
5. Optimization of beam-port for a fast-flux.
6. Optimization of beam-port for the gamma flux.
7. Mitigation of gamma-rays in the neutron beam.
8. Mitigation of neutrons in the gamma beam.
9. Characterization of beam spectra: The aim is to develop characterization metrics of the beam quality. It is a predictive approach. Quantitative characteristics are used to determine the beam-port configuration required for a desired spectrum.

This characterization of the beam-port system used the Monte Carlo *N*-particle (MCNP) transport code (Monte Carlo Team, 2003). The existing MCNP5 model of the MSTR was modified to include the proposed beam-port system model. The new (modified) model was used to analyze the beam-tube designs and to optimize the calculations where necessary. While validation would be ideal for the proposed beam-port system, such validation would require the construction of an entire system. The cost of such an endeavor is prohibitive for a dissertation project. However, the results from the MCNP simulations of elements of the design were validated with experiments performed at the MSTR. Thus, MCNP simulations to determine the flux spectra and magnitude at various locations of the MSTR have been performed. These locations are the source-holder and the bare rabbit

tube. The MCNP results for these locations were also validated with experiments. A significant aspect of the validation process was the use of SAND-II (an energy unfolding code developed by Sandia National Laboratories) to determine the spectrum from experimental foil activation analysis (McElroy, Berg, Crockett, & Hawkins, 1967). Once the MCNP model of the reactor could accurately predict the energy spectra and flux magnitudes from the MSTR, it was used to determine the flux and spectrum-related characteristics of the beam-port system.

Note that tasks 1 and 2 characterized the impact of reactor changes on the beam-port system. Tasks 3 to 9 are intrinsically related to the design of the beam-port system itself. Thus, the characterization of the beam-port system will only be complete when the impact of expected reactor changes on the performance of the beam-port system can be quantified. Reactor power changes are expected in practically every reactor operation session. While core modifications are not necessarily frequent in research reactors, modification is one of the flexibilities afforded by research reactors for experimental purposes. This implies that when core modifications are required, it is equally necessary to predict the effect these may have on the beam tubes.

2. CHARACTERIZATION OF MSTR PROMPT-NEUTRON SPECTRUM

2.1. NEUTRON FLUX SPECTRA DETERMINATION

Knowing the neutron flux spectrum of a nuclear facility is important in the evaluation of any irradiation experiment. Interpreting any changes in the physical properties of materials that occur in an irradiation experiment requires good knowledge of the neutron flux spectrum prior to the start of the experiment. An established method for characterizing the reactor neutron flux is through neutron-activation analysis, in which samples are irradiated by neutrons. This produces unstable isotopes, enabling qualitative and quantitative analyses of unknown samples (Tsoulfanidis, 2010). The neutron flux spectrum of a research reactor can be obtained using several foils that are activated by being irradiated inside the reactor core. MCNP provides an initial guess of the neutron flux for a specific position in the core. SAND-II runs iteratively to obtain the best-fitting spectrum between the measured and calculated foil activities.

This activation-foil method was used to obtain the energy spectrum of the prompt-neutron flux at MSTR. The foils were irradiated at the center of the reactor core (120W configuration). The neutron spectrum was determined using the unfolding method implemented in the SAND-II code.

The primary objective of the study described herein was the determination of the prompt-neutron spectrum at two different locations of the MSTR with the 120W core configuration: the source-holder and the bare rabbit tube. This improved the documentation of the neutronic characteristic of the MSTR. This neutron spectrum flux can be used as the source term for MCNP calculations and to test beam-port designs.

2.2. METHODOLOGY

The overall approach to this work involved the modeling of the MSTR in MCNP to determine its neutron spectrum. To validate the MCNP predictions, the foil activation method was used to determine the neutron flux spectrum experimentally. This was aided by the use of SAND-II for spectrum unfolding. The MCNP prediction was used as the initial guess for SAND-II.

The activity of a sample as a function of neutron irradiation time t_r is given by

$$\alpha_{tr} = \lambda N(t_r) = N_0 \sigma \varphi (1 - e^{-\lambda t_r}) \quad (1)$$

where α_{tr} is the activity of the sample after irradiation for time t_r , N_0 is the number of atoms initially present in the sample, σ is the microscopic cross-section of the sample, φ is the neutron flux, and λ is the decay constant of the product isotope. The number of atoms N is given by

$$N = \frac{\gamma_i m_i N_A}{A_i} \quad (2)$$

where N_A is Avogadro's number, m_i is the mass of the isotope to be activated, γ_i is the natural abundance, and A_i is the atomic weight of the isotope.

After removing a sample from the reactor core, its activity at any time t is given by

$$\alpha(t) = \alpha_{tr} e^{-\lambda t} \quad (3)$$

where α_{tr} is the activity of the sample when it was removed from the reactor core.

The activity of the sample reaches the saturation level when the radiation time is infinite or much longer than the half-life of the sample. The saturation activity α_s is (Tsoulfanidis, 2010)

$$\alpha_s = N \varphi \sigma \quad (4)$$

2.3. IRRADIATION FACILITIES

An activation-foil method was used to obtain the energy spectrum of the prompt-neutron flux at the Missouri University of Science and Technology Reactor (MSTR). The foils were irradiated at the center of the reactor core (120W configuration). The neutron spectrum was determined using the unfolding method implemented in the SAND-II code. Two irradiation facilities were used to determine the neutron flux spectrum.

2.3.1. Source-Holder Position. The neutron spectrum was determined using the unfolding method implemented in the SAND-II code. The experimental and analytical determination of the spectra was performed at the locations of the source-holder and the bare rabbit tube. The source-holder tube in position B6 (Figure 1.3(a)) is surrounded by water on three sides and has a fuel element on the fourth side.

2.3.1.1. Foil selection. A set of foils was selected based on neutron interactions of interest, foil cross-section, and availability. Different sets of threshold and epithermal foils were prepared using bare and cadmium covers to cover the full available energy range. The foil set covers energies from 0.025 eV to 7.2 MeV to give a broad-spectrum analysis. The characteristics of the irradiated activation foils are given in Table 2.1. This table shows the most important reactions for each foil. Foils with relatively high absorption cross-sections were made thinner, which limits the effects of self-shielding. For example, the radiative capture cross-section of ^{197}Au at 0.0253 eV is 2 orders of magnitude larger than that of ^{64}Ni ; the same cross-section in the resonance energy range is 3 orders of magnitude higher in ^{197}Au .

All foil sets should have a good response and cover the important spectrum energies. Foils with (n, α) and (n, p) reactions are particularly necessary for fast spectrum

unfolding. Figure 2.1 shows the reaction cross-sections obtained from the ENDF/B-VII.1 library and the foil half-lives obtained from the IAEA Nuclear Data Section (Baum, Knox, & Miller, 2002; Chadwick et al., 2006).

2.3.1.2. Experimental procedure. Two sets of foils were prepared for irradiation in the reactor source-holder: a 1-mm-thick cadmium foil and a bare foil. Each individual foil was placed in a polyethylene vial and hung by a string at the source-holder position.

Table 2.1. Specification and Reaction Information for Available Foils Used for Source Holder Spectrum.

Foil	Foil thickness (μm)	Reaction	Product half-life	Energy range
Dysprosium	250	$^{164}\text{Dy}(n,\gamma)\text{Dy}^{165}$	2.33 h	Thermal
Vanadium	127	$^{50}\text{V}(n,\gamma)\text{V}^{51}$	3.76 m	Thermal
Indium	50	$^{113}\text{In}(n,\gamma)\text{In}^{114\text{ m}}$	49.51 d	Thermal
Indium	50	$^{115}\text{In}(n,\gamma)\text{In}^{116\text{ m}}$	54.00 m	Thermal Epithermal
Indium	50	$^{115}\text{In}(n,n')\text{In}^{115\text{ m}}$	4.50 h	Fast
Gold	25	$^{197}\text{Au}(n,\gamma)\text{Au}^{198}$	2.69 d	Thermal Epithermal
Aluminum	127	$^{27}\text{Al}(n,\alpha)\text{Na}^{24}$	15.00 h	Fast
Copper	25	$^{63}\text{Cu}(n,\gamma)\text{Cu}^{64}$	12.70 h	Thermal Epithermal
Cobalt	127	$^{59}\text{Co}(n,\gamma)\text{Co}^{60}$	5.27 y	Thermal Epithermal
Silver	127	$^{109}\text{Ag}(n,\gamma)\text{Ag}^{110\text{ m}}$	246.76 d	Epithermal
Nickel	500	$^{58}\text{Ni}(n,p)\text{Co}^{58}$	70.86 d	Fast
Nickel	500	$^{64}\text{Ni}(n,\gamma)\text{Ni}^{65}$	2.52 h	Epithermal
Iron	127	$^{54}\text{Fe}(n,\alpha)\text{Cr}^{51}$	27.70 d	Fast
Iron	127	$^{58}\text{Fe}(n,\gamma)\text{Fe}^{59}$	44.50 d	Epithermal
Iron	127	$^{54}\text{Fe}(n,p)\text{Mn}^{54}$	312.20 d	Fast

The reactor was operated at 100 kW for about 3 min to irradiate the samples. The individual irradiation of each sample allowed it to absorb a sufficient number of neutrons and this eliminates the self-shielding problem when multiple foils are irradiated together. After irradiation, each sample was left to cool under water until the dose rate decreased to the point where it could be handled.

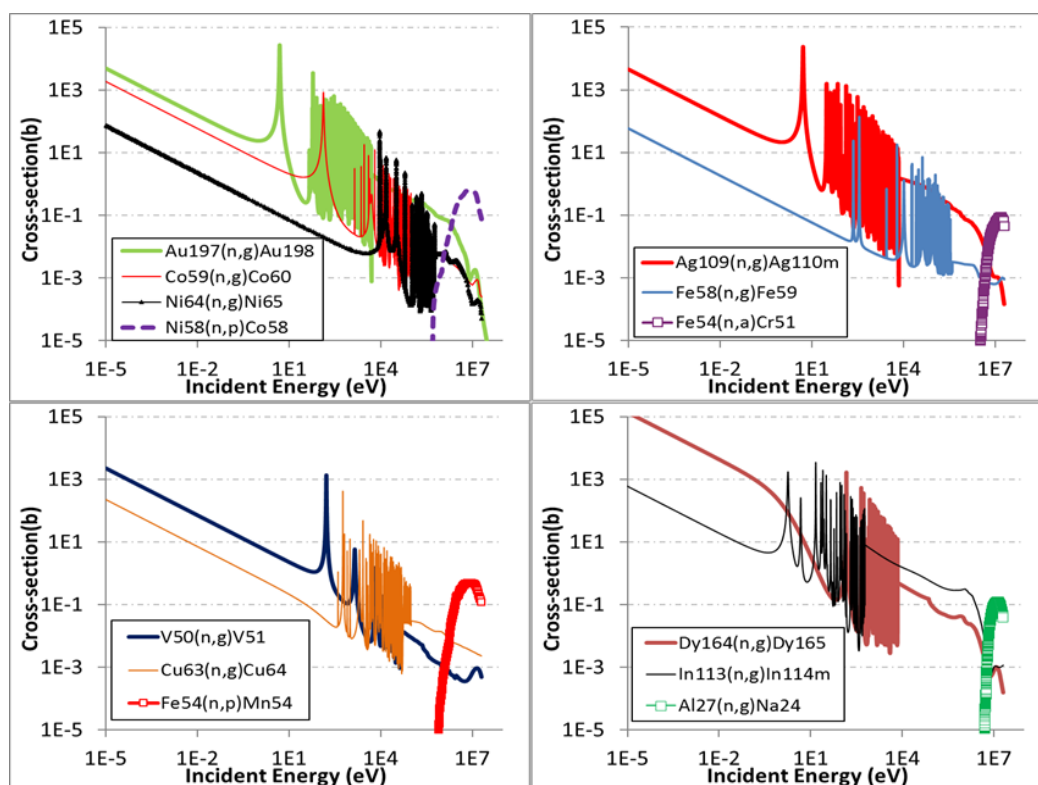


Figure 2.1. Foil Cross-Sections as a Function of Incident Neutron Energy.

The dose rate was no more than 25 mrem/h at approximately 30 cm from each sample. For each sample, bare and cadmium covers were used to determine the thermal and epithermal neutron fluxes. The activity of each foil was counted with high-purity germanium (HPGe) detectors for 3 minutes. The longest-lived activation product requiring

detection was ^{60}Co (see Table 2.1), for which the 3-minute count was sufficient to get good resolution with an HPGe detector.

The detector was calibrated using a multi-isotope europium source containing ^{152}Eu , ^{154}Eu , and ^{155}Eu . It emits gamma-rays of a specific energy at a specific rate. The detector efficiency ε was calculated using

$$\varepsilon = \frac{C}{I_{\gamma} \alpha t_c} \quad (5)$$

where C is the net gamma-ray count of the full-energy peak, I_{γ} is the gamma-ray intensity, α is the activity of the standard sample, and t_c is the live counting time (Canberra, 2010).

The foil activity was analyzed and the detectors were calibrated using Canberra analytical software (PROSPECT). The activation results were used as input data to the spectrum unfolding code SAND-II for analysis. An initial guess of a neutron spectrum is required by SAND-II. The measured activity of each foil helps the code to find the most accurate neutron spectrum results. SAND-II neglects the self-shielding effect of the foils and the cover materials used in neutron-activation analysis (McElroy et al., 1967).

2.3.1.3. Monte Carlo N-particle code. The neutron spectrum thus determined is then compared with the original MCNP spectrum. Version 5 of the MCNP code (Monte Carlo Team, 2003) was used to calculate the MSTR spectrum using 620-group energy bins from SAND-II. The spectrum was then used as an initial fine guess in the SAND-II code. An MCNP model of the MSTR that includes the reactor core, all fuel elements, control rods, the grid plate, beam-port, thermal column, irradiation facilities, pool water, and all pool structures exists. The neutron flux spectrum was simulated for a model of a polyethylene vial at the source-holder position corresponding to the experiment position

within the reactor core in the 120W configuration. The energy bins ranged from 10^{-10} to 18 MeV. The F4 tally was used to obtain the flux used as input for the SAND-II code. The cross-section library for this model uses ENDF/B-VI (.66c) in MCNP5 for all isotopes. A KCODE criticality calculation was performed with 20,000 particles per cycle for 30,050 cycles in total, after discarding the first 50 cycles. Figure 2.2 shows the MCNP spectrum from this simulation.

Another neutron spectrum containing 12 energy groups is also determined using the MCNP model and this was used as an initial coarse guess for SAND-II. For this spectrum, the 12 energy groups were obtained from a previous study (Kulage, Castano, Usman, & Mueller, 2013) that characterized the MSTR in the 101W reactor core configuration. The results from both spectra (i.e., the 620-group fine spectrum and the 12-group coarse spectrum) were then compared (see Figure 2.3). The three-group collapsed neutron flux for the fine and coarse MCNP spectra was calculated. The results show the thermal spectra accounted for 76% of the fine spectrum and 77% of the coarse spectrum, which represent the thermal proportion of the total flux. The epithermal-fluxes of the fine and coarse spectra were, respectively, 12% and 11% of the total flux. In both spectra, fast neutrons represented 12% of the total flux. Both the fine and coarse spectra were used as initial guesses in SAND-II calculations.

2.3.1.4. SAND-II. The SAND-II code was developed at Sandia National Laboratories for neutron spectrum unfolding. This code uses the iterative method of multiple foil activation to provide the best-fitting neutron spectrum for the input foil activities. As input, SAND-II requires measurements of foil activity (foil cover material

and thickness, an initial guess of the spectrum for the irradiation environment, number of iterations, and number of discards in units of standard deviation) to obtain the best solution.

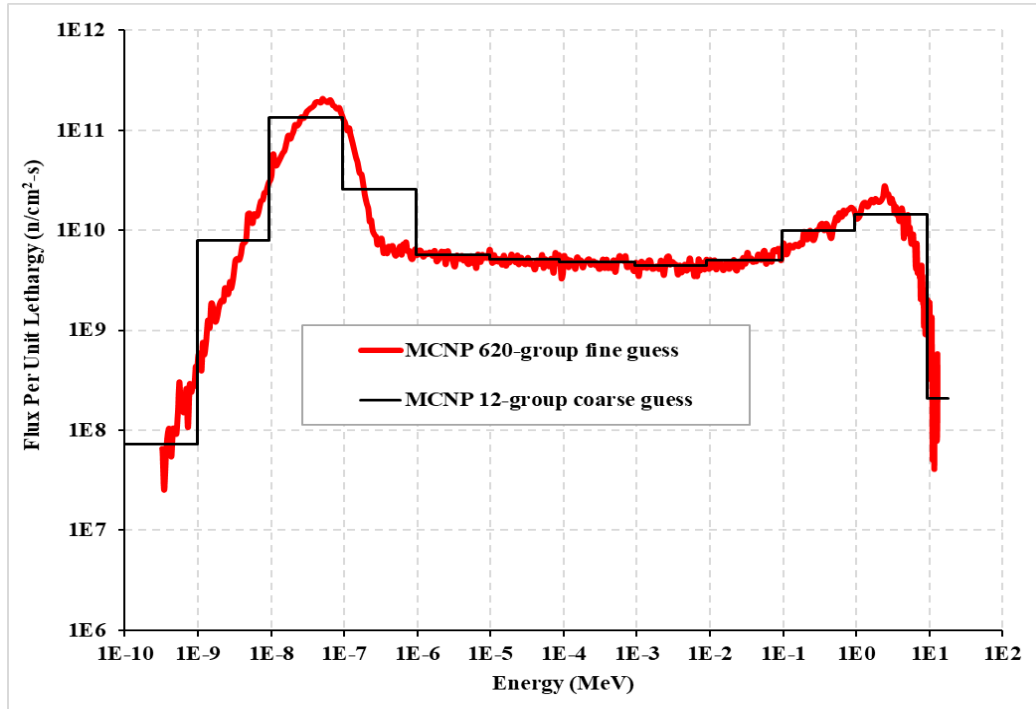


Figure 2.2. Coarse and Fine Spectra (120W) at the Source-Holder from MCNP Calculations.

The code has a cross-section library with most nuclear reactions and the spectrum library from ENDF-VII. The energy-dependent spectrum based on the initial guess of the neutron spectrum and cross-section is determined using

$$\alpha_i = m_0 \int_0^{\infty} \sigma_i(E) \phi(E) dE, 1 \leq i \leq n \quad (6)$$

where α_i is the measured activity of foil i , m_0 is the initial number of target atoms, $\sigma_i(E)$ is the energy-dependent neutron cross-section of foil i , $\phi(E)$ is the energy-dependent neutron flux, and n is the number of foils.

The foil activity is calculated from the differential flux in the steady state. The solution to this equation is provided in 620 discrete energy intervals in the range from 10^{-10} to 18.0 MeV and at 621 points. Because the number of equations (i.e., foils) is less than the number of unknowns (i.e. group fluxes), the solution of this equation is not unique. The solution provided by SAND-II minimizes the difference between the calculated activity and the measured activity of the foils (McElroy et al., 1967).

2.3.1.5. Results. Figure 2.3 shows the output of the SAND-II code. Table 2.2 shows the reactions in each neutron energy region covered by the foils (Zijp & Baard, 1981). The neutron spectrum determined from the coarse guess has a similar profile to the spectrum derived from the fine guess. The SAND-II flux profiles are consistent with the MCNP calculations in the thermal region (0–0.55 eV), which is an expected result since the MSTR is a thermal reactor and the source-holder is surrounded by water, which thermalizes most of the neutrons.

The epithermal region (0.55 eV to 0.10 MeV) of the spectrum matches that of MCNP from 0.55 eV to about 0.38 keV and the flux drops over the rest of the spectrum relative to the MCNP calculation. The drop in the flux in the epithermal and fast regions (0.10–10 MeV) may be due to foil self-shielding. Foils with several high-resonance cross-sections strongly absorb epithermal neutrons about 5 eV (ASTM E720-11, 2011). The cadmium-covered foils were used to discriminate reaction rates induced by epithermal neutrons only. None of the foils used in the experiment have effective reaction responses above 600 eV in the epithermal range.

Furthermore, the foils used to capture fast neutron-induced reactions effectively covered 2.8–7.2 MeV. The energy range with no effective neutron absorption reactions

spans 3 orders of magnitudes, which is the reason for the observed spectral depression in that energy range.

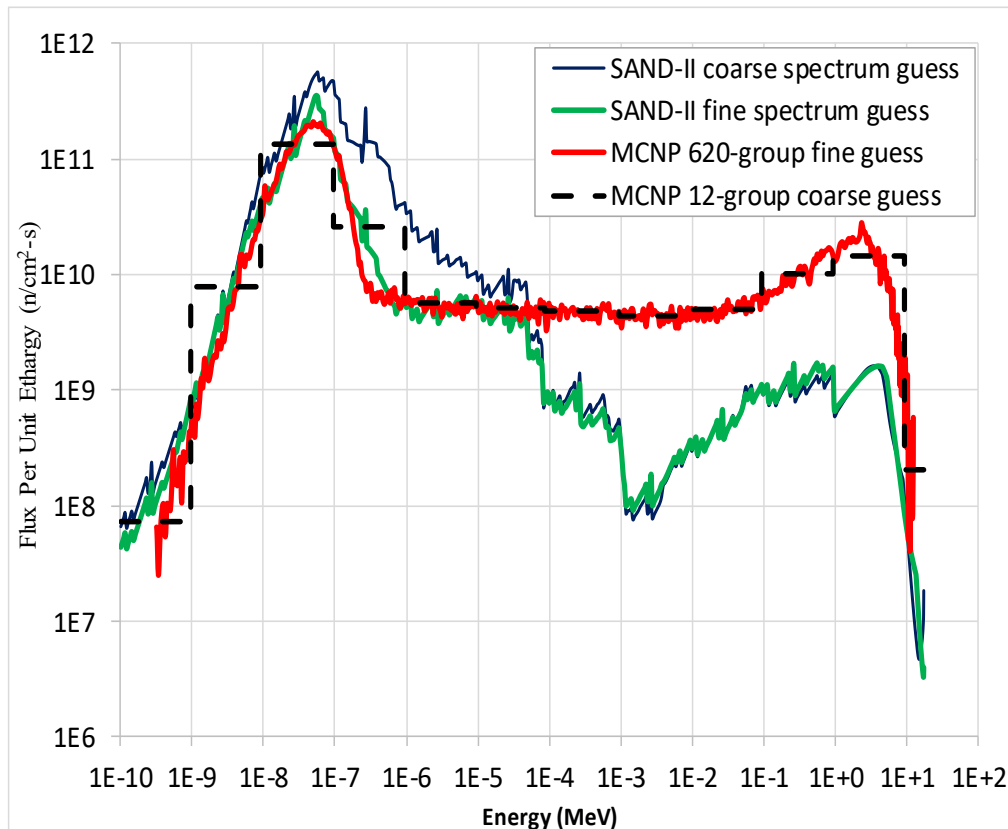


Figure 2.3. MSTR Neutron Flux Spectra at the Source-Holder.

Furthermore, the foils used to capture fast neutron-induced reactions effectively covered 2.8–7.2 MeV. The energy range with no effective neutron absorption reactions spans 3 orders of magnitudes, which is the reason for the observed spectral depression in that energy range.

Three reactions are sensitive in the fast region. Foils sensitive to fast neutrons have microscopic absorption cross-sections less than 0.5 barn in that energy range. The limited number of reactions and foils may result in a poor determination of the neutron flux in

these regions. The combination of this and the reduced number of fast neutrons in the moderating environment diminishes the number of fast energy reactions.

Six of the nine foils are sensitive to epithermal neutrons. This implies that epithermal self-shielding effects contribute to the uncertainties in the epithermal energy spectrum. Nonetheless, the foil selection covers a broad energy spectrum. Figure 2.4 shows the energy regions covered by each foil reaction used in SAND-II.

Table 2.2. Reactions Used in SAND-II and the Corresponding Energies and Cross-Sections.

Reaction	Neutron energy [foil cross-section]		
	Thermal region	Epithermal region*	Fast region
$^{164}\text{Dy}(n,\gamma)\text{Dy}^{165}$	0.025 eV [920 b]		
$^{113}\text{In}(n,\gamma)\text{In}^{114\text{m}}$	0.025 eV [3.9 b]	4.7 eV [90 b]	
$^{197}\text{Au}(n,\gamma)\text{Au}^{198}$	0.025 eV [100 b]	4.906 eV [1565 b]	
$^{27}\text{Al}(n,\alpha)\text{Na}^{24}$			7.2 MeV [0.0007 b]
$^{63}\text{Cu}(n,\gamma)\text{Cu}^{64}$	0.025 eV [4.5 b]	580 eV [5.6 b]	
$^{59}\text{Co}(n,\gamma)\text{Co}^{60}$	0.025 eV [37.4 b]	132 eV [77 b]	
$^{109}\text{Ag}(n,\gamma)\text{Ag}^{110\text{m}}$		5.20 eV [750 b]	
$^{58}\text{Ni}(n,p)\text{Co}^{58}$			2.8 MeV [0.109 b]
$^{58}\text{Fe}(n,\gamma)\text{Fe}^{59}$		230 eV [1.58 b]	
$^{54}\text{Fe}(n,p)\text{Mn}^{54}$			3.1 MeV [0.078 b]

* Cross-sections in the epithermal region are resonance integral values.

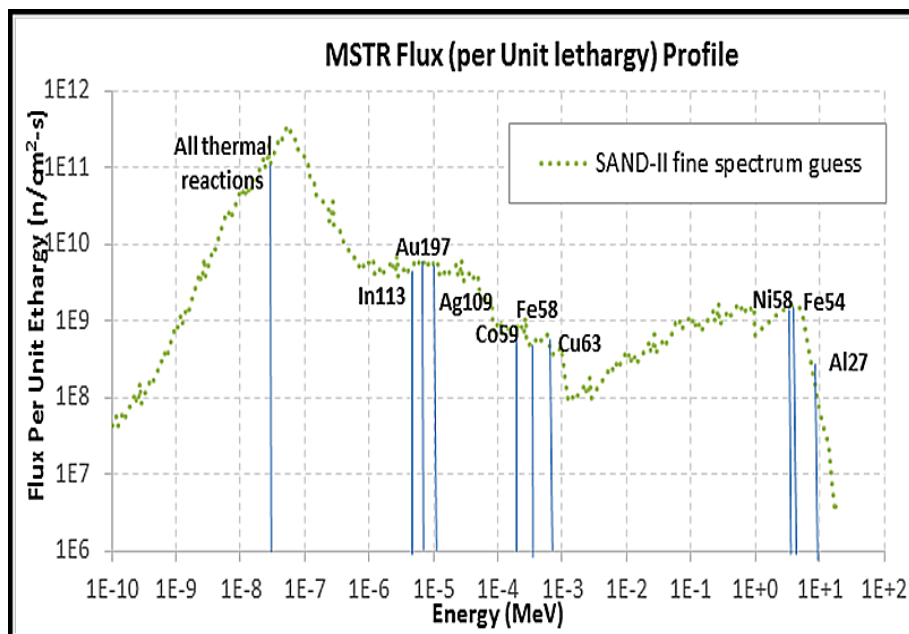


Figure 2.4. Foil Detector Regions in the Unfolded Spectrum.

Table 2.3 gives the three-group collapsed neutron flux for the MSTR at the source-holder position for the 120W reactor core configuration. The results show the thermal spectrum contributes 93% of the total flux. In comparison, from the MCNP calculation (initial guess), 76% of the total flux is thermal.

Table 2.3. MSTR Neutron Flux Distribution as Determined by SAND-II.

Energy	Range	Flux ($\text{n cm}^{-2} \text{s}^{-1}$)
Thermal	0 to 0.55 eV	$4.47 \times 10^{11} \pm 5.91 \times 10^{10}$
Epithermal	0.55 eV to 0.10 MeV	$2.70 \times 10^{10} \pm 2.24 \times 10^9$
Fast	Above 0.10 MeV	$5.11 \times 10^9 \pm 6.28 \times 10^8$
Total	–	$4.79 \times 10^{11} \pm 6.10 \times 10^{10}$

There are also significant differences between the MCNP calculation and the SAND-II prediction in the epithermal and fast contributions to the total flux (see Table 2.4). The MSTR thermal neutron spectrum characterized using SAND-II matches that given by MCNP. Corrections must be applied to improve the results for the other regions where the SAND-II spectrum deviates from the MCNP spectrum.

The integrated MSTR flux was obtained and compared with that of MCNP to determine the average difference (see Figure 2.5). The MCNP spectrum is reasonably consistent with the SAND-II spectrum.

Table 2.4. MSTR Integrated Flux.

Energy	SAND-II	MCNP	Difference
Thermal	93.3%	76.4%	16.9%
Epithermal	5.6%	12.1%	6.5%
Fast	1.1%	11.5%	10.4%
Total	100%	100%	—

The percentage difference in the contribution to the total flux was 16.9% for thermal neutrons, 6.5% for epithermal neutrons, and 10.4% for fast neutrons. For energies ≤ 0.0253 eV, the MCNP calculation and the SAND-II prediction for the contribution of the thermal-flux to the total flux are, respectively 19.4% and 21.1%. Up to 0.05 eV, the MCNP calculation and the SAND-II prediction for the contribution of the thermal-flux are 48.5% and 42.7%, respectively.

For a thermal reactor like the MSTR, difference in the predicted and calculated contribution of the thermal-flux affects activation experiments. This difference is <10% for room-temperature energies. The discrepancies at higher energies might be due to the variation in the neutron flux and the cross-sections or the uncertainty in the characterization techniques.

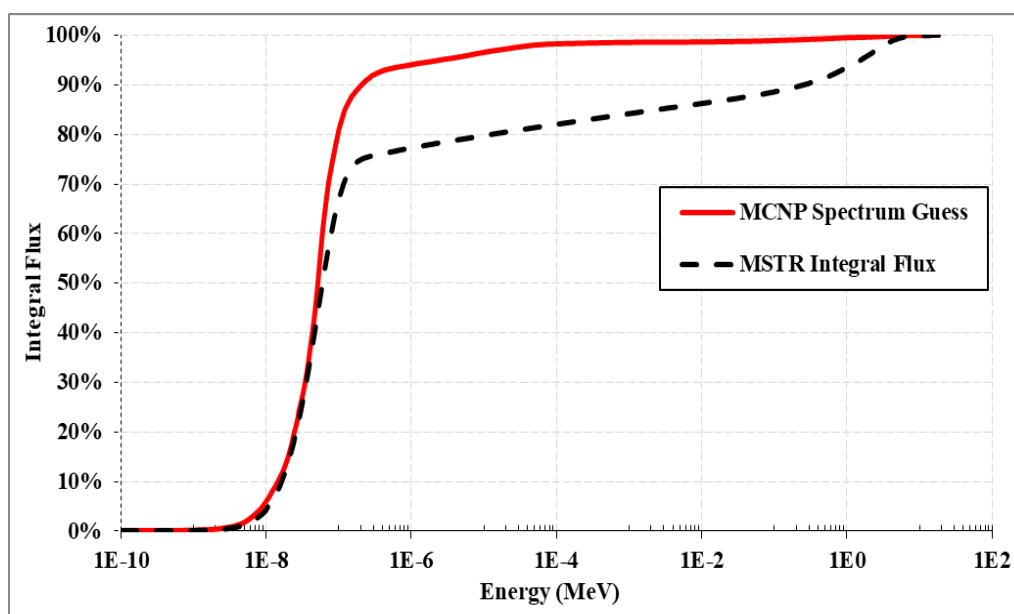


Figure 2.5. MSTR and MCNP Integrated Flux as a Function of Neutron Energy for the 120W Configuration.

Another explanation is that the MCNP model has not been updated since it was developed, which means that the MCNP spectrum assumes fresh fuel. Burnup credit impacts the spectrum and the flux magnitude calculated by MCNP.

The total neutron flux predicted by MCNP calculation is $4.98 \times 10^{11} \pm 1.72 \times 10^{10} \text{ n cm}^{-2} \text{ s}^{-1}$. The flux from the SAND-II calculation is $4.79 \times 10^{11} \pm 6.10 \times 10^{10} \text{ n cm}^{-2} \text{ s}^{-1}$, a difference of 4%.

2.3.2. Impact of Resonance Self-Shielding on Neutron Spectrum

Determination. In previous work, it was noted that the determined neutron flux spectrum at the source-holder was distorted due to self-shielding (Alqahtani & Alajo, 2017b). It is important to study neutron self-shielding, which affects the neutron spectra of thick foils. There was good agreement in the thermal region, but not in the intermediate and fast regions (see the spectra in Figure 2.6). The activation experiment was repeated with infinitely dilute solutions of elements in lieu of foils to assess the effects of self-shielding on the MSTR neutron flux spectra. The activation products were from the following reactions: (n,γ) in Dy, V, In, Au, Ag, Cu, Co, and Fe; (n,p) in Ni and Fe; and (n,α) in Al. All experiments were performed at the source-holder location. The purpose of this current study is to investigate the impact of resonance self-shielding of some of the activated foils on the determined spectrum (Alqahtani & Alajo, 2017b).

2.3.2.1. Experiment. A set of eight solutions were prepared for irradiation in the reactor core at a thermal power of 100 kW. The solution was prepared by dissolving CuCl_2 , AgNO_3 , FeCl_3 , VCl_3 , AuCl_4 , CoSO_4 , NiO_4S , and $\text{Dy}(\text{OOCCH}_3)_3$ in de-ionized water. The weight of the salt depended on the concentration of the liquid. Each salt was dissolved in 50 mL of liquid at a concentration of 0.01 M. Each sample was placed in a small polyethylene vial (1 mL of solution) and then hung by a string in the source-holder location within the reactor core, and irradiated for 3 min. For each sample, bare and cadmium covers were used to discriminate between thermal and epithermal neutron activation. The activity of each solution was counted with HPGe detectors for 3 min. Note that only 8 of 10 infinitely dilute solutions were made; salts of aluminum and indium were not available to the authors (Alqahtani & Alajo, 2017c).

2.3.2.2. Result. Figure 2.6 compares the neutron spectra determined with foils and solutions. The MCNP prediction was the initial guess provided to SAND-II for the activity unfolding in foils and solutions. The spectra are reasonably identical in the thermal region, regardless of the mode of determination. Beyond 40 eV, the spectrum determined through foil activities is lower, deviating significantly from the spectra based on infinitely dilute solutions. The depression of the flux in the resonance region could have occurred due to self-shielding. All foils with (n,γ) reactions are deemed responsible for the resonance flux depression. This is supported by the elimination of the depression when activated infinitely dilute solutions were used for the spectrum determination (see Figure 2.6).

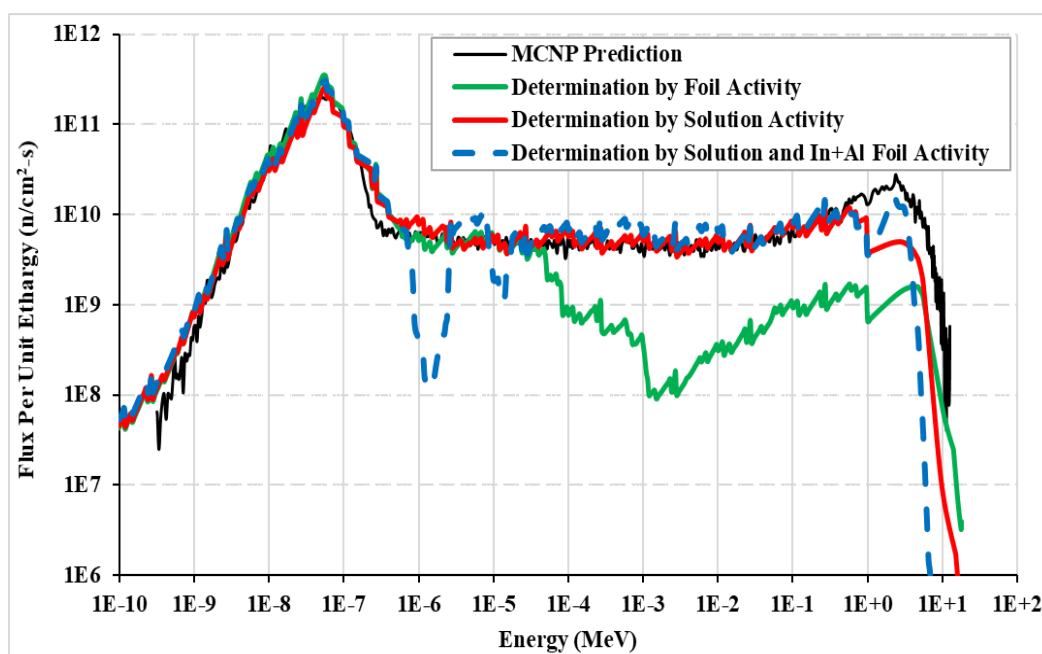


Figure 2.6. MSTR Neutron Flux Spectra.

The spectrum determined from only dilute solutions agrees well with the predicted spectra except at energies above 1 MeV (Figure 2.7(b)). This may be a consequence of not having an aluminum-based dilute solution. The (n,α) reaction in aluminum impacts the

determination of the high-energy neutron flux. Indium was the other element without a dilute solution. This impacts the determination of the thermal and epithermal-fluxes, which are, however, covered by other elements. The 10 foils represented 11 reaction types (Fe has both (n,γ) and (n,p) reactions). The determination of the flux using only the eight infinitely dilute solutions provided nine reaction types. Using only the activities of the solutions in the spectrum unfolding implies that fewer reactions are used in the spectrum determination.

To see the effect of additional reactions on the spectrum determined from dilute solutions, reaction data for aluminum and indium foils were included. This provides 11 reaction types, the same as for the 10 foils. In the resulting spectrum, the fast energy flux was refined (Figure 2.7(b)), which is attributable to the data for the aluminum reaction.

However, there are two significant depressions in the early resonance range between 0.6 eV and 27 eV (Figure 2.7(a)). The first of the depressions is between 0.6 and 2.7 eV, with the lowest point at 1.5 eV. The first resonance of ^{115}In has a peak at 1.46 eV, where resonance self-shielding is expected to be effective (Griffin & Kelly, 1995). The second depression is between 8 and 27 eV. This depression may be due to the compounded effect of the next four resonances of ^{115}In . These resonances are at 3.85, 9.07, 12.04 and 22.73 eV.

The observations also present a conundrum: depressions seemingly introduced by indium foil to the dilute solution spectrum were not observed when the spectrum was wholly based on foils. There may be mutually negating effects from the resonance impacts of other foils, which concealed the depression when all foils were used.

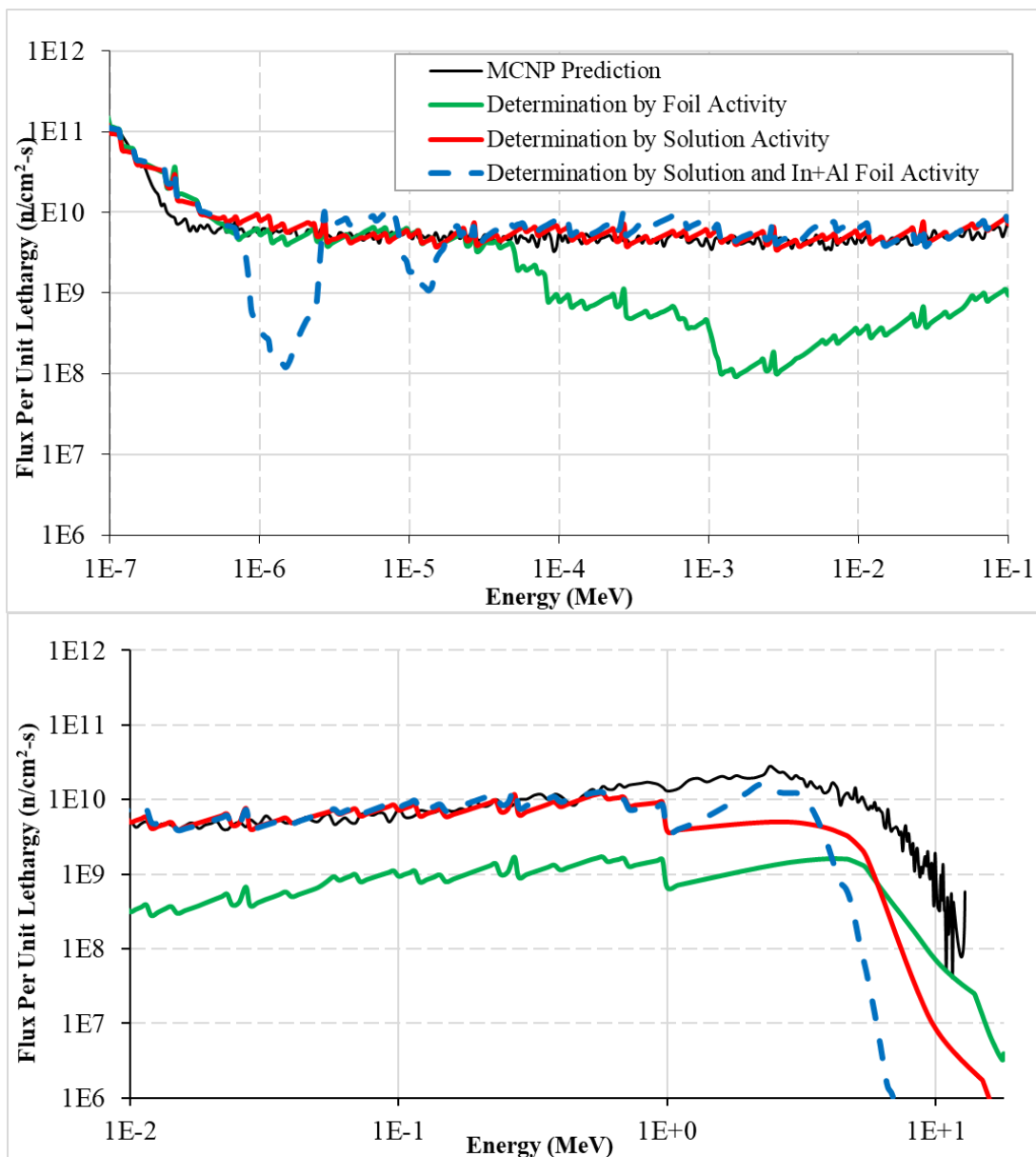


Figure 2.7. Non-Thermal Region of the Spectra: (a) Resonance Energy Region; (b) Fast Energy Region.

This is the subject of further investigation on the impact of self-shielding on the MSTR neutron spectrum. Table 2.5 gives the three-group collapsed neutron flux for the MSTR at the source-holder position for the 120W reactor core configuration for both foils and dilute solutions SAND-II predictions are compared with those for MCNP. Note that

the flux distribution from the dilute solutions closely matches the MCNP prediction better than the foil-based distribution (Alqahtani & Alajo, 2017c).

Table 2.5. MSTR Neutron Flux Distribution as Determined by SAND-II in Source-Holder Tube.

Energy	Foil		Solutions		MCNP	
Thermal	4.47×10^{11}	93.31%	3.36×10^{11}	78.41%	3.81×10^{11}	76.42%
Resonance	2.70×10^{10}	5.63%	6.58×10^{10}	15.37%	6.06×10^{10}	12.15%
Fast	5.11×10^9	1.07%	2.67×10^{10}	6.22%	5.70×10^{10}	11.44%
Total	4.79×10^{11}	100%	4.28×10^{11}	100%	4.99×10^{11}	100%

2.3.3. Bare Rabbit Tube Position. One of the irradiation locations in the MSTR core is the pneumatic sample transfer (rabbit) system. This system consists of two rabbit tubes. One of these tubes does not have a thermal neutron filter and is called the bare rabbit tube (BRT). The tube is positioned in the core and samples can be moved into and out of the core using compressed nitrogen. The advantage of this system is that it allows samples to be positioned in the zone with the maximum neutron flux for a specific time. The BRT is used more frequently than the other tube. The BRT location has not been characterized for the current configuration of the MSTR. Simulations assuming a neutron flux in the BRT were performed using MCNP. Various MCNP spectra for 620-, 143-, 89-, 50-, 22-, and 12-energy groups were used as the initial guess for the SAND-II code to investigate the impact of the initial guess on the MSTR neutron spectrum.

Table 2.6. Specifications and Reaction Information of the Available Foils Used for Bare Rabbit Tube Spectrum.

Foil	Composition	Mass (g)	Reaction	Half-life	Energy range
Indium	In	0.20	$^{115}\text{In}(n,\gamma)\text{In}^{116\text{m}}$	54.29 min	Thermal Epithermal
			$^{115}\text{In}(n,n)\text{In}^{115\text{m}}$	4.48 h	Fast
			$^{113}\text{In}(n,\gamma)\text{In}^{114\text{m}}$	49.50 d	Thermal
Gold	0.134% Au–Al	0.05	$^{197}\text{Au}(n,\gamma)\text{Au}^{198}$	2.69 d	Thermal Epithermal
Aluminum	Al	0.05	$^{27}\text{Al}(n,\alpha)\text{Na}^{24}$	14.99 h	Fast
			$^{27}\text{Al}(n,p)\text{Mg}^{27}$	9.45 min	Fast
Magnesium	Mg	0.20	$^{24}\text{Mg}(n,p)\text{Na}^{24}$	15.06 h	Fast
Titanium	Ti	0.04	$^{46}\text{Ti}(n,p)\text{Sc}^{46}$	83.79 d	Fast
			$^{47}\text{Ti}(n,p)\text{Sc}^{47}$	3.35 d	Fast
			$^{48}\text{Ti}(n,p)\text{Sc}^{48}$	43.67 h	Fast
Vanadium	V	0.05	$^{51}\text{V}(n,\gamma)\text{V}^{52}$	3.74 min	Thermal
Cobalt	Co	0.03	$^{59}\text{Co}(n,\gamma)\text{Co}^{60}$	1925.28 d	Thermal
			$^{59}\text{Co}(n,\alpha)\text{Mn}^{56}$	2.57 h	Fast
Copper	Cu	0.27	$^{63}\text{Cu}(n,\gamma)\text{Cu}^{64}$	12.70 h	Thermal
			$^{63}\text{Cu}(n,\alpha)\text{Co}^{60}$	1925.28 d	Epithermal
			$^{63}\text{Cu}(n,\alpha)\text{Co}^{60\text{m}}$	10.46 min	Fast
			$^{63}\text{Cu}(n,2n)\text{Cu}^{62}$	9.67 min	Fast
Iron	Fe	0.13	$^{58}\text{Fe}(n,\gamma)\text{Fe}^{59}$	44.49 d	Epithermal
			$^{54}\text{Fe}(n,p)\text{Mn}^{54}$	312.20 d	Fast
			$^{56}\text{Fe}(n,p)\text{Mn}^{56}$	2.57 h	Fast
Lutetium	5.2% Lu–Al	0.06	$^{176}\text{Lu}(n,\gamma)\text{Lu}^{177}$	6.64 d	Thermal
Manganese	87% Mn–Cu	0.05	$^{55}\text{Mn}(n,\gamma)\text{Mn}^{56}$	2.57 h	Thermal
Molybdenum	Mo	0.09	$^{98}\text{Mo}(n,\gamma)\text{Mo}^{99}$	65.97 h	Epithermal
Sodium	50% NaCl	0.60	$^{23}\text{Na}(n,\gamma)\text{Na}^{24}$	14.99 h	Thermal
Scandium	Sc	0.05	$^{45}\text{Sc}(n,\gamma)\text{Sc}^{46}$	83.79 d	Thermal
Tungsten	W	0.32	$^{186}\text{W}(n,\gamma)\text{W}^{187}$	24.00 h	Thermal
Nickel	Ni	0.29	$^{58}\text{Ni}(n,p)\text{Co}^{58}$	70.86 d	Fast
Zirconium	Zr	0.11	$^{90}\text{Zr}(n,2n)\text{Zr}^{89}$	78.41 h	Fast

The motivation for this work is the need to characterize the prompt-neutron spectra at other locations in the reactor and to improve the documentation of the neutronic characteristics of the MSTR. Experimental and analytical approaches were used to determine the spectra for a specific location (BRT). The results of the present study will act as a baseline for the reactor, and if necessary, any new experimental facilities that are installed, as well as any irradiation experiments that are conducted.

2.3.3.1. Foil selection. Two identical sets of 17 foils were selected based on the neutron interactions of interest, the foil cross-section, and their availability.

Table 2.7. Foil Cross-Sections and Energy Ranges Used in SAND-II.

Cross-section (barn)	Energy range				
	0.001 – 0.1 eV	0.1 eV – 0.1 MeV	0.1 – 5 MeV	5 – 10 MeV	10 – 18 MeV
< 0.1			$^{27}\text{Al}(n, p)\text{Mg}^{27}$		$^{90}\text{Zr}(n, 2n)\text{Zr}^{89}$ $^{24}\text{Mg}(n, p)\text{Na}^{24}$
0.1 – 1	$^{23}\text{Na}(n, \gamma)\text{Na}^{24}$	$^{23}\text{Na}(n, \gamma)\text{Na}^{24}$	$^{115}\text{In}(n, n)\text{In}^{115\text{m}}$ $^{58}\text{Ni}(n, p)\text{Co}^{58}$	$^{27}\text{Al}(n, \alpha)\text{Na}^{24}$ $^{115}\text{In}(n, n)\text{In}^{115\text{m}}$	$^{46}\text{Ti}(n, p)\text{Sc}^{46}$ $^{63}\text{Cu}(n, 2n)\text{Cu}^{62}$
1 – 10	$^{63}\text{Cu}(n, \gamma)\text{Cu}^{64}$ $^{51}\text{V}(n, \gamma)\text{V}^{52}$	$^{63}\text{Cu}(n, \gamma)\text{Cu}^{64}$ $^{58}\text{Fe}(n, \gamma)\text{Fe}^{59}$ $^{98}\text{Mo}(n, \gamma)\text{Mo}^{99}$			
10 – 100	$^{59}\text{Co}(n, \gamma)\text{Co}^{60}$ $^{197}\text{Au}(n, \gamma)\text{Au}^{198}$ $^{55}\text{Mn}(n, \gamma)\text{Mn}^{56}$ $^{45}\text{Sc}(n, \gamma)\text{Sc}^{46}$ $^{186}\text{W}(n, \gamma)\text{W}^{187}$	$^{59}\text{Co}(n, \gamma)\text{Co}^{60}$ $^{55}\text{Mn}(n, \gamma)\text{Mn}^{56}$			
> 100	$^{115}\text{In}(n, \gamma)\text{In}^{116\text{m}}$ $^{176}\text{Lu}(n, \gamma)\text{Lu}^{177}$	$^{197}\text{Au}(n, \gamma)\text{Au}^{198}$ $^{115}\text{In}(n, \gamma)\text{In}^{116\text{m}}$			

The foil sets for bare foil irradiation and cadmium-covered foil irradiation cover energies from 0.025 eV to 13 MeV for a broad-spectrum analysis. These masses are designed to reduce self-shielding, self-absorption, and other corrections. All foil sets should have a good response and cover the important spectrum energies. Foils with (n, α) and (n, p) reactions are particularly necessary for unfolding fast spectra.

All the reaction cross-sections for the foils were obtained from the ENDF/B-VII.1 Library, and the foil half-lives were obtained from IAEA Nuclear Data Section (ASTM E720-11, 2011; Baum et al., 2002; Chadwick et al., 2006). Table 2.7 lists the reactions and the cross-sections for both cadmium-covered foils and bare foils that cover the neutron energy range used in SAND-II to predict the neutron flux energy for MSTR.

2.3.3.2. Monte Carlo N-particle code. MCNP code version 5 was used to develop a model of the MSTR reactor (Monte Carlo Team, 2003). The model includes the reactor core, all fuel elements, the control rods, the grid plate, the reactor pool, the thermal column, and the activation experiment locations. The MSTR spectrum was obtained using 620-group energy bins in SAND-II. The resulting spectrum was supplied as the initial spectrum guess for input into the SAND-II code. The estimated spectrum was calculated at the exact geometry of the polyethylene vial that was modeled inside the BRT position corresponding to the experiment position within the reactor core in the 120W configuration. The energy of the initial estimated spectrum ranged from 10^{-10} to 18 MeV. Another neutron spectrum with different energy structures was determined using the MCNP model and was also used as the initial guess for SAND-II. In this study, six different energy groups were used as the initial guess for SAND-II, namely, the 620-, 143-, 89-, 50-, 22-, and 12-bin energy groups

from MCNP. The cross-section library for this model uses ENDF/B-VI (.66c) in MCNP5 for all isotopes.

The MCNP code was run as a KCODE criticality calculation performed with 20,000 particles per cycle for 1,050 cycles in total, after discarding the first 50 cycles.

Figure 2.8 shows the MCNP spectrum resulting from this simulation.

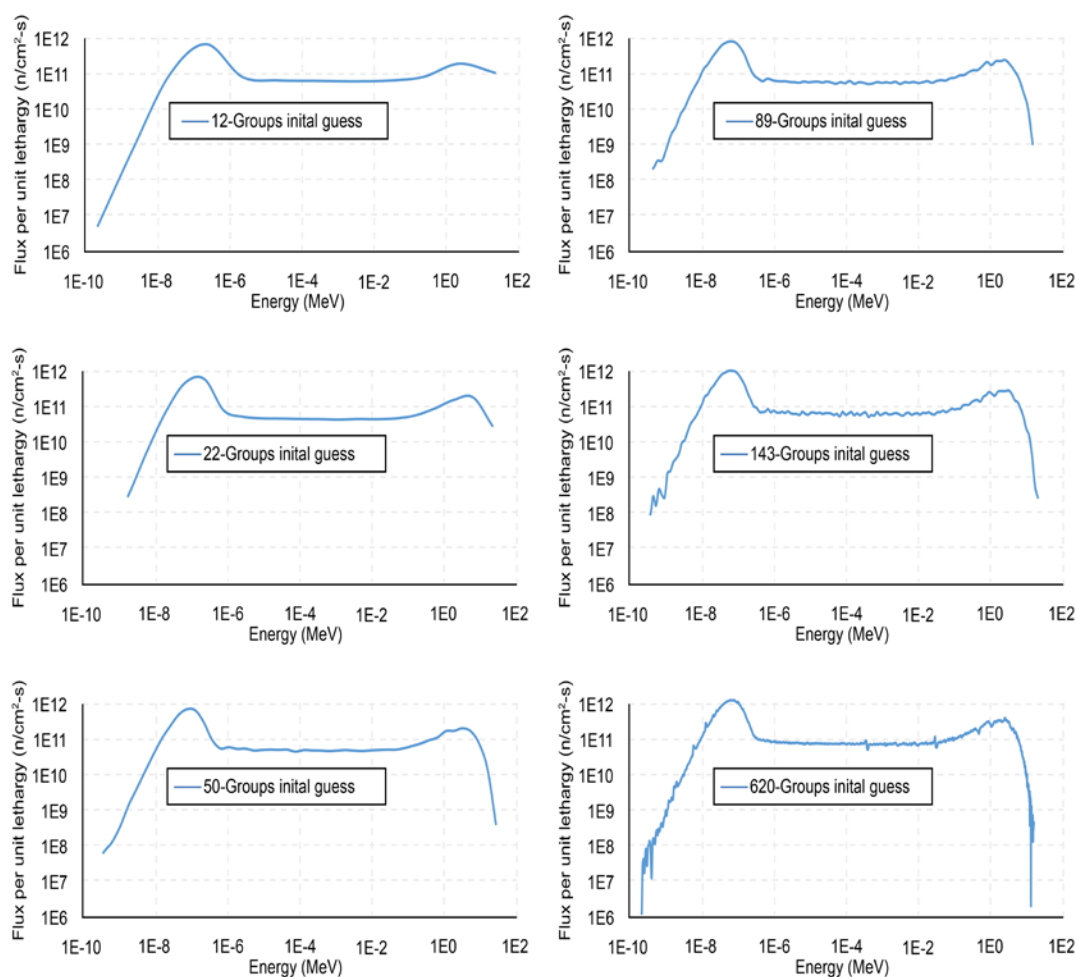


Figure 2.8. MCNP Initial Estimates of Spectra Obtained from the Bare Rabbit Tube (120W).

2.3.3.3. Results. The foil activities were unfolded using the SAND-II code with different initial guess energy groups. The spectrum was unfolded into the same energy binning structure as the MCNP model for the 620-energy group, as well as the 143-, 89-, 50-, 22-, and 12-energy groups, to examine the impact of the initial guess on the results obtained for the neutron flux spectrum. Figure 2.9 compares the MSTR neutron spectra determined by the SAND-II code for each energy group, presented in tabular form for 621 points. The result of the 620-group prediction agrees well with the results of the MCNP calculation.

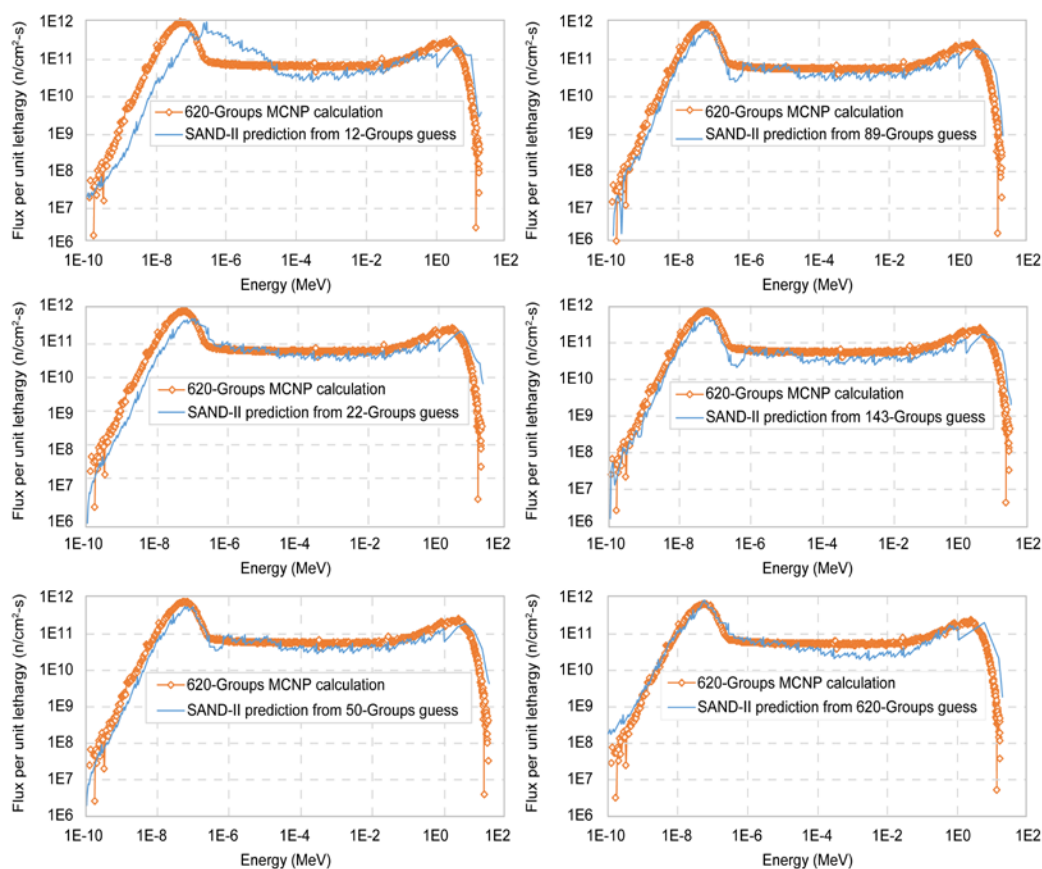


Figure 2.9. MSTR Neutron Flux Spectra at the BRT.

The neutron fluxes, collapsed into three energy groups for the MSTR at the BRT position for the 120W reactor core configuration, are listed in Table 2.8 for each energy group. The relative error for the quality of each group affects the initial guess, with the thermal and fast regions having the largest relative errors among the MCNP errors (see Figure 2.10). The relative error in each bin of an energy group is defined as the ratio of the standard deviation of the flux in the bin to the estimated flux level in the bin.

Table 2.8. MSTR Neutron Flux Distribution as Determined by SAND-II in BRT.

Number of bins in group	MCNP calculation			SAND-II prediction		
	D_{thermal}	$D_{\text{epithermal}}$	D_{fast}	D_{thermal}	$D_{\text{epithermal}}$	D_{fast}
12	52%	23%	25%	38%	36%	26%
22	55%	21%	24%	48%	29%	23%
50	54%	24%	22%	49%	28%	23%
89	54%	23%	23%	49%	26%	25%
143	55%	23%	22%	49%	26%	25%
620	55%	23%	22%	59%	19%	22%

The neutron flux distribution for each group was compared with the results of the MCNP calculation for each region. Disparities were noted in the distribution of the thermal and epithermal-flux predictions as the number of groups in the initial guess changed. The 12-group initial guess resulted in the prediction of a fairly even distribution between the

thermal (38%) and epithermal (36%) fluxes, with differences of no more than 13% in the thermal and epithermal regions and less than 1% in the fast region for the MCNP calculation. The 22-group region exhibits differences in the thermal and epithermal regions of less than 6% and 8%, respectively, and 1.5% in the fast region. The 50-, 89-, and 143-energy groups are reasonably consistent with the results of the MCNP calculation; the thermal distribution is in good agreement within approximately 5% and between 2% to 4% in the epithermal region and approximately 2% in the fast region. The predictions based on the 89- and 143-group guesses are fairly consistent with the predictions obtained with the 22- and 50-group guesses. The 59%/19% distribution of the thermal/epithermal flux, as predicted with the 620-group guess, is inconsistent with the 49%/26% distribution predicted with the 89- and 143-group guesses. The 620-group was considered to be reasonably consistent in that the difference between the MCNP calculation and the SAND-II prediction was 4% in both the thermal and epithermal regions and less than 1% in the fast region. Regardless of the number of groups in the initial guess, the SAND-II prediction is always fairly consistent in the fast energy range. The fast neutron flux ranged between 22% and 26%. MCNP was used to calculate the relative error for each flux energy, with the relative error behavior with the 620-group energy being consistent for energy levels above room temperature and below an energy level of 10.5 MeV.

Figure 2.10 shows the relative error versus the proportion of the bins in the energy groups used for the initial guess. In the 620-bin energy group, approximately 86% of the bins have a relative error of less than 20% and the group is generally considered to be reliable. For the 143- and 89-bin energy groups, 89% and 91% of the bins have a relative error of less than 20%, respectively. In the 50-bin group, 90% of the bins have a relative

error of 20% or less. For the 22-bin and the 12-bin groups, 95% and 91% of the energy bins have a relative error of less than 20%, respectively.

The relative error of the flux distribution increased in the thermal and fast energy regions of each energy group in the MCNP simulation. The 620-bin flux predicted by MCNP requires a considerable amount of computing time and many histories to estimate a neutron flux with an acceptable relative error.

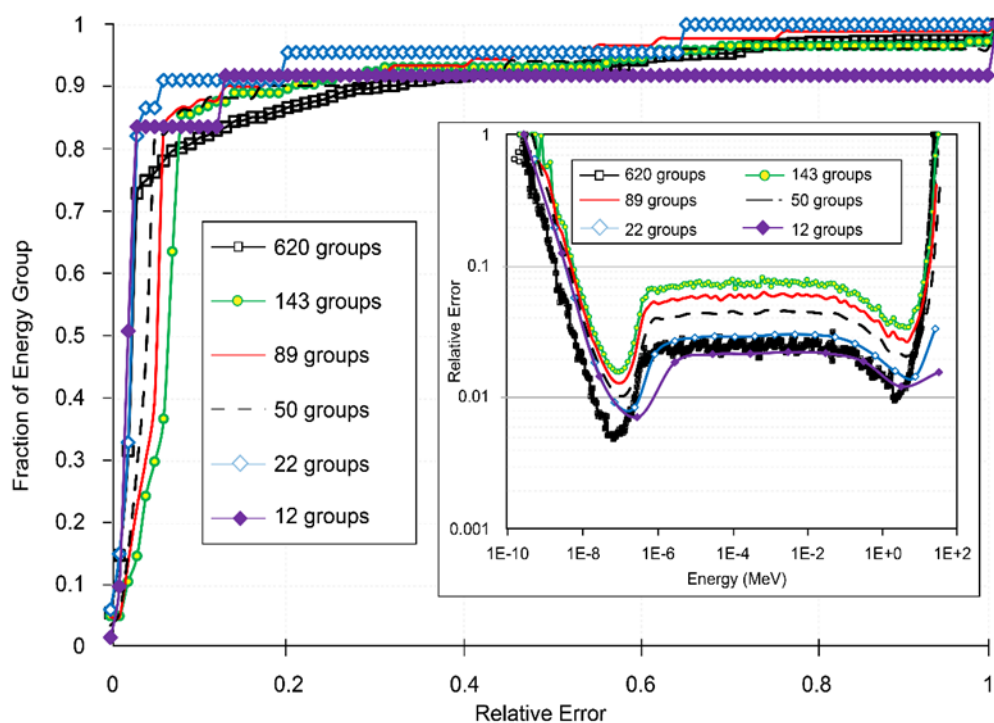


Figure 2.10. Cumulative Distribution of the Relative Error in the Fluxes for Energy Groups.

A total of 14% of both the low- and high-energy ranges of the spectrum have a relative error of more than 20%. The thermal energy range, from 0 eV to 0.55 eV, accounted for 31% of the total relative error. The epithermal energy range, from 0.55 eV

to 0.1 MeV, accounted for 9% of the relative error. The fast energy range, from 0.1 MeV to 18 MeV, has 60% of the total relative error.

The thermal-fluxes of the 620-group energy predicted by SAND-II and the MCNP calculation at the BRT location were $1.43 \times 10^{12} \pm 2.82 \times 10^{11} \text{ n cm}^{-2} \text{ s}^{-1}$ and $1.72 \times 10^{12} \pm 1.25 \times 10^{10} \text{ n cm}^{-2} \text{ s}^{-1}$, respectively. The epithermal-fluxes, as predicted by SAND-II and the MCNP calculation, were $4.51 \times 10^{11} \pm 2.85 \times 10^{10} \text{ n cm}^{-2} \text{ s}^{-1}$ and $7.29 \times 10^{11} \pm 2.68 \times 10^{10} \text{ n cm}^{-2} \text{ s}^{-1}$, respectively. The fast-fluxes determined with the SAND-II and MCNP calculation were $5.38 \times 10^{11} \pm 4.85 \times 10^9 \text{ n cm}^{-2} \text{ s}^{-1}$ and $6.94 \times 10^{11} \pm 1.06 \times 10^{10} \text{ n cm}^{-2} \text{ s}^{-1}$, respectively. The total neutron fluxes obtained by the SAND-II prediction and the MCNP calculation were $2.42 \times 10^{12} \pm 3.02 \times 10^{11} \text{ n cm}^{-2} \text{ s}^{-1}$ and $3.14 \times 10^{12} \pm 3.97 \times 10^{10} \text{ n cm}^{-2} \text{ s}^{-1}$, respectively.

3. CONCEPTUAL DESIGN OF THE BEAM-PORT SYSTEM

3.1. MULTI-SPECTRA UNDERWATER BEAM-PORT

The design and characterization of the beam-port system for the MSTR are easily replicated for any other pool-type research reactor (Figure 3.1). Especially if space is restricted, such a facility within the reactor pool saves space. More importantly, any reactor facility can use it to expand its research capabilities. It is a future-proof facility for a reactor system, since the beam tubes and reactor core can be redesigned for specific flux characteristics without the attendant limitations of the traditional beam-port design.

MCNP code version 5 (Monte Carlo Team, 2003) was used to develop a model of the MSTR. The model includes the reactor core, all fuel elements, the control rods, the grid plate, the reactor pool, the thermal column, and the activation experiment locations. Each of the tasks listed in Section 1.11 for the characterization of the beam-port system used the MCNP transport code. The existing MCNP5 model of the MSTR was modified to include the beam-port system.

The new (modified) model was used to analyze beam-tube designs and to perform optimization calculations where necessary. The energy bins ranged from 10^{-10} to 18 MeV. The F4 tally was used to obtain the neutron flux in the beam-port optimizations. The cross-section library for this model was ENDF/B-VI (.66c) in MCNP5 for all isotopes. A KCODE criticality calculation was performed with 20,000 particles per cycle for 30,050 cycles in total, after discarding the first 50 cycles.

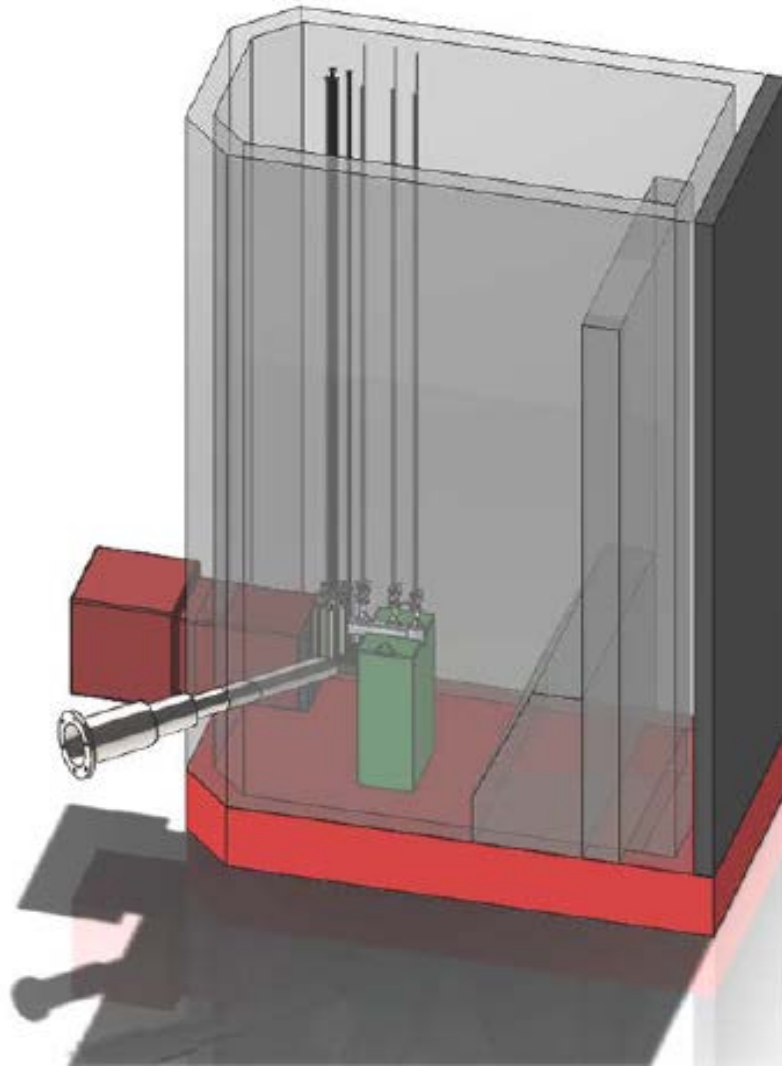


Figure 3.1. Side View of the MSTR and the Beam-Port System.

3.2. DESIGN OF THE BEAM-PORT SYSTEM

This section is devoted to the beam-port design, the beam-port components and material selections, reactor core modifications, beam-port tube design for specific particle type, and neutron spectra for each beam-port.

3.2.1. General Components. As mentioned in Section 1, the neutron beam in a beam-port depends on many factors, including the size and shape of the beam-port as well as the location and orientation of the beam-port with respect to the reactor core, the core–

moderator configuration, the reflectors, and the filter and collimator in the beam-port. Each of these factors needs to be well defined to characterize the neutron beam. The underwater beam-port system was designed to be portable so that it can be moved into and out of the reactor pool. The underwater beam-port system consists of three main components that can be adapted for any type of particle transport and energy spectrum (Figure 3.2).

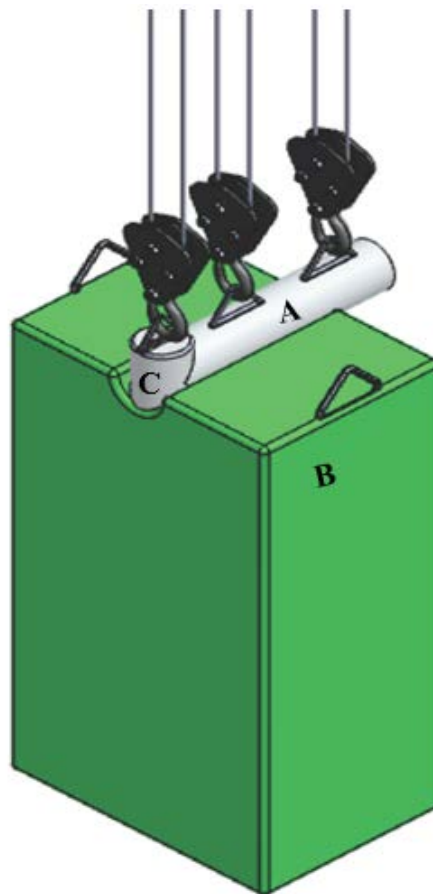


Figure 3.2. Beam-Port System, Showing the Beam-Port (A), the Movable Base (B), and the Target Delivery System (C).

Each of these components has been optimized to obtain the best material and size for a given particle energy.

3.2.2. Beam-Port Tube. The first component is the beam-port tube (Figure 3.3). It allows neutrons to pass from the reactor core to the sample irradiation system (target delivery system). The tube is made of aluminum 6061 and has a length of 73.2 cm. The diameter of the beam-port tube was optimized to give the best neutron flux at the sample irradiation system. The beam-port tube runs horizontally along the centerline of the reactor core. It has neutron filters to facilitate spectral morphing and particle discrimination for each particle energy spectrum. At the reactor core end, the tube is designed so that it is close to several active fuel elements (Figure 3.4).

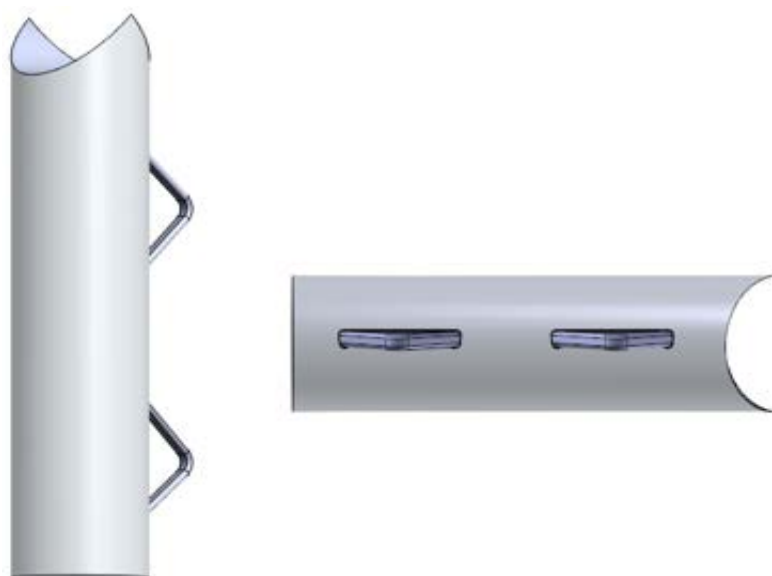


Figure 3.3. Beam-Port Tube.

This design permits a high intensity of neutrons to pass from the fuel elements into the beam-port tube before they are thermalized. The other end of the tube is sculpted to fit around the target delivery system to reduce the gap between them. The curved end of the beam-port was designed to reduce any neutron scattering that might occur between the two tubes. The beam-port tube fits into a groove on the movable base, which ensures it remains

steady relative to both the reactor core and the target delivery system. The beam-port has two lifting lugs, allowing it to be removed when not in use.

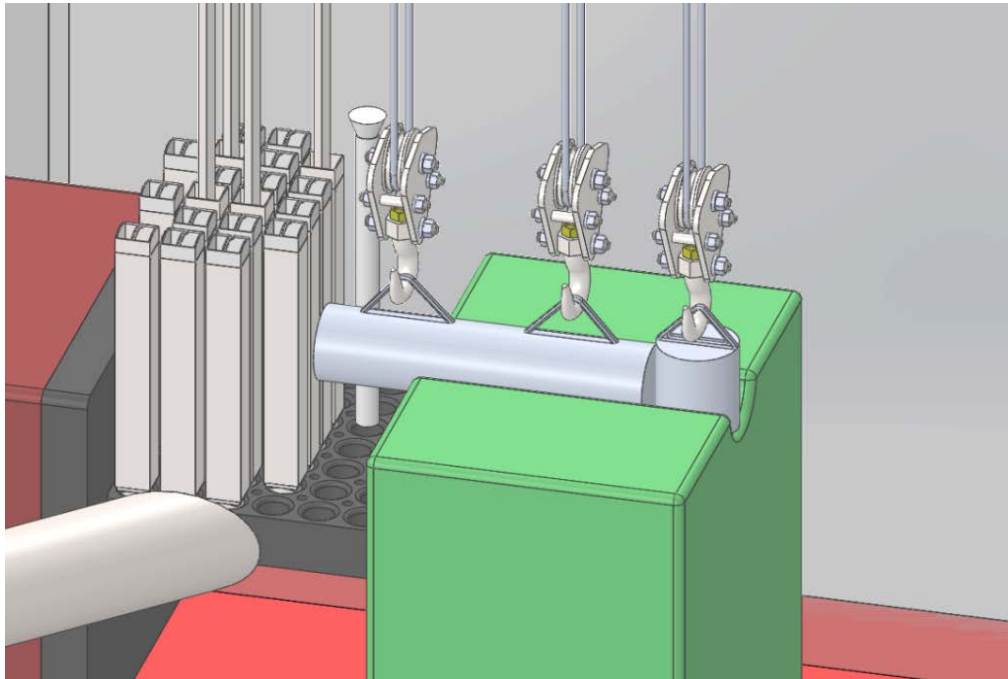


Figure 3.4. Beam-Port in the Core.

3.2.3. Movable Base. The second component is the movable base, onto which both the beam-port and the target delivery system are installed. The base is made of borated polyethylene, which provides shielding from fast neutrons and gamma-rays (Figure 3.5)(Elmahroug, Tellili, & Souga, 2013). It is used as biological shielding for the target delivery system from the core irradiation. This base has two lifting lugs, so that it can be removed when not in use. The dimensions of the base were selected to place the beam-port on the height where is the height of the active fuel is parallel to it and fit for both beam-port and target delivery.

The dimensions are 100 cm (length) \times 70 cm (width) \times 171.35 cm (height). The movable base is higher than the core grid plate to align the beam-port with the reactor centerline (Figure 3.4). At the end of the groove in the movable base, there is a 17.98-cm-diameter hole into which the target delivery system is inserted. Its specifications are listed in Table 3.1.

Table 3.1. Technical Specifications.

Target Delivery System	
Height	92.4 cm
Diameter	17.6 cm
Material	Aluminum alloy
Movable Base	
Height	135.16 cm
Length	100 cm
Width	70 cm
Material	5% borated polyethylene, high density

3.2.4. Target Delivery System. This is a tube with an inner diameter of 17.6 cm and a height of 92.4 cm. The top of the tube has a removable cap, allowing the irradiation sample to be moved in and out. The tube is inserted into the curved end of the beam-port to avoid the thermalization of the neutrons by the water (Figure 3.6). The tube has one lifting lug that allows the tube to be moved. The specifications are given in Table 3.1.

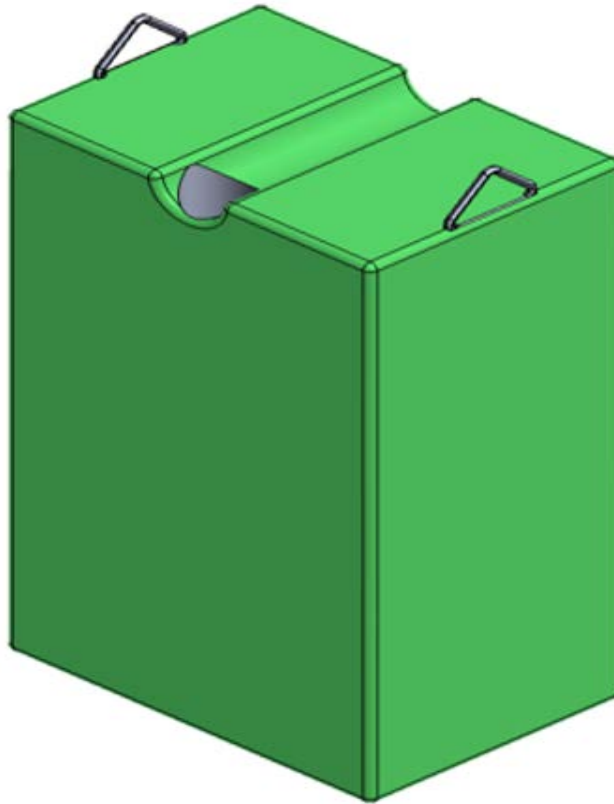


Figure 3.5. Movable Base.

3.3. MODIFICATION TO MSTR CORE LAYOUT

The MSTR core was modified for two reasons; to ensure that the reactor maintained critical after installing the beam-port system to the reactor pool and to enhance the neutron flux at the reactor side.

3.3.1. Criticality. The MSTR core was modified to ensure there was adequate excess reactivity after the introduction of the beam-port system into the reactor pool. After installing the new beam-port, the criticality was calculated at the 120W configuration. The effective multiplication factor decreased to 0.99585 ± 0.00018 , initially, one new fuel element was added at the position C9 to maintained critical (Figure 3.7). The MCNP

calculation showed that K_{eff} increased to 1.005 ± 0.00017 at 200 kW. Hence, another fuel element was added to position C4 and K_{eff} increased to 1.01426 ± 0.00017 at full power. The beam-port was designed and characterized with a core configuration of 120W by adding a fuel element on the position C9.

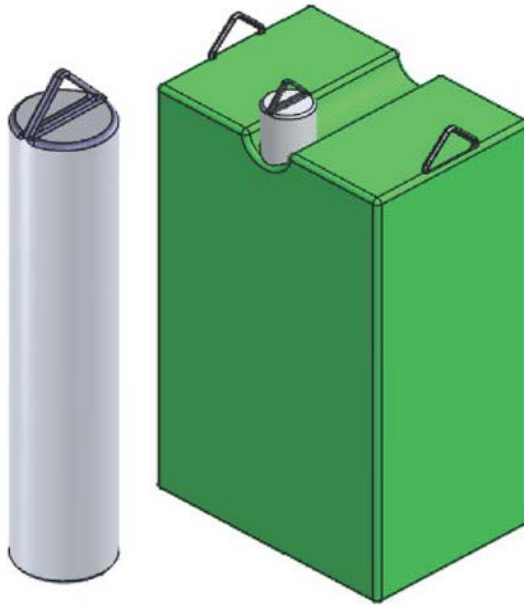


Figure 3.6. Target Delivery System.

The additional fuel elements at this position increased the neutron flux in the target delivery system and remain the reactor critical. Furthermore, adding more fuel elements at this position proves to be advantageous to the beam-port.

3.3.2. Conceptual Fast Neutron Island. To enhance the quality of the neutron spectrum at the reactor side of the beam-port, a new fast island was investigated for the reactor core. At the center of the island is the core access element (CAE). The objective is to improve the fast neutron intensity in the CAE by replacing the water moderator of the three fuel elements immediately surrounding it with Zircaloy.

	1	2	3	4	5	6	7	8	9
A									
B						S			
C					-4	F-5	F-1	F-17	
D				F-4	F-8	F-14	C-1	F-10	F-2
E				F-9	C-3	F-12	C-2	F-7	F-3
F				CRT	F-15	HC	F-13	BRT	F-6

Figure 3.7. MSTR Core Configuration (Modified).

The deployment of the fast island in the reactor core provides a fast neutron flux for experimental purposes, thereby expanding the research capabilities of the MSTR. This design permits fast neutrons emanating from the fuel elements to enter the island before they are thermalized. The design is relatively portable, so that the island can be moved into and out of the pool. MCNP was used to simulate the MSTR core and the new CAE. The MCNP model was used to evaluate the fast neutron island and CAE configuration to obtain the optimum neutron flux at the core access element (Alqahtani & Alajo, 2017a).

3.3.2.1. Fuel element redesign. The water in the gaps (~0.315 cm) between the plates of three fuel elements was replaced with Zircaloy to temper the moderation (Figure 3.8). This helps to improve the fast neutron flux at the core access element (Alqahtani & Alajo, 2017a). The MCNP model used to redesign the fuel element moderator to obtain the neutron flux at the core access element.

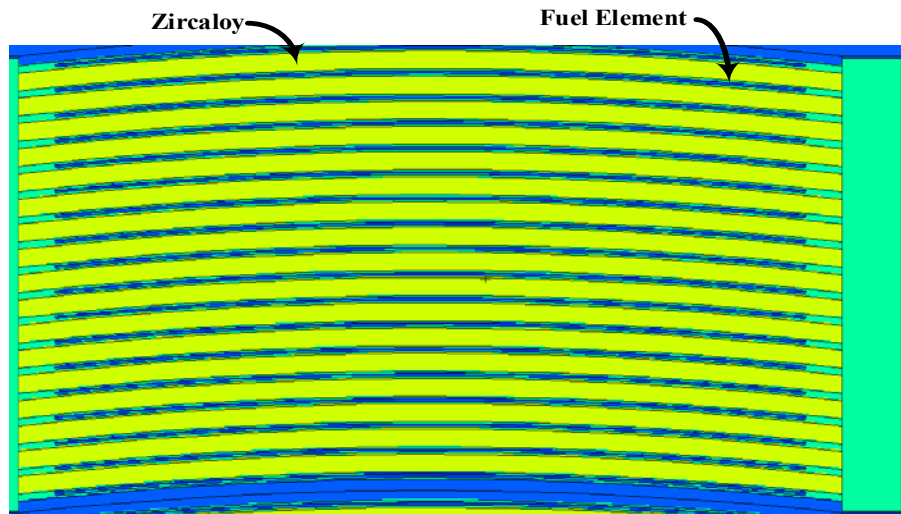


Figure 3.8. Fuel Element with Zircaloy.

3.3.2.2. Core access element. The CAE is similar in shape to a fuel element (Figure 3.9) (Bonzer & Carroll, 2008). It has a central cylindrical cavity filled with air to accommodate irradiation samples.

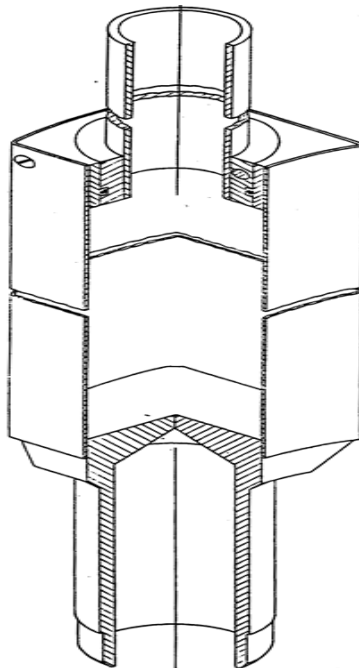


Figure 3.9. Core Access Element.

The end of the element slots into the grid plate and can be used in different positions in the core. The existing CAE, which is clad in aluminum, is made of graphite and is unfueled. The new CAE has no graphite to prevent thermalization and a cadmium lining to eliminate thermal neutrons (Alqahtani & Alajo, 2017a).

3.3.2.3. Simulations. MCNP was used to calculate the spectrum in the CAE using 620-bin energy groups. Spectra with both water and Zircaloy moderators were compared. Three scenarios for the CAE were modeled for the neutron flux spectrum inside the fast neutron island, as shown in the flow chart in Figure 3.10.

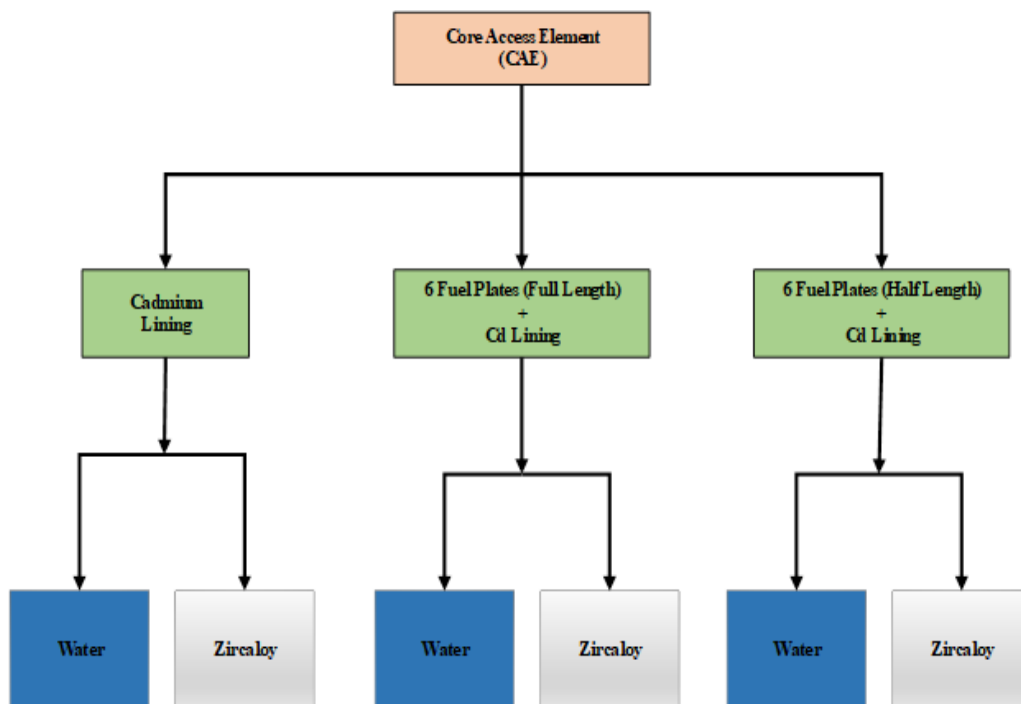


Figure 3.10. Flowchart for CAE Simulations.

In each scenario, the use of water and Zircaloy as the moderator in the three surrounding fuel elements are compared. In the first scenario, the CAE has no fuel plates.

In the second scenario, the CAE has six full-length fuel plates. In the third scenario, the CAE has six half-length fuel plates (Figure 3.11) (Alqahtani & Alajo, 2017a).

3.3.2.4. Results. Figure 3.12 compares the neutron spectra in the CAE for the three scenarios. In each scenario, the spectra are mainly identical, but the flux is higher in the fast region when Zircaloy is used as the moderator. There is a shift in the neutron flux due to the removal of the water moderator and the reduction in thermalization.

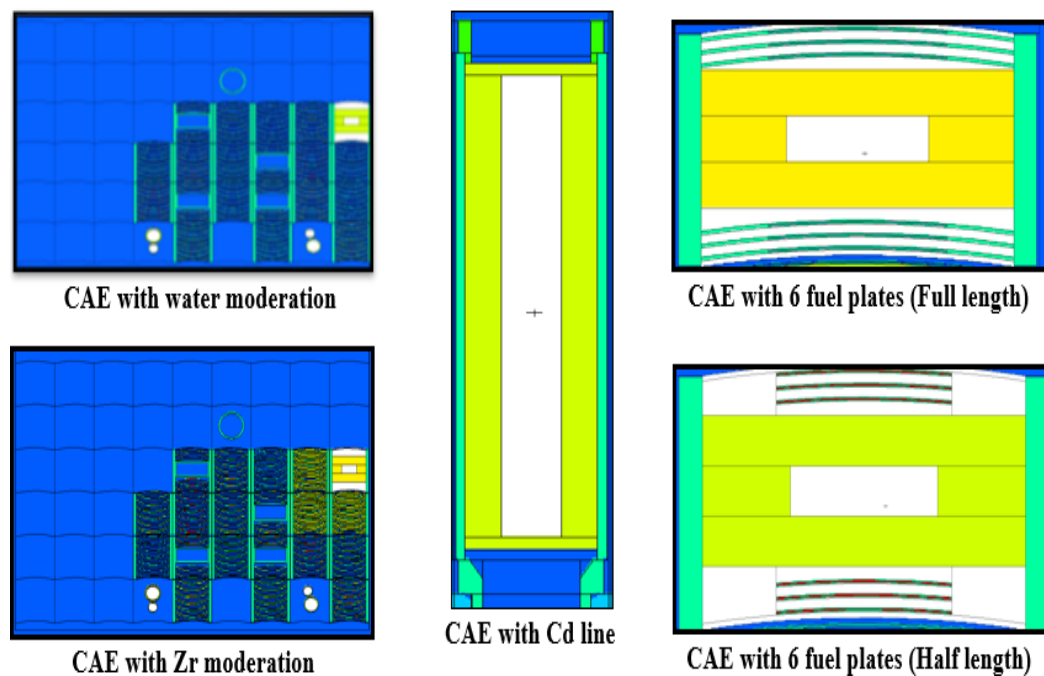


Figure 3.11. Core Access Element Simulations.

The fast neutrons in the CAE with six full-length fuel plates were $1.06 \times 10^{12} \text{ n cm}^{-2} \text{ s}^{-1}$ the total flux using Zircaloy as the moderator, and $5.61 \times 10^{11} \text{ n cm}^{-2} \text{ s}^{-1}$ of the total flux with the water as moderator. The fast-flux determined with six half-length fuel plates were $1.04 \times 10^{12} \text{ n cm}^{-2} \text{ s}^{-1}$ of the total flux using Zircaloy as moderator, and $5.38 \times 10^{11} \text{ n cm}^{-2} \text{ s}^{-1}$ with water moderator.

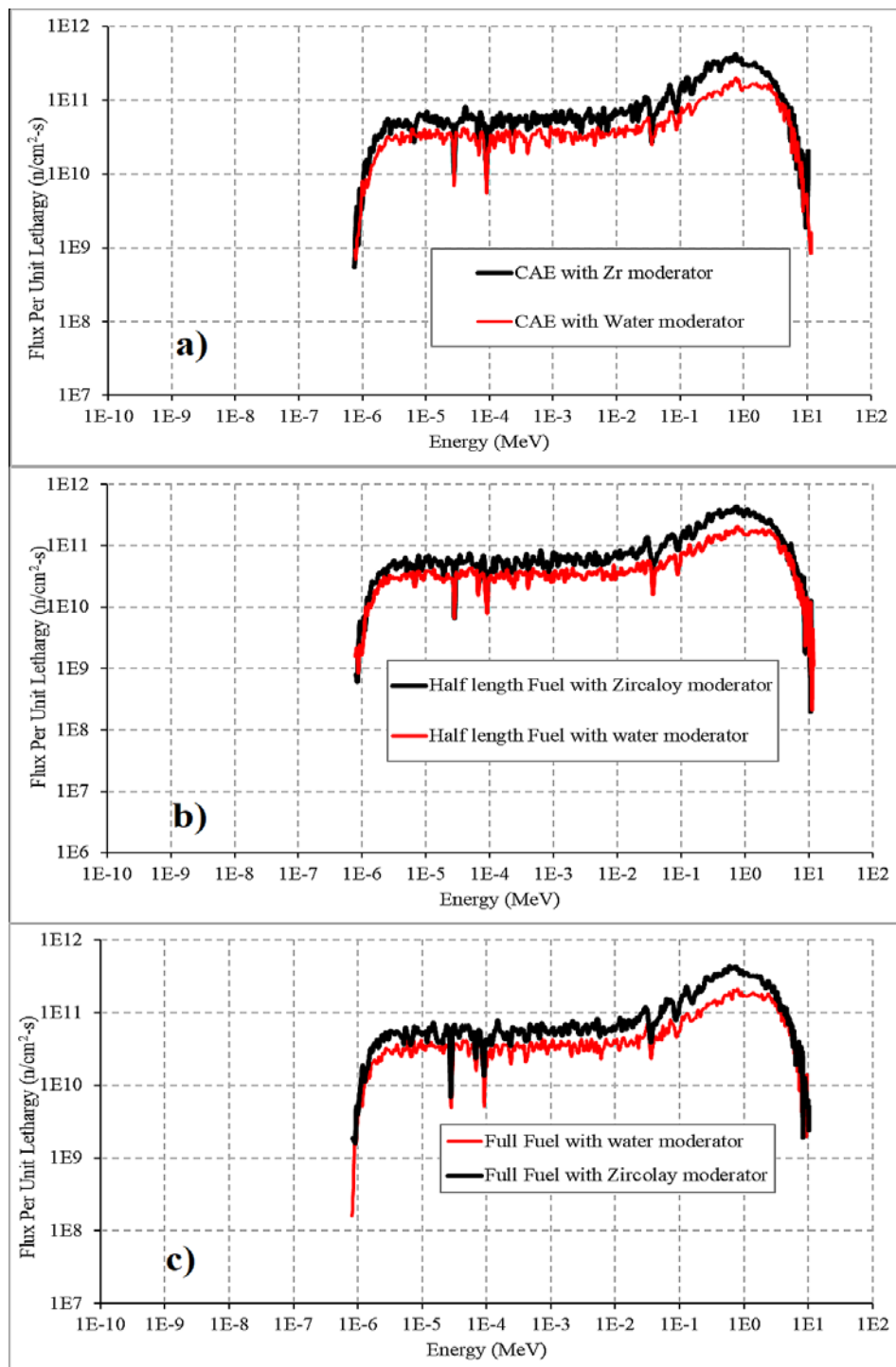


Figure 3.12. Neutron Flux Spectra in the Core Access Element (CAE):
 (a) CAE Moderated by H₂O or Zr. (b) CAE with Full-Length Fuel Plates.
 (c) CAE with Half-Length Fuel Plates.

The results are summarized in Table 3.2. The fast neutron flux in CAE improved when Zircaloy was used as the moderator. The fast-flux increased by 49% with Zircaloy used in CAE compared with the use of water as the moderator, and the fast-flux increased by 52% when six full-length fuel plates in the CAE were employed compared with the original design of the fast island that was moderated with water.

Table 3.2. Neutron Flux Distribution in CAE as Determined by MCNP.

Core Access Element				
Energy	With Water		With Zircaloy	
Thermal	0.00E+00	0.0%	0.00E+00	0.0%
Epithermal	3.85E+11	43.2%	6.70E+11	40.1%
Fast	5.07E+11	56.8%	1.00E+12	59.9%
Total	8.93E+11	100.0%	1.67E+12	100.0%
CAE with 6 fuel plates (Full length)				
Energy	With Water		With Zircaloy	
Thermal	0.00E+00	0.0%	0.00E+00	0.0%
Epithermal	3.95E+11	41.3%	6.76E+11	38.9%
Fast	5.61E+11	58.7%	1.06E+12	61.1%
Total	9.56E+11	100.0%	1.74E+12	100.0%
CAE with 6 fuel plates (Half length)				
Energy	With Water		With Zircaloy	
Epithermal	0.00E+00	0.0%	0.00E+00	0.0%
Resonance	3.91E+11	42.1%	6.80E+11	39.5%
Fast	5.38E+11	57.9%	1.04E+12	60.5%
Total	9.29E+11	100.0%	1.72E+12	100.0%

Table 3.3 shows the improvement of the fast-flux associated with each moderator for all the three scenarios.

Table 3.3. Fast Neutron Flux Improvement in CAE with Moderators.

Moderator	CAE	CAE with 6 Full-Length Fuel plates	CAE with 6 Half-Length Fuel plates
Zircaloy	1.00×10^{12}	1.06×10^{12}	1.04×10^{12}
Water	5.07×10^{11}	5.61×10^{11}	5.38×10^{11}
Improvement	49%	47%	48%

3.3.2.5. Concluding thoughts. The modified fuel element showed better neutronic performance than the regular fuel element while being used as a fast-island facility. However, there are challenges related to the deployment of the modified element as conceived. The modification presents the fuel element as a monolithic structure without any passages for coolant flow. This raises an important issue related to heat removal from the fuel element. Also, a fuel element comprising alternating laminates of fuel plates and Zircaloy plates presents a potential for delamination; this would damage the fuel element. It will be interesting to investigate the usage of the modified fuel element at a low power because this may mitigate the negative issues that have been discussed herein.

3.4. OPTIMIZATION OF THE BEAM-PORT

MCNP was used to simulate and optimize the beam-port, in particular for MSTR, which is an open-pool reactor. The process had four phases.

- Selection of the beam-port position
- Selection of the beam-port
- Selection of the moderator material and thickness
- Selection of the shielding material.

3.4.1. Selection of the Beam-Port Position. Two different positions were evaluated as potential location for the beam-port (Figure 3.13). The neutron flux was calculated for a 12.6-cm-diameter collimated beam-port 62.25 cm in length with no neutron filters. The space in front of the reactor core is designed to give the beam-port the possibility of moving into the reactor pool. The MSTR beam-port is on the right side of the reactor core, which prevents the possibility of selecting this position. The distance from the left-side reactor wall is only 102 cm, which is a severely limited amount of space for the beam-port because the movable base length is 100 cm. These considerations limited the beam-port position to the two shown in Figure 3.13.

	1	2	3	4	5	6	7	8	9
A					Position 1			Position 2	
B						S			
C					-4	F-5	F-1	F-17	
D				F-4	F-8	F-14	C-1	F-10	F-2
E				F-9	C-3	F-12	C-2	F-7	F-3
F				CRT	F-15	HC	F-13	BRT	F-6

Figure 3.13. Optimization of the Beam-Port Position.

The initial dimensions of the beam-port were selected to evaluate the better position for optimizing neutron flux. The diameter of the beam-port was selected to be larger than the fuel element width and cover more than the fuel element. Using 12.6 cm initially was a good assumption for the beam-port design, which was assumed based on the MSTR beam-port diameter (Bonzer & Carroll, 2008).

The length of the beam-port was selected to provide sufficient distance between the reactor core and delivery target location to reduce the neutron flux that is discharged from the reactor pool. Table 3.4 shows the MCNP calculations for two positions that were selected for the beam-port.

Table 3.4. Neutron Flux for the Beam-Port Positions.

Energy	Thermal-flux (n cm ⁻² s ⁻¹)	Epithermal-flux (n cm ⁻² s ⁻¹)	Fast-flux (n cm ⁻² s ⁻¹)	Total flux (n cm ⁻² s ⁻¹)
Position 1	2.39×10^9	8.33×10^8	7.62×10^8	3.99×10^9
Position 2	3.07×10^9	1.23×10^9	1.11×10^9	5.41×10^9

Thermal range: 0 to 0.55 eV; epithermal range: 0.55 eV to 0.10 MeV; fast range: >0.10 MeV

The first position was selected to be in the middle of the reactor core, located to the left of the source-holder tube. The second position was selected to face more than one fuel element. The better beam-port position was determined from the total neutron flux in the target delivery. As shown in Table 3.4, position 2 has a higher neutron flux by 26% since it is close to more fuel elements than position 1. Moreover, the advantage of this position

is a fuel element will be added to C9 to maintain the reactor criticality with the implementation of the beam-port (Section 3.2.1).

3.4.2. Selection of the Beam-Port Tube. The beam-port is a hollow tube that gives free path for neutrons to pass through to the experiment facility. The beam-port is significant for the neutrons beam desired direction. The flux depends on the size and shape of the beam-port. Since the beam-port position was evaluated with beam diameter 12.6 cm (Section 3.3.1) the analysis of the tube diameter's impact started with the same size. The diameter of the beam-port was varied from 12.6 to 17.24 cm.

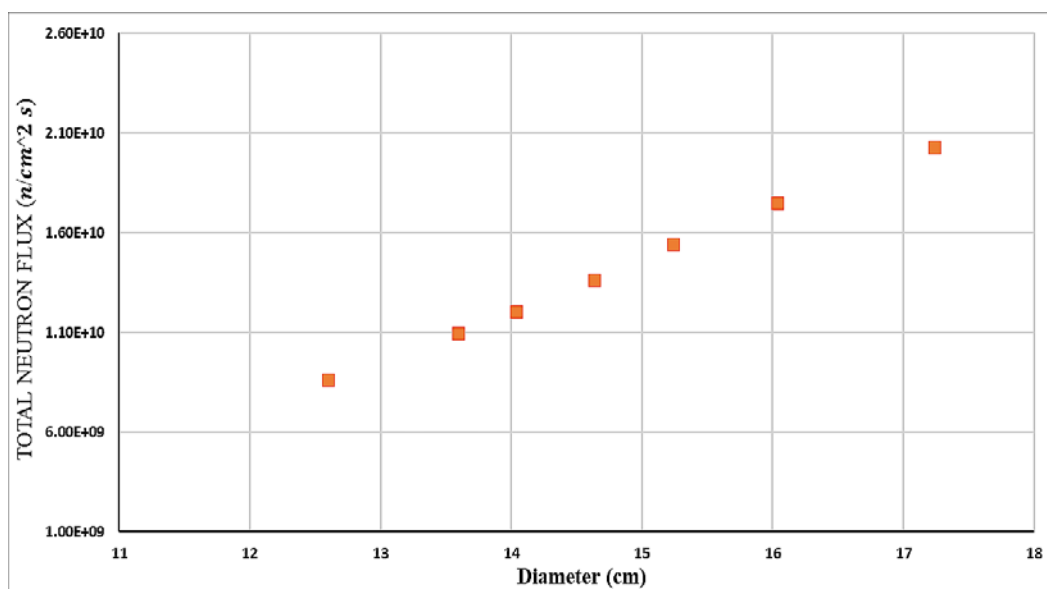


Figure 3.14. Effect of Beam-Port Diameter on the Neutron Flux.

A goal of 2×10^{10} n.cm⁻²s⁻¹ was set as the desired neutron flux at the target region subject to critical core configuration. The diameter of the beam-port must support adequate neutron flux in the target delivery location. Increasing the tube diameter reduces the excess reactivity in the core due to the displacement of water by the void. The selected diameter is 17.24 cm, which satisfies the neutron flux goal while the reactor can still maintain

criticality (see Figure. 3.14). Table 3.5 shows the calculations of K_{eff} for the evaluated diameters.

Table 3.5. K_{eff} Values for Beam-Port with Different Diameters.

Diameter (cm)	Total Flux (n cm ⁻² s ⁻¹)	K_{eff} with Void	K_{eff} with Flooding Withdrawn Control Rod	K_{eff} with Flooding Control Rod Inserted
12.6	$8.61 \times 10^9 \pm 1.89 \times 10^8$	1.00930	1.01397	0.97635
13.6	$1.09 \times 10^{10} \pm 2.10 \times 10^8$	1.00848	1.01326	0.97727
14.04	$1.20 \times 10^{10} \pm 2.23 \times 10^8$	1.00847	1.01436	0.97618
14.64	$1.36 \times 10^{10} \pm 2.33 \times 10^8$	1.00809	1.01315	0.97422
15.24	$1.54 \times 10^{10} \pm 2.48 \times 10^8$	1.00678	1.01374	0.97310
16.04	$1.75 \times 10^{10} \pm 2.66 \times 10^8$	1.00654	1.01401	0.97566
17.24	$2.03 \times 10^{10} \pm 2.82 \times 10^8$	1.00515	1.01398	0.97500

Moreover, the K_{eff} has been calculated in case the beam-ports suffer damage leading to water-ingress into the tube. The calculation was performed for cases with all control rod fully withdrawn and one control rod fully inserted. The results showed that while the reactor's excess reactivity increases with water-ingress, the reactor would be effectively shut-down with the insertion of one control rod.

Simulations were performed with varying beam tube length. A length of 72.25 cm was chosen as the length for the beam-port in this study for two reasons:

1. To provide sufficient distance between the core and target delivery such that without the beam-port, neutrons from the core cannot reach target delivery: The length was

determined to ensure that the neutron flux in the target delivery system is from the beam-port. The neutron flux in the target delivery system that did not arrive via beam-port was low enough.

2. To provide sufficient space within the beam-port for a neutron or photon moderator and filters: Since the beam-port end is close to the fuel elements, a thick moderator and neutron filter are needed.

3.4.3. Optimization of the Beam-Port for a Thermal-Flux. The beam-port was designed to have a high ratio of thermal neutron flux in the target delivery system. The design will include neutron moderator and filters for neutron and photons.

3.4.3.1. Moderator material in the beam-port. A moderator is placed in the front part of the beam-port to thermalize the neutron flux before it reaches the target delivery tube. The moderator parameters investigated included the moderator material, moderator thickness, fast neutron filter, and gamma-ray filter. Several materials were evaluated as moderators: aluminum, borated polyethylene, high-density polyethylene, beryllium, and graphite. The objective was to produce a high intensity of thermal neutrons with a low intensity of fast and epithermal neutrons at the far end of the beam-port and the target delivery tube. The optimum moderating material should have a high-neutron-scattering cross-section, a low-neutron-absorption cross-section, and a low atomic number. The figure of merit for the neutron moderator is the moderating ratio:

$$M = \xi (\Sigma_s / \Sigma_a) \quad (7)$$

where Σ_s is the scattering cross-section, Σ_a is the absorption cross-section, and ξ is the average logarithmic energy decrement:

$$\xi = 2 / (A_m + \frac{2}{3}) \quad (8)$$

where A_m is the atomic mass number(Lamarsh & Baratta, 2001). Figure 3.15 shows that beryllium and graphite are suitable for decreasing the number of fast neutrons while causing less attenuation of thermal neutrons.

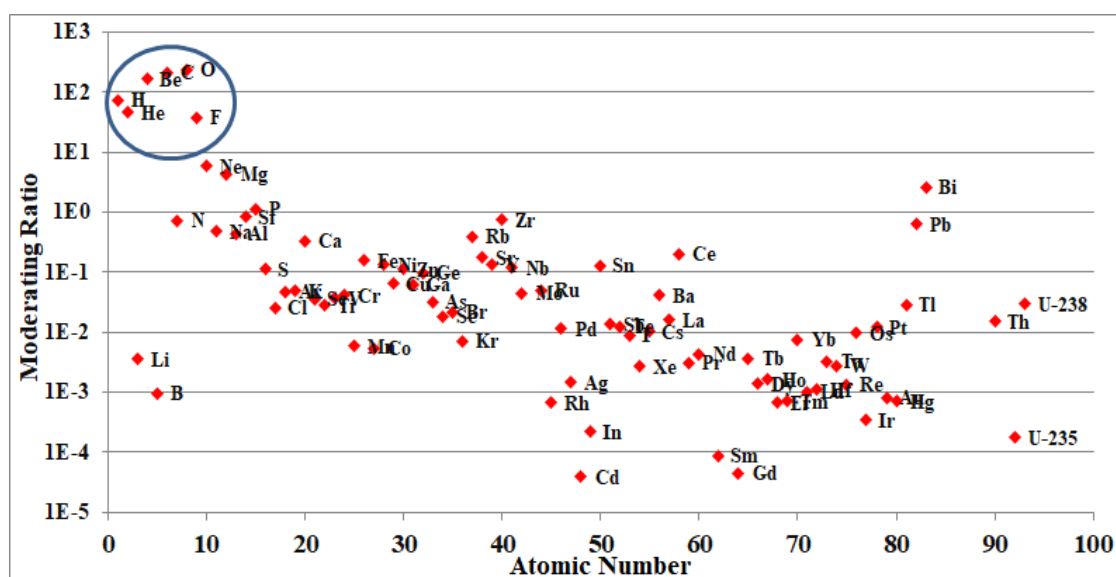


Figure 3.15. Moderating Ratio for Moderator Material.

Both materials are solids, so they will keep their shape if the beam-port becomes damaged. Furthermore, these materials have a good resistance to radiation damage. Beryllium has a higher scattering cross-section than graphite and a lower absorption cross-section. For this design, beryllium was selected as the moderator for the beam-port (Azevedo, 2011).

3.4.3.2. Moderator thickness. The optimal thickness depends on the ratio of the flux of thermal neutrons to the flux of fast neutrons at the end of the beam-port. The thickness of beryllium was varied from 5 to 22 cm.

As shown in Figure 3.16, the ratio of the thermal to fast neutron flux increased as the thickness of the beryllium increased until the thickness reached 22 cm, and the ratio

subsequently decreased. A thickness of 21 cm was selected for the beryllium moderator and used for the beam-port.

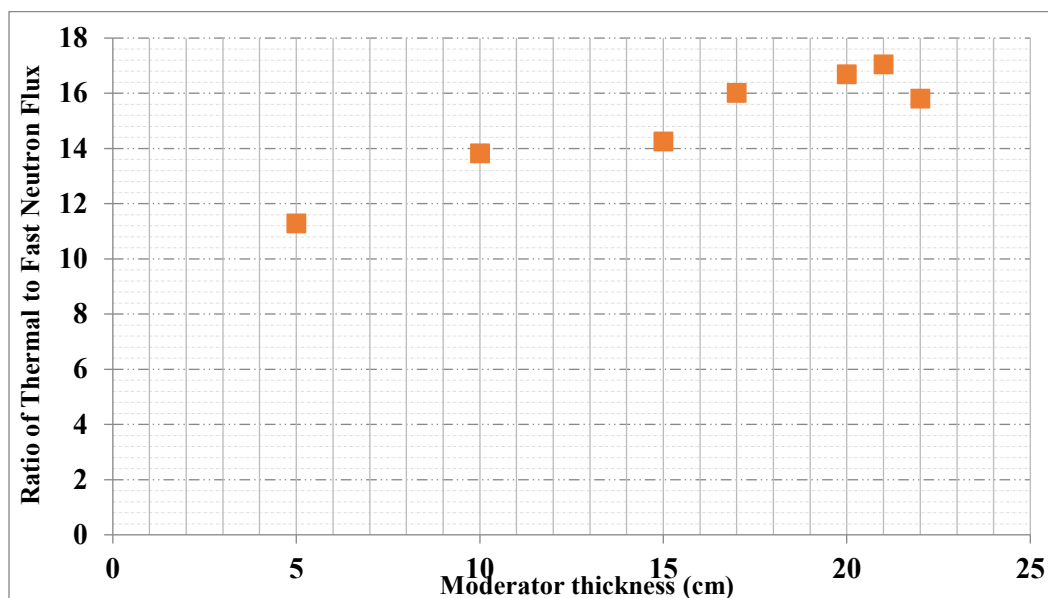


Figure 3.16. Ratio of Thermal Neutron Flux to Fast Neutron Flux at the End of the Beam-Port vs. Beryllium Thickness.

The thermal-flux and the ratio of thermal-flux to total neutron flux for the evaluated thicknesses were calculated in the target delivery and are represented in Table 3.6

3.4.3.3. Fast neutron filter for the thermal beam-port. Some of the high-energy neutrons will pass through the beryllium filter, so a fast neutron filter is required. Several materials were evaluated for the fast neutron filter, such as aluminum and silicon. The objective of this filter is to eliminate the fast neutrons but allow the thermal neutrons to pass through. Aluminum is good at minimizing the fast neutron flux at the end of the beam-port. The absorption cross-section for aluminum is low compared with silicon and it has short-lived neutron activation. Moreover, the ratio of the thermal-flux to the total neutron flux for aluminum is higher than for silicon.

Table 3.6. Thermal Neutron Flux as Determined by MCNP.

Thickness (cm)	Thermal-flux (n cm ⁻² s ⁻¹)	ϕ_{th} / ϕ_{total}
5	9.79×10^9	78%
10	6.12×10^9	82%
15	3.44×10^9	85%
17	3.00×10^9	86%
20	2.17×10^9	88%
21	1.90×10^9	88%
22	1.84×10^9	88.8%

The ratio of the thermal to total neutron flux reached 91% at the thickness of 7 cm and decreased as the thickness of aluminum increased. The aluminum filter was placed after the beryllium. Table 3.7 shows that the optimum thickness of aluminum is 7 cm, for which the ratio of the thermal-flux to the total flux at the target delivery system is 91%.

3.4.3.4. Gamma-ray filter for the thermal beam-port. Gamma-rays are emitted by the reactor core and produced by interactions with the filter materials. Bismuth is a good material that provides shielding from gamma-rays. Its low-neutron-absorption cross-section, high density (9.78 g/cm³), and atomic number ($Z = 83$) make bismuth effective at gamma-ray shielding (Turkoglu, 2011). A 1-cm-thick layer was placed at the far end of the beam-port to reduce the gamma-rays in the target delivery. The MCNP calculation uses a ICRP-74 flux-to-dose equivalent rate conversion factor (Ward, 2009). The result shows that the gamma dose dropped by 55% in comparison with the conditions with no bismuth

filter. The gamma-ray dose rate was 3.08×10^{-11} Gy cm², and the thermal neutron flux was not affected by the bismuth material.

Table 3.7. Neutron Flux Distribution as Determined by Using Aluminum Filter.

Thickness (cm)	Thermal-flux (n cm ⁻² s ⁻¹)	Epithermal-flux (n cm ⁻² s ⁻¹)	Fast-flux (n cm ⁻² s ⁻¹)	Total flux (n cm ⁻² s ⁻¹)	Φ_{th} / Φ_{total}
1	1.82×10^9	1.50×10^8	1.07×10^8	2.08×10^9	88%
2	1.77×10^9	1.18×10^8	9.20×10^7	1.98×10^9	89%
3	1.65×10^9	1.32×10^8	8.74×10^7	1.87×10^9	88%
4	1.59×10^9	1.38×10^8	8.17×10^7	1.81×10^9	88%
5	1.57×10^9	1.21×10^8	7.89×10^7	1.77×10^9	89%
6	1.42×10^9	1.12×10^8	6.85×10^7	1.60×10^9	89%
7	1.40×10^9	7.66×10^7	5.72×10^7	1.53×10^9	91%
8	1.34×10^9	1.03×10^8	6.60×10^7	1.51×10^9	89%
9	1.32×10^9	9.83×10^7	5.40×10^7	1.47×10^9	90%
10	1.24×10^9	8.93×10^7	4.65×10^7	1.37×10^9	90%

3.4.3.5. Final design for the thermal neutron beam-port. The final design of the thermal beam-port consisted of 21 cm of beryllium as the moderator followed by 7 cm of aluminum as a fast neutron filter, with 1 cm of bismuth at the far end as a gamma-ray filter (Figure 3.17).

The thermal neutron flux at the target delivery system was 91.7% of the total neutron flux. The gamma-ray dose rate was 3.08×10^{-11} Gy cm². The final neutron flux distribution for the thermal beam-port is shown in Table 3.8.

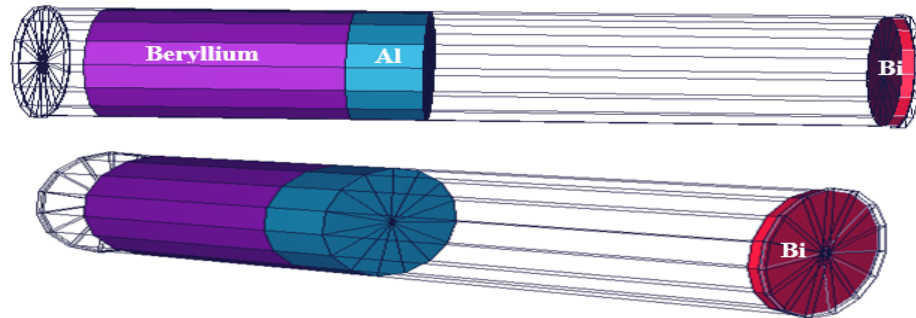


Figure 3.17. Final Design for the Thermal Neutron Beam-Port.

This beam port design can be configured for a desired neutron quality by changing the filter thicknesses. Algorithms were developed in MATLAB code to determine the beam flux quality and filter dimensions (see Sections 4.3 and 4.4).

Table 3.8. Thermal Neutron Beam-Port Flux Distribution.

Thermal-flux (n cm ⁻² s ⁻¹)	1.31×10^9	91.7%
Epithermal-flux (n cm ⁻² s ⁻¹)	6.95×10^7	4.9%
Fast-flux (n cm ⁻² s ⁻¹)	4.90×10^7	3.4%
Total flux (n cm ⁻² s ⁻¹)	1.43×10^9	100.0%

3.4.4. Optimization of the Beam-Port for a Fast-Flux. Some thermal neutrons from the pool can reach the target delivery system through the borated polyethylene in the movable base. Hence, the fast neutron filter needs to be a part of the target delivery system and not in the beam-port to ensure of having high quality of the fast-flux in the target delivery. The beam-port provides an uninhibited path for neutrons to pass through to the target delivery system. The aluminum target delivery tube is lined with 1.5 cm of cadmium to filter out thermal neutrons (Figure 3.18). The calculation shows that many fast neutrons arrive in the target delivery system (Figure 3.19).

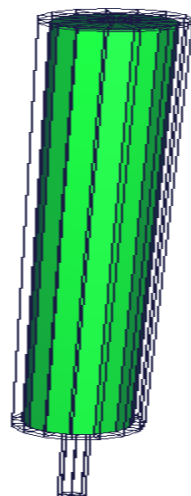


Figure 3.18. Target Delivery Tube

The neutron flux distribution for the fast neutron beam-port is shown in Table 3.9. The result shows that the cadmium filter absorbed all the thermal neutrons and the fast neutron flux is 51.8% of the total flux.

The total flux in the target delivery is $4.95 \times 10^9 \text{ n.cm}^{-2}\text{s}^{-1}$. The cadmium layer will be minimized the thermal-flux, this layer shields a large portion of thermal energy while

leaving the fast neutron increase. MCNP prediction of the neutron flux spectrum at the target delivery was calculated.

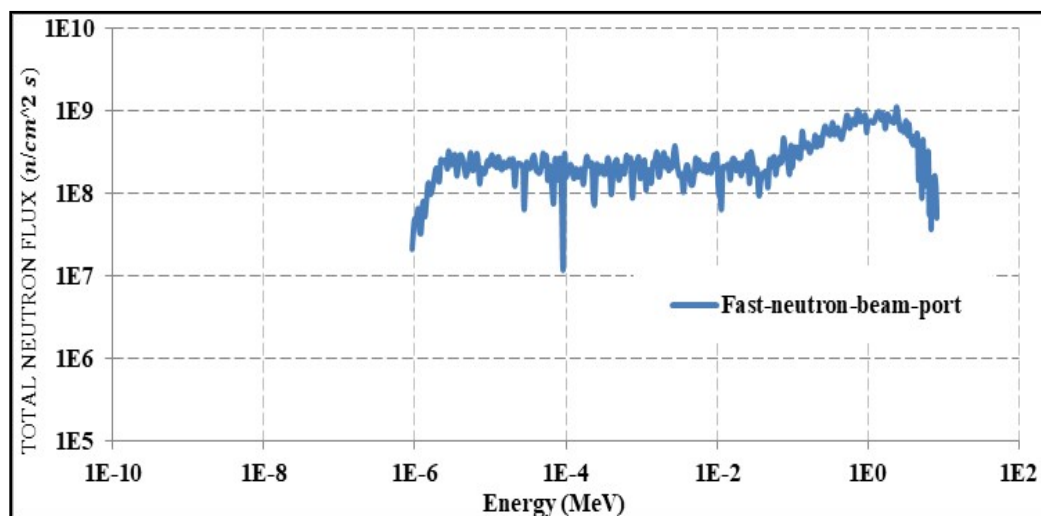


Figure 3.19. Fast Neutron Flux Spectrum in the Target Delivery System.

Results from this prediction confirmed the expected neutron spectrum, especially in fast energies. A goal of above 1×10^9 n.cm⁻².s⁻¹ was set as the desired neutron flux at the target region with low thermal neutrons for the fast-flux experiments region.

Table 3.9. Fast Neutron Beam-Port Flux Distribution.

Thermal-flux (n cm-2 s-1)	0.00	0.0%
Epithermal-flux (n cm-2 s-1)	2.39×10^9	48.2%
Fast-flux (n cm-2 s-1)	2.56×10^9	51.8%
Total flux (n cm-2 s-1)	4.95×10^9	100.0%

3.4.5. Optimization of the Beam-Port for a Gamma-Ray Flux. Filters were used to eliminate the neutrons that could contaminate the gamma-ray beam. First, 45 cm of beryllium was used to thermalize the high-energy neutrons and then 10 cm of aluminum was used to reduce the fast neutron flux further.

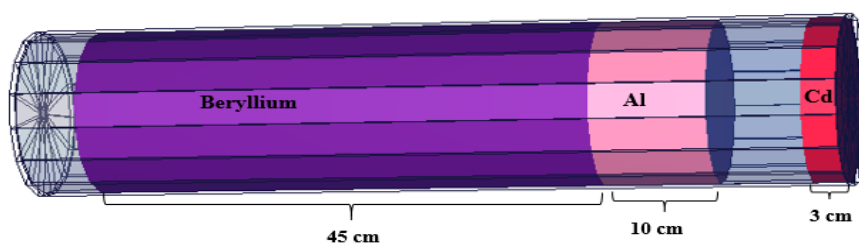


Figure 3.20. Gamma-Ray Flux Beam-Port.

At the end of the beam-port, 3 cm of cadmium was used to prevent thermal neutrons from reaching the target delivery system Figure 3.20. The calculation of the material filters was performed by using MCNP code.

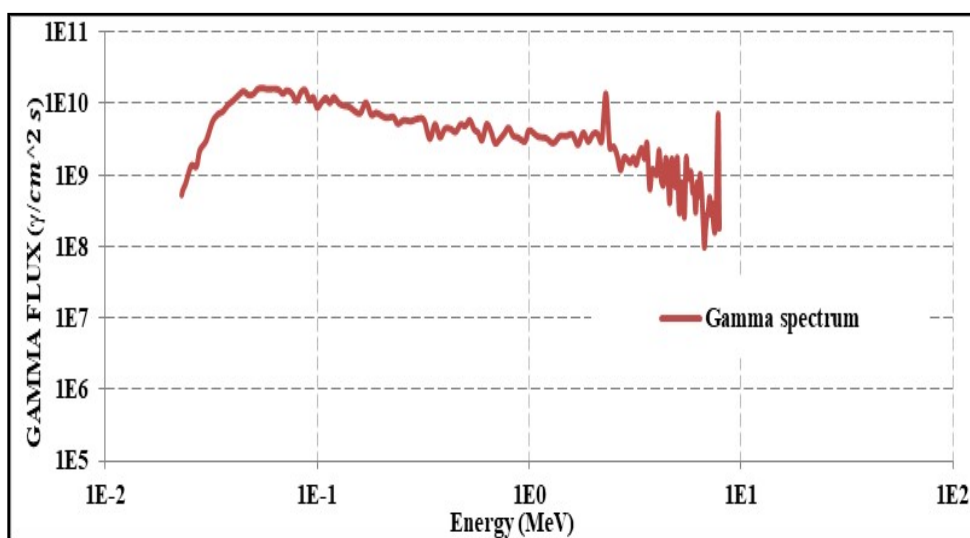


Figure 3.21. Gamma Spectrum in the Target Delivery.

The thickness of each material was increased gradually to minimize the neutron flux in the target delivery. The total gamma flux was $3.19 \times 10^{10} \text{ } \gamma/\text{cm}^2\text{s}$. The gamma spectrum in the target delivery system is shown in Figure 3.21.

4. CHARACTERIZATION OF NEUTRON BEAM SPECTRA

4.1. BEAM-PORT CONFIGURATION DETERMINATION

The beam-port system was simulated and optimized using the MCNP radiation transport code. MCNP simulations were performed to obtain the neutron flux for each beam-port system. The final design of a beam-port includes the beam-port size and the neutron filters. Since MCNP simulation of various configurations of the beam-port and material thickness are time intensive, quantitative characteristics were developed to determine the beam-port configuration requirements for a given spectrum at the target delivery. The reactor and target fluxes were known from the MCNP calculation. Also, the MCNP fluxes at some reactor positions have been validated through experiments. The neutron flux that enters from the reactor core and entering the beam-port φ_{rx} was assumed to be only in two groups, thermal-flux φ_{rx}^{th} and fast-flux φ_{rx}^f . The target flux in the target delivery location φ_{Trg} was also considered to be only thermal-flux φ_{Trg}^{th} and fast-flux φ_{Trg}^f . The reactor flux entering the beam-port and passing through moderator and filter materials with thickness S and removal cross-section Σ_r reach the target delivery (Figure 4.1).

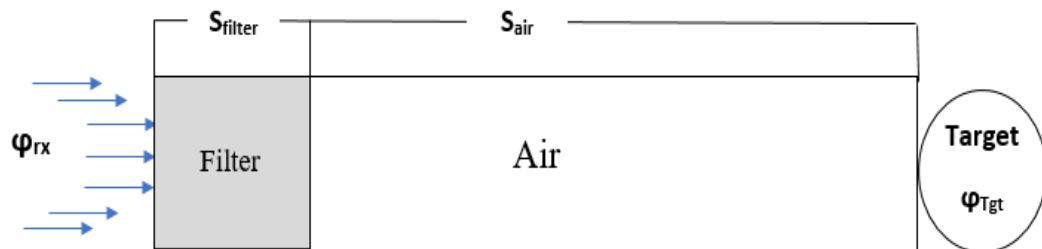


Figure 4.1. Beam-Port Configuration.

An algorithm was developed to determine the optimum thickness of the filter materials for the required neutron quality.

The neutron flux in the target delivery system is given by

$$\varphi_{Tgt} = \varphi_{rx} e^{-\alpha_r}, \quad (9)$$

where φ_{rx} is the reactor flux, and α_r is the attenuation coefficient (Figure 4.1). Here,

$$\varphi_{rx} = \varphi_{rx}^{th} + \varphi_{rx}^f, \quad (10)$$

In this equation, the target flux was assumed to consist of only fast and thermal neutrons. So, the fast-flux in the target is

$$\varphi_{Tgt}^f = \varphi_{rx}^f e^{-\alpha_r^f}, \quad (11)$$

where

$$\alpha_r^j = \Sigma_{r,filter}^j S_{filter} + \Sigma_{r,air}^j S_{air} = \sum_i \Sigma_i^j S_i, \quad (12)$$

where i is the index of the medium in the beam tube and j is the energy group. Σ_r is the removal cross-section that takes into account all scattering that does not advance particles toward the target cross-section. S_i is the thickness of the medium.

The thermal-flux in the target is

$$\varphi_{Tgt}^{th} = \varphi_{rx}^{th} e^{-\alpha_r^{th}} + \varphi_{rx}^f (1 - e^{-\alpha_L^{th}}) \prod_i \left(\frac{\Sigma_{SF}^f}{\Sigma_L^f} \right) \quad (13)$$

where $\varphi_{rx}^{th} e^{-\alpha_r^{th}}$ is the thermal-flux reaching the target delivery, and the second component of the equation contains two terms. The first term is $\varphi_{rx}^f (1 - e^{-\alpha_L^{th}})$, which is the fast-flux lost before reaching the target delivery, and second term, $\prod_i \left(\frac{\Sigma_{SF}^f}{\Sigma_L^f} \right)$ is the fraction of loss driven by forward scattering.

$$\alpha_L^f = \sum_i (\Sigma_r^{(f)} + \Sigma_{SF}^{(f)})_i S_i = \sum_i \Sigma_L^{(f)} S_i \quad (14)$$

where, Σ_{SF} accounts for all scattering cross-section that advances particles toward the target.

For the simulations that have been performed, only the cross-sections in the preceding equations are unknown. Whenever cross-sections for the materials are solved based on simulation, fluxes can then provide important information as follows:

- 1- Predict flux characterization for any material thickness.
- 2- Predict moderator and filter thicknesses given flux quality.

4.2. DETERMINATION OF MATERIAL CROSS-SECTIONS IN BEAM-PORT

A MATLAB code was used to calculate the cross-sections for the filter material for thermal and fast energies. Altogether, 26 MCNP models with different thicknesses and different arrangements of the filters were simulated and stored in an $m \times n$ matrix.

To obtain the cross-sections, Equations (11) and (13) can be simplified. Since

$$\alpha_r^j = \Sigma_{r,i}^j S_i \quad (15)$$

and

$$\alpha_r^j = \ln(\varphi_{rx}/\varphi_{Tgt}), \quad (16)$$

the matrix of linear equations is solved using

$$ax = b \quad (17)$$

giving

$$x = a^{-1} b \quad (18)$$

where a is the thickness of the material matrix, x is the cross-section for the filter matrix, and b is the alpha value (α_r^j) for each model at the i^{th} energy.

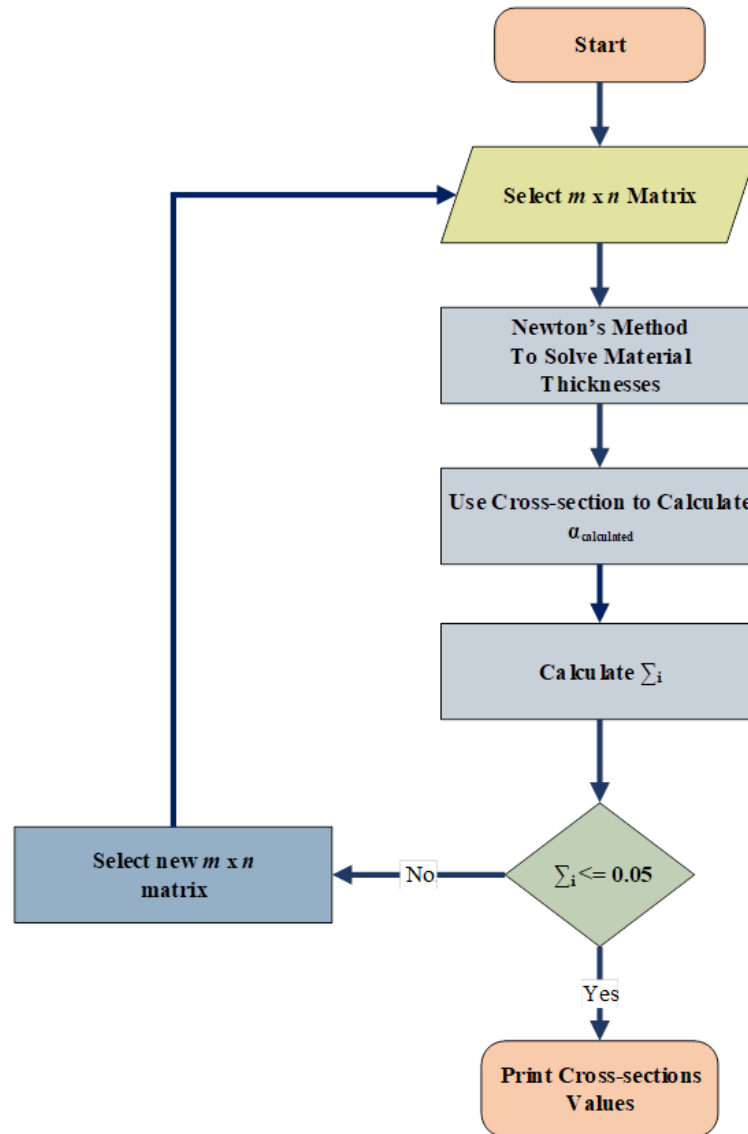


Figure 4.2. Cross-Section Algorithm Flowchart.

The MATLAB code is used to solve this system for the first iteration with a 3×3 matrix to obtain the first cross-sections, which were used to obtain the calculated alpha ($\alpha_{r,calculated}^j$). The code continues iterating until the tolerance \sum_i between the actual alpha (α_r^j) and the calculated alpha ($\alpha_{r,calculated}^j$) is less than 5%:

$$\sum_i = \frac{\alpha_{r,actual}^j - \alpha_{r,calculated}^j}{\alpha_{r,actual}^j} \quad (19)$$

Figure 4.2 describes the flow chart of the MATLAB algorithm for the filters cross-sections calculation. The results of the material cross-section are represented in Table 4.1.

Table 4.1. Material Cross-Sections in Beam-Port.

Material	Σ_r^f	Σ_r^{th}	Σ_L^f	Σ_{SF}^f
Beryllium	0.2356	0.1947	0.2358	0.1963
Aluminum	0.1869	0.1024	0.1850	0.3023
Air	0.0969	0.0704	0.0970	0.0951

4.3. FLUX PREDICTION GIVEN MATERIAL THICKNESSES

The cross-sections for beryllium, aluminum, and air were calculated with MATLAB (Table 4.1). These values were used to determine the neutron flux in the target delivery system. In this script, the thicknesses of the filters and the reactor fluxes were provided to obtain the target flux. The neutron flux thus determined is then compared with the original MCNP flux.

In the worst case when there is no filter in the beam-port, only air, the thermal-flux calculated by MCNP is $1.40 \times 10^{10} \text{ n cm}^{-2} \text{ s}^{-1}$ and by MATLAB is $1.32 \times 10^{10} \text{ n cm}^{-2} \text{ s}^{-1}$, a difference of 6%. The fast neutron fluxes obtained from MCNP and MATLAB are 2.94×10^9 and $2.79 \times 10^9 \text{ n cm}^{-2} \text{ s}^{-1}$, respectively, a difference of 5% (see Table 4.3). This prediction code provides results equivalent to what might be obtained from the MCNP calculation but in faster time (see Table 4.2). The scenario being considered here is the case

where filters of known dimensions are available and the resultant spectrum quality needs to be determined.

Table 4.2. Prediction Algorithm Time vs. MCNP Simulation Time.

Cases	Prediction Algorithm time (s)	MCNP Simulation time (min)
1	0.007156	176.69
2	0.007504	179.30
3	0.006775	176.66
4	0.007628	177.86
5	0.007113	176.88

4.4. MATERIAL THICKNESSES FOR DESIRED FLUX

Filter thickness prediction gives flux characteristics. The user provides thermal and fast-fluxes from reactor side to the code. The user also specifies the desired flux quality in the target delivery system. The code solves Equation (11) for fast neutrons and Equation (13) for thermal neutrons. The method of this calculation is described in the next section.

4.4.1. Problem Statement. The set of equations to be solved are Equations (11) and (13). The inner length of the beam-port, L_{port} , is 71.65 cm. Since there are three mediums in the beam-port configuration, the equation can be solved by using

$$S_{Be} + S_{Al} + S_{air} = L_{port} \quad (20)$$

and

$$\alpha_r^f = \Sigma_{r,Be}^f S_{Be} + \Sigma_{r,Al}^f S_{Al} + \Sigma_{r,air}^f S_{air} \quad (21)$$

Table 4.3. Predictive Neutron Flux Using MATLAB.

Cases	Filter Thicknesses			Thermal-Flux			Fast-Flux			Total Flux		
	Be	Al	Air	Prediction	MCNP	Error	Prediction	MCNP	Error	Prediction	MCNP	Error
	1	6	19	46.65	3.65×10^9	3.69×10^9	1%	2.19×10^8	2.09×10^8	5%	3.87×10^9	4.39×10^9
2	25	5	41.65	5.40×10^8	6.63×10^8	19%	3.56×10^7	3.05×10^7	14%	5.96×10^8	7.45×10^8	20%
3	42	5	24.65	6.61×10^7	6.38×10^7	3%	5.402×10^8	5.26×10^6	14%	7.14×10^7	7.14×10^7	1%
4	12	4	55.65	2.80×10^9	3.20×10^9	13%	2.80×10^8	2.35×10^8	16%	3.17×10^9	3.79×10^9	16%
5	0	0	71.65	1.32×10^{10}	1.40×10^{10}	6%	2.79×10^9	2.93×10^9	5%	2.04×10^{10}	1.60×10^{10}	22%

$$\alpha_r^{th} = \Sigma_{r, Be}^{th} S_{Be} + \Sigma_{r, Al}^{th} S_{Al} + \Sigma_{r, air}^{th} S_{air} \quad (22)$$

$$\alpha_L^f = (\Sigma_r^f + \Sigma_{SF}^f)_{Be} S_{Be} + (\Sigma_r^f + \Sigma_{SF}^f)_{Al} S_{Al} + (\Sigma_r^f + \Sigma_{SF}^f)_{air} S_{air} \quad (23)$$

Equations (11) and (13) can be simplified. Taking logs on both sides of Equation (10):

$$\begin{aligned} \ln(\varphi_{Tgt}^f) &= \ln(\varphi_{rx}^f e^{-\alpha_R}) \\ \ln(\varphi_{Tgt}^f) &= \ln(\varphi_{rx}^f) + \ln(e^{-\alpha_R}) \\ \ln(\varphi_{Tgt}^f) - \ln(\varphi_{rx}^f) &= -\alpha_R \ln(e) \\ \ln(\varphi_{Tgt}^f) - \ln(\varphi_{rx}^f) &= -\alpha_R \end{aligned}$$

Thus,

$$\alpha_r^f = \ln(\varphi_{rx}^f / \varphi_{Tgt}^f) \quad (24)$$

In a similar fashion, the following equation can be derived from Equation (11):

$$\alpha_r^{th} = \ln(\varphi_{rx}^{th} / \varphi_{Tgt}^{th}) \quad (25)$$

So, we have three equations and three unknowns. These equations are a system of non-linear equations.

4.4.2. Solution by Newton's Method. This iterative method is based on a Taylor series expansion and is used to find a solution of an equation in the form $\mathbf{F}(\mathbf{x}) = \mathbf{0}$. So, the first step is to transform Equations (14), (15), and (16) into the form $\mathbf{F}(\mathbf{x}) = \mathbf{0}$:

$$\Sigma_{r, Be}^f S_{Be} + \Sigma_{r, Al}^f S_{Al} + \Sigma_{r, air}^f S_{air} - \ln(\varphi_{rx}^f / \varphi_{Tgt}^f) = 0 \quad (26)$$

$$\Sigma_{r, Be}^{th} S_{Be} + \Sigma_{r, Al}^{th} S_{Al} + \Sigma_{r, air}^{th} S_{air} - \ln(\varphi_{rx}^{th} / \varphi_{Tgt}^{th}) = 0 \quad (27)$$

$$S_{Be} + S_{Al} + S_{air} - L_{port} = 0 \quad (28)$$

Newton's method states that for the k th iteration:

$$S^k = S^{k-1} - J(S^{k-1})^{-1} \mathbf{F}(S^{k-1}) \quad (29)$$

where $k = 1, 2, \dots, n$ is the iteration number. \mathbf{F} is a vector function and $J(S^{k-1})^{-1}$ is the inverse of the Jacobian matrix. This equation is used in Newton's method to solve non-linear algebraic systems. In this case, the system $F(x) = 0$ has to be solved.

F vector:

$$\mathbf{F}(S_{Be}, S_{Al}, S_{air}) = \begin{bmatrix} \Sigma_{r, Be}^f S_{Be} + \Sigma_{r, Al}^f S_{Al} + \Sigma_{r, air}^f S_{air} - \ln(\varphi_{rx}^f / \varphi_{Tgt}^f) \\ \Sigma_{r, Be}^{th} S_{Be} + \Sigma_{r, Al}^{th} S_{Al} + \Sigma_{r, air}^{th} S_{air} - \ln(\varphi_{rx}^{th} / \varphi_{Tgt}^{th}) \\ S_{Be} + S_{Al} + S_{air} - L_{port} \end{bmatrix} \quad (30)$$

Vector of unknowns:

$$\mathbf{S} = \begin{bmatrix} S_{Be} \\ S_{Al} \\ S_{air} \end{bmatrix} \quad (31)$$

Jacobian matrix:

$$\mathbf{J} = \begin{bmatrix} \partial f_1 / \partial S_{Be} & \partial f_2 / \partial S_{Al} & \partial f_1 / \partial S_{air} \\ \partial f_2 / \partial S_{Be} & \partial f_2 / \partial S_{Al} & \partial f_2 / \partial S_{air} \\ \partial f_3 / \partial S_{Be} & \partial f_3 / \partial S_{Al} & \partial f_3 / \partial S_{air} \end{bmatrix} \quad (32)$$

Here, the Jacobian matrix is

$$\mathbf{J} = \begin{bmatrix} \Sigma_{r, Be}^f & \Sigma_{r, Al}^f & \Sigma_{r, air}^f \\ \Sigma_{r, Be}^{th} & \Sigma_{r, Al}^{th} & \Sigma_{r, air}^{th} \\ 1 & 1 & 1 \end{bmatrix} \quad (33)$$

4.4.3. Solution Steps. The first step is to define the initial values for the variables:

$$\mathbf{S}^0 = \begin{bmatrix} S_{Be}^0 \\ S_{Al}^0 \\ S_{air}^0 \end{bmatrix} \quad (34)$$

The values can be changed randomly, and any initial guess will work. However, in this particular case, the initial guess for the unknowns is \mathbf{S}_0 .

Define $F(\mathbf{S}^0)$ and $J(\mathbf{S}^0)$:

$$\mathbf{F}(S_{Be}^0, S_{Al}^0, S_{air}^0) = \begin{bmatrix} \Sigma_{r,Be}^f(S_{Be}^0) + \Sigma_{r,Al}^f(S_{Al}^0) + \Sigma_{r,air}^f(S_{air}^0) - \ln(\varphi_{rx}^f/\varphi_{Tgt}^f) \\ \Sigma_{r,Be}^{th}(S_{Be}^0) + \Sigma_{r,Al}^{th}(S_{Al}^0) + \Sigma_{r,air}^{th}(S_{air}^0) - \ln(\varphi_{rx}^{th}/\varphi_{Tgt}^{th}) \\ S_{Be}^0 + S_{Al}^0 + S_{air}^0 - L_{port} \end{bmatrix} \quad (35)$$

The algorithm was verified and validated with the MCNP predications. For example, when MCNP run with 12 cm of beryllium thickness, 9 cm of aluminum, and 50.65 air. The thermal neutron flux at the target delivery system was $3.37 \times 10^9 \text{ n/cm}^2\text{s}$, and the fast neutron flux was $2.06 \times 10^8 \text{ n cm}^{-2} \text{ s}^{-1}$. The MCNP fluxes were used in the MATLAB code to calculate the thicknesses of the used filters. The result of this calculations shows the material thickness of beryllium is 11.0826 cm, 9.0397 for the aluminum, and 51.5277 cm for the air.

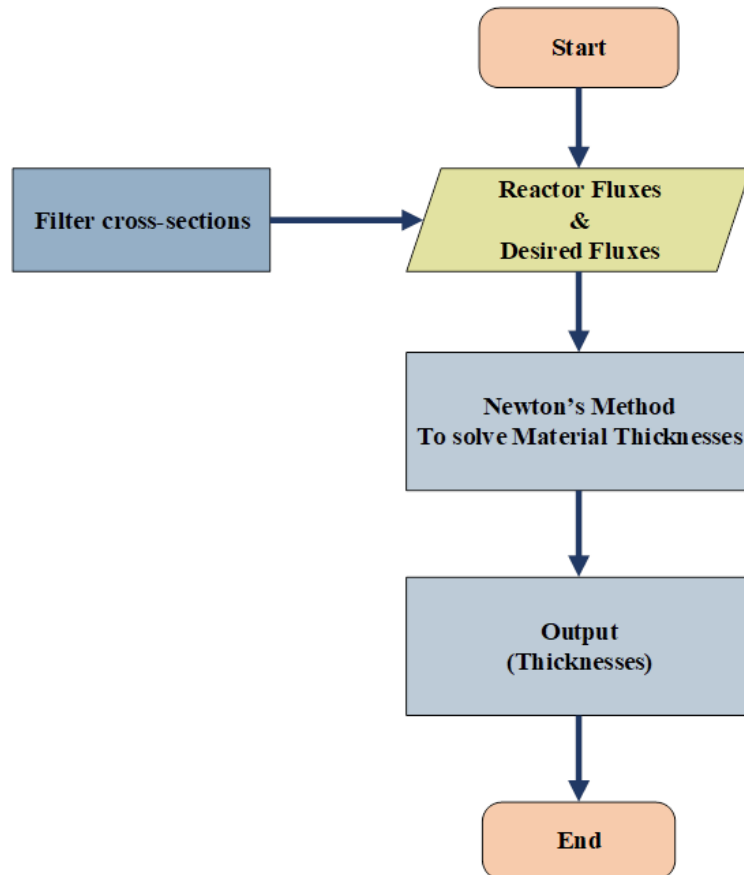


Figure 4.3. Filters Thickness Algorithm Flowchart.

The algorithm employs the Newton's method to solve for thicknesses in Equation 35. Filter material cross-section values required in Equation 35 are predetermined from algorithm shown in Figure 4.2. The filter thicknesses for 5 different flux-quality scenarios are shown in Table 4.4. For each scenario, the material thicknesses were used in MCNP simulations to determine various fluxes at the target delivery point. These fluxes were then provided to a MATLAB program based on the algorithm in Figure 4.3 to determined filter thicknesses needed for the specified fluxes. The difference showed a small difference from the thicknesses that used in the MCNP simulations, but this difference not affect the neutron ratio at the target delivery.

Table 4.4. Predictive Material Thickness Using MATLAB.

Cases	Target Flux Required Quality		Thicknesses (cm) Simulated in MCNP			Predicted Thicknesses (cm)		
	φ_{Tgt}^{th}	φ_{Tgt}^f	Be	Al	Air	Be	Al	Air
1	2.52×10^9	1.456×10^8	9	19	49.65	8.47	19.81	43.37
2	3.97×10^8	4.39×10^7	28	3	40.65	27.88	3.19	40.58
3	3.11×10^9	1.40×10^8	6	24	41.65	5.49	24.78	41.37
4	1.04×10^9	1.52×10^8	21	0	50.65	20.45	0.84	50.35
5	6.61×10^7	5.26×10^6	30	5	36.65	30.12	4.81	36.72

5. CONCLUSIONS

5.1. CONCLUSION ON MSTR PROMPT-NEUTRON SPECTRUM

The neutron flux spectrum in the MSTR at the source-holder tube and BRT were determined using irradiated foils and SAND-II as the spectrum unfolding code. The neutron flux spectrum for the source-holder tube and BRT were calculated in MCNP and used as the initial guess for SAND-II. The results confirmed the thermal spectrum expected in the source-holder. The thermal-flux (up to 0.55 eV) was 93.3% of the total flux. The thermal region of the spectrum as determined by SAND-II agreed with the MCNP calculations. Up to room-temperature energies, the thermal-flux contributions are within 10% of each other, and 17% of the total thermal-flux. However, the neutron spectrum estimate using MCNP and predicted using SAND-II are different for the epithermal and fast energies. The differences may be attributed to epithermal self-shielding in epithermal reactions, the coupling of limited fast neutrons, and the small fast absorption cross-sections. The results could potentially be improved by including additional foils and reactions to span the broad energy range better (0–20 MeV). For example, a combination of foils that contain Al, Fe, In, Mg, NaCl, Ni, S, Ti, V, Zn, Zr, Au, Co, Cu, Lu–Al, Mn–Cu, Mo, Sc, and W is recommended to provide coverage of different neutron energy ranges. In addition, using activities derived by irradiating infinitely dilute solutions of selected materials with large resonances would mitigate the effects of self-shielding in the spectrum unfolding.

Given that both MCNP and SAND-II spectra agree reasonably well, either method may be used to determine the flux spectrum at other locations within the reactor core. The agreement is particularly excellent for thermal spectra. Using MCNP is cheaper in both

time and resources than foil activation with spectrum unfolding. If a thermal spectrum is required, MCNP is adequate. The spectral disagreement between MCNP and SAND-II at high resonance and fast energies suggests the use of foil activation with spectrum unfolding. This would be the case if the reactor location of interest is within the fuel cluster. The activation-foil approach intrinsically accounts for the fuel-burnup credit near the location of interest. This assumes adequate foil choices and self-shielding corrections in the spectrum unfolding.

Another experiment obtained the neutron flux spectrum of the MSTR at the source-holder using solutions. Results from the experiment confirmed the expected neutron spectrum in the source-holder, especially for thermal energies. However, a depression in the resonance and fast regions of the determined spectrum occurred due to self-shielding of the foils. Repeating the experiment with infinitely dilute salt solutions indicated that the self-shielding effects had been overcome. The self-shielding effects on the foil-based spectrum are apparently due to indium foil.

5.2. CONCLUSION ON SENSITIVITY OF MSTR SPECTRUM TO INITIAL SPECTRUM GUESSES

The neutron flux spectrum of the MSTR at the BRT was determined using 17 different foils irradiated at 100 kW. Various initial guesses were used with SAND-II to obtain the best-fitting neutron flux for the BRT. The computed and experimentally obtained spectra were compared, and the relative error for each energy group was determined. Disparities were noted in the distributions of the thermal and epithermal-flux predictions as the number of bins in the initial spectrum guess changed. The 59%/19% distribution of

the thermal/epithermal flux, as predicted with the 620-group guess, is inconsistent with the 49%/26% distribution predicted with the 89- and 143-group guesses.

The predictions based on the 89- and 143-group guesses are consistent with the predictions obtained with the 22- and 50-group guesses. The 12-group initial guess resulted in the prediction of a fairly even distribution of the thermal (38%) and epithermal (36%) fluxes. Regardless of the number of groups used for the initial guess, the SAND-II prediction was found to be consistent in the fast energy range. The fast neutron flux ranged between 22% and 26%. The spectra predicted from 50-, 89- and 143-group initial guesses had the same thermal-flux contribution (49%) and comparable epithermal/fast flux distribution. These initial guesses also had comparable relative error distributions: about 85% of each group's energy bins had a relative error within 10%. Other group structures with vastly different flux distributions do not share the same level of precision as these groups. The results obtained with the 620-energy group are generally regarded as being reliable; the relative error was less than 20% in 86% of the bins. The thermal and epithermal region flux contributions are within 4% and less than 1% of that in the fast region. The 620-bin energy group is deemed reliable because it is exactly the energy bin structure employed in SAND-II to determine a spectrum. All cross-sections in SAND-II libraries are for the same group structure. Any other initial guess with a group structure mismatch compared with SAND-II will require the software to restructure the spectrum guess for the 620-bin calculations. However, this introduces an additional source of error and uncertainty into the calculations. In addition, the use of another energy group (a coarse energy group) in the neutron spectrum adjustment requires knowledge of the weighting spectrum in the

620-bin (the fine energy group). The result could potentially be improved using an updated cross-section library for SAND-II.

The results obtained by SAND-II show that the initial guess impacts the MSTR spectra, and caution is needed in the determination of the energy groups for the initial spectrum guess. The sensitivity of the reactor spectrum to relative errors in initial spectrum guesses has not been extensively investigated. It is likely that having comparable relative error distributions across all initial guess group structure would lead to a comparable flux distribution in the SAND-II prediction.

5.3. CONCLUSION ON MULTI-SPECTRUM BEAM-PORT DESIGN

A novel approach for the design and characterization of an underwater multi-spectral beam-port for neutron and gamma fluxes from pool-type research reactors was developed using the MCNP transport code. An additional novelty of this design is the potential for a neutron-only beam-port as well as a gamma-only beam-port. The design and characterization of the beam-port system, which was developed specifically for MSTR, can easily be replicated for any other pool-type research reactor. If space is restricted, this type of beam-port within the reactor pool saves space. More importantly, any reactor facility can use it to expand its research capabilities. It is a future-proof facility for the reactor because the beam tubes and reactor core can be redesigned for specific flux characteristics without the constraints of traditional beam-port design. These limitations motivated our design of a movable beam-port system. This system is flexible, allowing for changes to the beam-port and core. Moreover, the neutron-only mode can provide fluxes from soft (thermal) neutrons to hard neutrons. The flexibility is facilitated by filters and a collimator

configured to deliver various spectra and provide neutrons or gamma-rays. The design is relatively portable, allowing the beam-port to be moved into and out of the pool. The beam can be realigned whenever and wherever necessary.

The design of beam-ports for specific types of particle energy spectra was optimized and characterized using MCNP. One of the beam-ports was positioned to obtain the maximum neutron flux from the reactor core, as it was situated close to multiple fuel elements. The size of the beam-port tube was selected. Filters were used to deliver the desired flux beam. The thermal beam-port has 21 cm of beryllium to moderate the fast neutron flux and 7 cm of aluminum to reduce the number of fast neutrons. At the far end of the beam-port, a 1-cm-thick layer of bismuth was used to prevent gamma rays from reaching the target delivery system. The thermal beam-port has a high thermal neutron flux of 91.7% of the total neutron flux. The fast beam-port has a cadmium layer in the target delivery system to eliminate the thermal-flux. This design maximizes the number of fast neutrons for high-energy experiments. Another beam-port was designed to give only gamma flux. Various filters were used to remove the neutrons from the beam in the target delivery system. In its most thermal neutron configuration, the beam-port delivered $1.43 \times 10^9 \text{ n cm}^{-2} \text{ s}^{-1}$ to the target with 91.7% of the flux having energies no greater than 0.55 eV. The hardest spectrum achievable in its fast neutron configuration was $4.95 \times 10^9 \text{ n cm}^{-2} \text{ s}^{-1}$ with 51.8% of the flux having energies greater than 0.1 MeV. The beam-port was able to deliver gamma flux of $3.19 \times 10^{10} \text{ photons/cm}^2 \cdot \text{s}$ to the target.

The final design of the beam-ports, which includes the beam-port size and the neutron filters, was realized through various simulations. Since MCNP simulations are time consuming, quantitative characteristics were developed to determine the beam-port

configuration required for a given spectrum. The reactor and target fluxes were determined from the MCNP calculation and validated through experiments. An algorithm was developed to determine the optimum thickness of the filter materials for the required neutron quality. The quality of the flux in the target delivery system was theoretically estimated. The cross-sections of the beam-port filters were calculated and used to calculate the neutron flux in the target delivery system for the optimum thickness of each filter.

A predictive algorithm was developed in MATLAB to characterize the beam-port properties so that: 1.) beam flux quality could be determined given collimator and filter dimensions, and 2.) collimator and filter dimension could be determined given desired flux qualities. For both scenarios, the maximum prediction errors were 19% and 8.5% respectively. The algorithm reduced time required for one simulation to 0.007 seconds from 179 minutes when using MCNP.

BIBLIOGRAPHY

- AGENCY, I. A. E. (2014). *Applications of Research Reactors*. Vienna: INTERNATIONAL ATOMIC ENERGY AGENCY.
- Alqahtani, M., & Alajo, A. B. (2017a). *Analysis of a Conceptual Fast Neutron Island in The Missouri S&T Reactor*. Paper presented at the 2017 ANS Winter Meeting.
- Alqahtani, M., & Alajo, A. B. (2017b). Characterization of prompt neutron spectrum of the Missouri University of Science and Technology Reactor. *Nuclear Engineering and Design*, 320, 57-64. doi: <https://doi.org/10.1016/j.nucengdes.2017.05.017>
- Alqahtani, M., & Alajo, A. B. (2017c). *Resonance Self-shielding Impact on Neutron Spectrum Determination for Missouri S&T Reactor*. Paper presented at the. 2017 ANS Annual Meeting.
- ASTM E720-11. (2011). Standard Guide for Selection and Use of Neutron Sensors for Determining Neutron Spectra Employed in Radiation-Hardness Testing of Electronics, ASTM International, West Conshohocken, PA, www.astm.org.
- Azevedo, C. (2011). Selection of fuel cladding material for nuclear fission reactors. *Engineering Failure Analysis*, 18(8), 1943-1962.
- Baum, E. M., Knox, H. D., & Miller, T. R. (2002). *Nuclides and isotopes: chart of the nuclides*: KAPL.
- Behar, C. (2014). *Technology roadmap update for generation IV nuclear energy systems*. Paper presented at the OECD Nuclear Energy Agency for the Generation IV International Forum, accessed Jan.
- Böning, K., & Neuhaus, J. (2007). Neutron beams of FRM-II at the Technische Universitaet Muenchen *Utilization related design features of research reactors: A compendium*.
- Bonzer, W., & Carroll, C. (2008). Safety Analysis Report for The Missouri University of Science and Technology Reactor-Revision 2. *Rolla, MO*.
- Bunker, M. E. (1983). Early reactors—from Fermi’s water boiler to novel power prototypes. *Los Alamos Science*, 7, 124-131.
- Cagle, C. (1953). The Oak Ridge National Laboratory Graphite Reactor: Oak Ridge National Lab., Tenn.
- Canberra. (2010). Spectrum analysis introduction. www.canberra.com.

- Chadwick, M., Obložinský, P., Herman, M., Greene, N., McKnight, R., Smith, D., . . . Frankle, S. (2006). *ENDF/B-VII. 0: next generation evaluated nuclear data library for nuclear science and technology* (Vol. 107).
- Elmahroug, Y., Tellili, B., & Souga, C. (2013). Calculation of gamma and neutron shielding parameters for some materials polyethylene-based. *METHODOLOGY*, 3, 4.
- Grant, E., Mueller, G., Castaño, C., Usman, S., & Kumar, A. (2011). Internet accessible hot cell with gamma spectroscopy at the Missouri S&T nuclear reactor. *Nuclear Engineering and Design*, 241(8), 3306-3316. doi: 10.1016/j.nucengdes.2011.05.015
- Griffin, P. J., & Kelly, J. G. J. (1995). An 'Exact' Treatment of Self-Shielding and Covers in Neutron Spectra[^] eterrninations^l.
- History of the High Flux Isotope Reactor. *Oak Ridge National Laboratory*. Retrieved from <https://neutrons.ornl.gov/hfir-history>
- IAEA. (2016). *Research Reactors: Purpose and Future*. Vienna: INTERNATIONAL ATOMIC ENERGY AGENCY.
- Kirk, M., & Greenwood, L. (1979). Determination of the neutron flux and energy spectrum in the low-temperature fast-neutron facility in CP-5, calculations of primary-recoil and damage-energy distributions, and comparisons with experiment. *Journal of Nuclear Materials*, 80(1), 159-171.
- Knop, W., Pfaffenbach, K., & Schreiner, P. (2007). High utilization of the neutron beam system at the FRG-1 at Geesthacht *Utilization related design features of research reactors: A compendium*.
- Kouts, H. (1963). Beam-tube design for the high-flux beam reactor. *Journal of Nuclear Energy. Parts A/B. Reactor Science and Technology*, 17(4-5), 153-163.
- Kulage, Z. A., Castano, C. H., Usman, S., & Mueller, G. (2013). Characterization of the neutron flux energy spectrum at the Missouri University of Science and Technology Research Reactor (MSTR). *Nuclear Engineering and Design*, 261, 174-180. doi: <https://doi.org/10.1016/j.nucengdes.2013.03.041>
- Lamarsh, J. R., & Baratta, A. J. (2001). *Introduction to nuclear engineering* (Vol. 3): Prentice Hall Upper Saddle River, NJ.
- Luo, C. (2007). Neutron beam system at the China Advanced Research Reactor *Utilization related design features of research reactors: A compendium*.

- Martens, F. H., & Jacobson, N. H. (1968). *Research Reactors*. Oak Ridge, Tennessee, United States of America: USAEC Division of Technical Information Extension.
- McElroy, W., Berg, S., Crockett, T., & Hawkins, R. (1967). A computer-automated iterative method for neutron flux spectra determination by foil activation. *Kirtland AFB Report AFWL-TR, 67(41), 2*.
- Monte Carlo Team. (2003). MCNP-A General Monte Carlo N-Particle Transport Code, Version 5 Volume II User's Guide.
- MSTR. (2012-2013). *Annual Progress Report for the Missouri University of Science and Technology Reactor*. Nuclear Regulatory Commission: Retrieved from <https://www.nrc.gov/docs/ML1315/ML13156A004.pdf>.
- Neutron Beam Applications. (2018). *Nuclear Reactor Laboratory, Massachusetts Institute of Technology*. Retrieved from <https://nrl.mit.edu/research/neutron-beam>
- Richardson, B., Castano, C. H., King, J., Alajo, A., & Usman, S. (2012). Modeling and validation of approach to criticality and axial flux profile experiments at the Missouri S&T Reactor (MSTR). *Nuclear Engineering and Design, 245*, 55-61. doi: <https://doi.org/10.1016/j.nucengdes.2012.01.023>
- Roegler, H.-J. (2007). Issues to be considered when designing beam tubes *Utilization related design features of research reactors: A compendium*.
- Sinha, V., Avachat, A. V., & Lee, H. K. (2013). Design and development of a neutron/X-ray combined computed tomography system at Missouri S&T. *Journal of Radioanalytical and Nuclear Chemistry, 296(2)*, 799-806. doi: 10.1007/s10967-012-2062-x
- Spinrad, B. I., & Marcum, W. (Producer). (2018, February 7). Nuclear reactor. *Encyclopædia Britannica*. Retrieved from <https://www.britannica.com/technology/nuclear-reactor/Liquid-metal-reactors>
- . Standard Guide for Determining Neutron Energy Spectra from Neutron Sensors for Radiation-Hardness Testing of Electronics, ASTM International, West Conshohocken, www.astm.org. (ASTM E721-11, 2011).
- Tsoufanidis, N. (2010). *Measurement and detection of radiation*: CRC press.
- Tuli, J. K. (1995). *Nuclear wallet cards*: Brookhaven National Laboratory.
- Turkoglu, D. J. (2011). *Design, Construction and Characterization of an External Neutron Beam Facility at The Ohio State University Nuclear Reactor Laboratory*. The Ohio State University.

- Vries, J. W. d., & Verkoijen, A. H. M. (2007). *Recent beam upgrading developments at the HOR reactor*. International Atomic Energy Agency (IAEA): IAEA.
- Ward, D. C. (2009). Impact of switching to the ICRP-74 neutron flux-to-dose equivalent rate conversion factors at the sandia national laboratory building 818 neutron source range. *SANDIA REPORT SAND2009-1144*.
- Welzel, S. (2007). Demands on and requirements for the cold neutron source at HMI'S BER-II at Berlin *Utilization related design features of research reactors: A compendium*.
- Zijp, W. L., & Baard, J. H. (1981). *Nuclear data guide for reactor neutron metrology*: Office for Official Publications of the European Communities.

VITA

Meshari Mesfer ALQahtani was born in Riyadh, the capital city of Saudi Arabia. In 2006, he was awarded a scholarship from the King Abdullah Scholarship Program (KASP) to pursue an undergraduate degree abroad. In December 2009, Meshari graduated with a bachelor's degree in System Engineering from the University of Arkansas at Little Rock (UALR). In 2010, he joined the King Abdulaziz City of Sciences and Technology (KACST) as an academic researcher at the Nuclear Sciences Research Institute (NSRI). By January 2012, Meshari was awarded a graduate scholarship and joined the Missouri University of Science and Technology (Missouri S&T). He earned a Master of Science in Nuclear Engineering in July 2013. Thereafter, he carried out a Ph.D. research project under the supervision of Dr. Ayodeji B. Alajo. Meshari's Ph.D. research was primarily involved in designing an underwater beam-port system for pool-type research reactors, which represented a novel approach to the research reactor community. Such work contained a variety of accomplishments, for example characterizing and optimizing the neutronics behavior inside the research reactor. Meshari published and presented a couple of conference papers at the annual meeting of American Nuclear Society (ANS). He also published a peer-reviewed journal paper in Nuclear Engineering and Design (NED), a well-known prestigious journal. In December 2018, Meshari received a Ph.D. degree in Nuclear Engineering from Missouri S&T.